Investigations into Synthesis and Reactions of Black and Red Phosphorus Nanomaterials

A Thesis

Submitted to the Faculty

of

Drexel University

by

Samuel Andrew Lascio IV

in partial fulfillment of the

requirements for the degree

of

Master of Science in Chemistry

December 2017

Dedications

I dedicate this thesis to Christine Sarah Markiewicz, the most supportive and loving person I have ever met. For dealing with the stress of my work, comforting me through difficult and uncertain times, and pushing me to always do my best, I thank you. You mean the world to me.

Acknowledgements

I'd like to acknowledge my advisor, Dr. Hai-Feng (Frank) Ji, and co-advisor, Dr. Aaron T. Fafarman, for their continued support and use of facilities through my research at Drexel University. None of this would have been possible without their guidance and dedication to challenging me both academically and personally to become a more competent scientist and all around better person.

I also extend my deepest thanks to my group members and former colleagues, Zhen Qiao, Daniel Hagaman, Dr. Josh Smith, Dr. Noah Johnson, Ketao Chen, and especially Pedro E. Martins Amaral and Donald Hall (DJ), for their help in the technical aspects of running our instruments and various apparatuses. The quality of this work would not be what it is without them. I would also like to thank Drexel undergraduate Glen Nieman of the STAR (Students Tackling Advanced Research) Scholars Program, who aided me through the summer in preparing solutions and running instruments.

Lastly, I'd like to thank Dr. Anthony Addison for serving on my thesis committee after his retirement from Drexel. His guidance throughout my graduate career cannot be understated, and I appreciate his dedication to the students of the Chemistry Department. Enjoy retirement!

Table of Contents

List of Tables

List of Figures

Abstract

Investigations into Synthesis and Reactions of Black and Red Phosphorus Nanomaterials

Samuel Andrew Lascio IV

Hai-Feng (Frank) Ji, Ph.D. and Aaron T. Fafarman, Ph.D.

Research discoveries in carbon nanostructures have encouraged scientists to look for the next generation of versatile nanomaterials with novel electronic and optical properties to generate new scientific knowledge and discover materials with unanticipated or enhanced functionality. One element that has become of great interest in the last few years is phosphorus. Although studies investigating phosphorus nanostructures and properties are still in their infancy, unique properties of various phosphorus nanostructures are expected. First, in a literature review, this work will summarize some optical and optoelectronic applications of both black and red phosphorus. The role of phosphorus as a photocatalyst is also discussed. Next, this work will explore liquid exfoliation techniques applied to 2D black phosphorus with several exotic and common laboratory solvents, both with and without the use of potentially damaging ultrasonication. Lastly, investigations into reactions of black phosphorus and boron trifluoride under ambient conditions will be undergone to study the formation of boron phosphate.

Chapter 1: Optical, Optoelectronic, and Photocatalytic Applications of Phosphorus Nanomaterials

1.1 Introduction to Phosphorus Allotropes

Research into nanomaterials has opened the door to new possibilities in engineering and nanotechnology. As more applications are found, it has pushed scientists to look for the next generation of versatile materials. One element that has become of great interest in the last few years is phosphorus. With its different stable and semi-stable allotropes, phosphorus provides unique potential for an array of applications due to its electronic and, specifically, optical properties.

There are three common allotropes of phosphorus: white phosphorus, red phosphorus, and black phosphorus.[1-2] White phosphorus exists as molecular P_4, with strained P-P bonds. This causes white phosphorus to be extremely reactive and will ignite upon contact with air to form phosphorus oxides.[2] Red phosphorus is a semi-stable polymeric solid produced by heating white phosphorus between 200°C and 260°C in a vacuum.[1-2] Red phosphorus exists in a number of different forms, both crystalline and amorphous, with Type IV being called fibrous red phosphorus and Type V being known as Hittorf's phosphorus or violet phosphorus.[2-3] Black phosphorus is the most thermodynamically stable allotrope (by approximately 21 kJ/mol compared to P_4) and is widely studied for its semiconducting properties.[2,4] The transition from white to red phosphorus at -17.6 kJ/mol demonstrates that the red allotrope is slightly more stable than white and less stable than black, as it will spontaneously produce phosphoric acid upon contact with oxygen and water, although the reaction rate is slow.[2,5] 2D sheets of black phosphorus have been termed 'phosphorene', which are most commonly produced by exfoliation from bulk. Structures for the solid phosphorus allotropes are detailed in Figure 1.1 below.

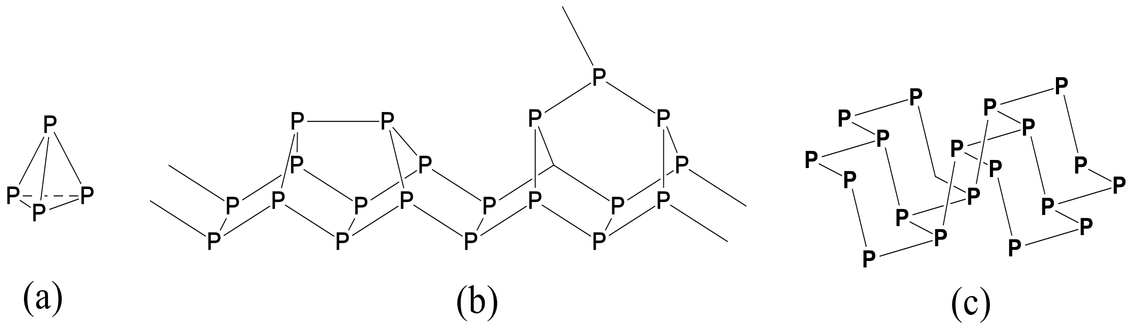

Figure 1.1 – Molecular structures of common allotropes of phosphorus. (a) White phosphorus, P_4. (b) Type IV and V red phosphorus. (c) Black or 2D Phosphorus (phosphorene).

Other common phosphorus allotropes are known to exist, such as P_2 gas (diphosphorus), however it will be the red and black allotropes on which this work will focus.

While a comprehensive theoretical study into possible phosphorus nanostructures was published in 1995,[6] research investigating phosphorus nanostructures and their properties is still in its infancy, with the bulk of publications happening within the last 3-4 years. Thus, research into these materials is ripe for discovery.

1.1.1 Red Phosphorus

Red phosphorus (RP) exists as five distinct types, with each type varying in crystallinity. These types were first reported in 1947 by Roth et al and were obtained via thermal analysis by heating red phosphorus as a sample bulb against alundum as a reference bulb from room temperature to 550°C.[7] Roth et al determined that the differences between the sample and reference bulbs, observed by the peaks in Figure 1.2, corresponded to an exothermic process, although these transitions did not hold any thermodynamic significance, because heating was performed far from equilibrium.[7] The areas between peaks were considered polymorphs of red phosphorus and were labeled Types I-IV in order of appearance.

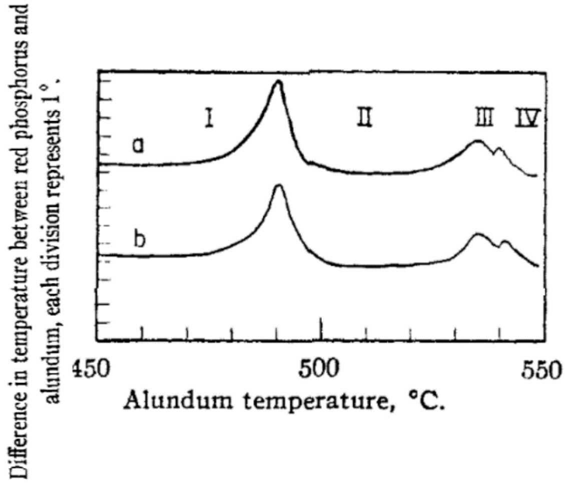

Figure 1.2 – Thermal analysis of red phosphorus: 1.5 grams of RP; heating rate, 1°C per min.; Curves (a) and (b) represent two separate runs of the analysis.[7]

The last type, Type V, was determined via X-ray analysis, as it did not show up under thermal analysis. The samples prepared for X-ray analysis displayed unique patterns when heated beyond 550°C.[7] While not addressed in the Roth paper, Type V red phosphorus has since been identified as Hittorf's violet phosphorus, first identified in 1865.

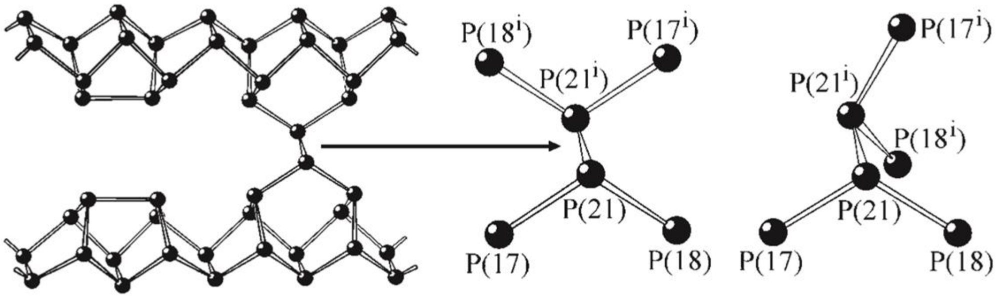

Figure 1.3 – Linkage of the tubes in fibrous phosphorus (left; i: -x, 1-y, -z) vs. Hittorf's phosphorus (right; i: -x, y, 0.5-z). Bonding lengths and angles in the structures of fibrous and Hittorf's phosphorus that differ by more than 3 SD: P(21)-P(21^i) 222.4(8)/217.3(1) pm; P(17)-P(21)-P(18) 111.9(3)/115.98(3)°, P(17)-P(21)-P(21^i) 94.7(3)/96.71(4)°, P(18)-P(21)-P(21^i) 93.6(3)/108.23(2)°.[3]

It is worth noting that while both Types IV and V have the same backbone structure (see Figure 1.1), they differ in crystallinity by how the chains connect to one another (see Figure 1.3). In Type IV fibrous red phosphorus, the phosphorus cage polymer chains run parallel (‖) to one another. In Type V violet phosphorus, the phosphorus cage polymer chains run perpendicular (⊥) to one another. Table 1.1 provides a side-by-side comparison of the five red phosphorus types.

Table 1.1 – A Comparison of Red Phosphorus Types.[2-3,7-9]

Type I	Types II/III	Type IV	Type V
Amorphous	Crystalline	Fibrous	Hittorf's Violet
Heating WP to 250°C in a vacuum	Type II: rods Type III: Undefined	Heating RP with I_2 catalyst at ~550°C	Heating RP to 590°C for several days
Most common form of red phosphorus	Both types not well understood	Prop. in 1947, confirmed in 2005	Chains are ⊥ as opposed to ‖ in Type IV

1.1.2 Black Phosphorus and Phosphorene

Black phosphorus is the thermodynamically stable allotrope of phosphorus, with bulk crystals composed of corrugated sheets of covalently bonded phosphorus atoms stacked by van der Waals forces (Figure 1.4).[10] Black phosphorus can be produced with a thickness-dependent band gap of approximately 0.35 eV for bulk crystalline BP, and calculations suggest a 2-2.5 eV estimated band gap for monolayered 2D BP.[10-13] These band gap values for black phosphorus thin films have also been shown to be sensitive to applied strain.[14]

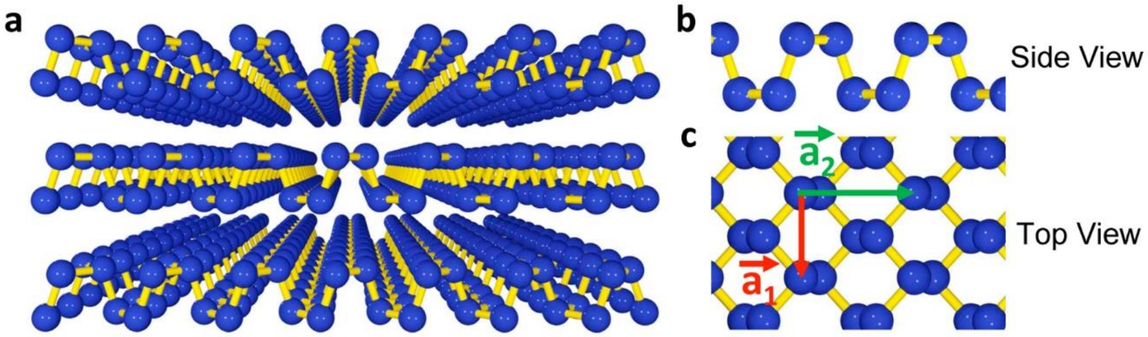

Figure 1.4 – Crystal structure and band structure of few-layer phosphorene. (a) Perspective side view of few-layer phosphorene. (b,c) Side and top views of few-layer phosphorene.[15]

In 2014, Liu et al produced a phosphorus analog to graphene that they dubbed 'phosphorene'. A technique first utilized for graphene, the team used mechanical exfoliation via Scotch tape to isolate 1-4 layers of phosphorene.[15] While the paper does not specify how large the sample is (only its thickness), the Scotch-tape method typically only creates flakes that are suitable for laboratory research, but are insufficient for large-scale production. Atomic force microscopy (AFM) determined that a single layer of phosphorene has a thickness of about 0.85 nm.[15] An important note from this paper is that phosphorene thickness in excess of 2 nm has environmental sensitivity not seen in other 2D materials such as graphene or MoS_2. This sensitivity to ambient conditions limits the potential applications of the material and applies constraints to how it can be studied in the lab, however a thin layer of PMMA can protect the material.[15]

Two of the most promising methods for large phosphorene sheet production are CVD and liquid exfoliation. In a paper from our laboratory's researchers Joshua Smith and Daniel Hagaman, it has been confirmed that phosphorene sheets of 4 layers or more can be synthesized using CVD.[4] RP powder or one piece of bulk BP (approximately 0.5 mg each) was placed in a tube furnace at 600°C in the presence of a silicon substrate for 30 minutes under vacuum.[4] Once cooled, the substrates contained a thin green (40 nm thick determined by AFM) or blue (< 10 nm thick determined by AFM) film of red phosphorus.[4] These were heated in the presence of Sn/SnI_4 (10 mg) mineralizing agents in a 27.2 atm Ar atmosphere, producing a wide range of BP flake thicknesses (3.4-600 nm) grown directly on the substrate with flake areas as large as 9000 μm^2. However, it should be noted that the flakes determined to be about 4 layers thick were only around 0.35 μm^2. Liquid exfoliation techniques will be discussed later in this work.

1.2 Anisotropic and Nonlinear Optical Properties of Black Phosphorus

Both the linear and nonlinear optical properties of BP are strongly spatially anisotropic and can be tuned by the BP film thickness.[16] In a 2015 paper by Li et al, the anisotropic properties of black phosphorus were investigated, with the results of the transmittance of BP thin films versus thickness of the films shown in Figure 1.5.[16]

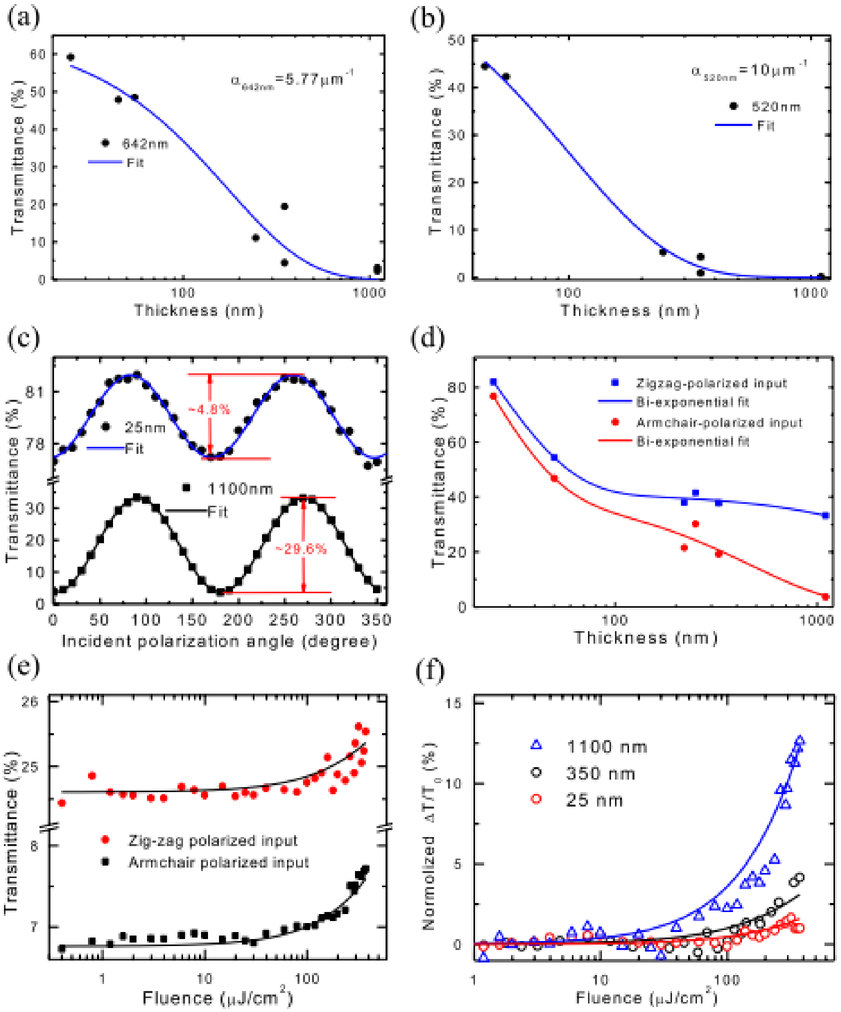

Figure 1.5 – Linear and nonlinear optical properties of BP films: Transmittance of BP films as a function of thickness at the wavelengths of (a) 642 nm and (b) 520 nm. (c) Polarization dependent transmittance for 25 nm and 1100 nm thick BP films. (d) Transmittance of BP films as a function of film thickness at the wavelength of 1550 nm with two orthogonal polarized light directions. (e) Fluence dependent transmittance of the 1100 nm thick BP film measured with ultrafast pulses at two orthogonal polarized light directions. (f) Relative transmittance change measured from 25nm, 350 nm and 1100 nm thick BP films as a function of input pulse fluence. The input polarization direction is along the armchair direction of the BP films.[16]

The polarization directions that correspond to the maximum and minimum of the transmittance curves in Figure 1.5c are linked with the zigzag and armchair axes of the black phosphorus thin films.[16] Specifically, Figures 1.5e and 1.5f correspond to the nonlinear properties of black phosphorus thin films. Li et al utilized the nonlinear properties for an ultrafast high energy pulse study, with the pulse duration reported at approximately 786 fs in mode-locking and the pulse energy's maximum output at about 18.6 nJ in Q-switching.[16]. Their work demonstrates that the nonlinear optical properties of black phosphorus are useful for lasing and other applications, such as ultrafast optical switches/modulators and frequency converters.[16]

1.3 Optical Reflectance of Phosphorus

In 2015, Tao Hu, Arqum Hashmi, and Jisang Hong conducted a theoretical study on the geometry, electronic structures, and optical properties of phosphorus nanotubes (PNTs).[17] The basis for their work came from a paper published only a year prior to theirs in which Zhen Zhu and David Tománek conducted a computational study on a currently unrecognized allotrope of phosphorus, which they dubbed 'blue phosphorus'.[18] Structural differences between black phosphorus and blue phosphorus can be seen in Figure 1.6.

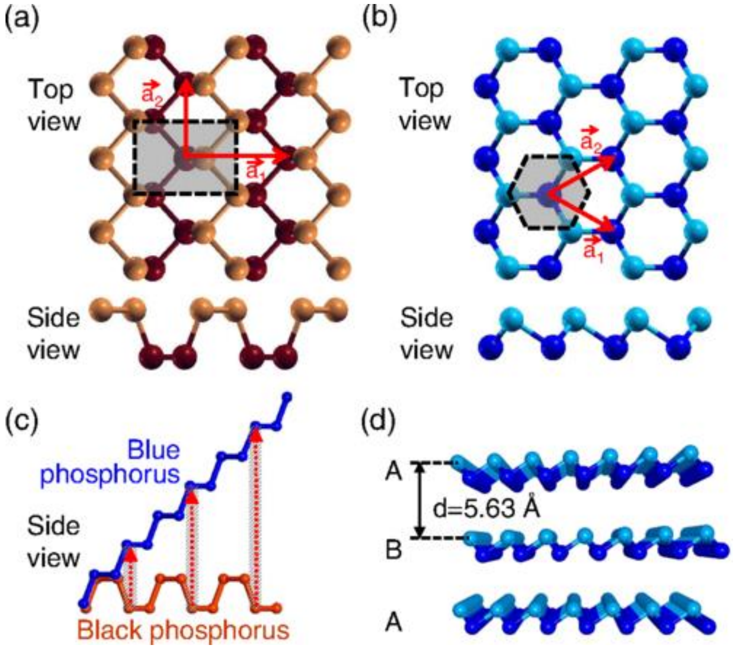

Figure 1.6 – The layered structure of (a) black and (b) blue phosphorus in top and side views. Atoms at the top and bottom of the non-planar layers are distinguished by color and shading, and the Wigner-Seitz cells are shown by the shaded region. (c) Schematic of the conversion of black to blue phosphorus by dislocations, highlighted by the shaded regions and arrows. (d) Equilibrium structure of AB stacked blue phosphorus as viewed from the side.[18]

Hu et al investigated two distinct types of phosphorus nanotubes, which they named α-PNTs, for the nanotubes made from blue phosphorus monolayers, and β-PNTs, for the nanotubes made from black phosphorus monolayers. The team predicts that both armchair and zigzag geometries (analogous to carbon nanotubes) are possible for α-PNTs, but only the armchair geometry is feasible with β-PNTs because the zigzag conformation induces too much strain from conformational energies.[17] The band structures revealed that the band gap is larger for the blue phosphorus α-PNTs than the band gap for the black phosphorus β-PNTs. The researchers found that the band gap for α-PNTs did not depend on the configuration (armchair or zigzag) of the phosphorus tubule, nor the inner diameter of the tubule when the inner diameter exceeds 13 Å, but the β-PNTs do in fact show configuration and diameter dependence.[17]

This all led to the researchers discussing the optical properties, and presented the frequency-dependent dielectric function for the armchair and zigzag α-PNTs and the armchair configuration for the β-PNTs and considered parallel electric fields ($E_{||}$) and perpendicular electric fields ($E_{\perp}$) with respect to the nanotube axis.[17] The frequency-dependent dielectric function comes from the Kramers-Kronig relation:

$$\epsilon(\omega) = \epsilon_1(\omega) + i\epsilon_2(\omega) \tag{1.1a}$$

$$\epsilon_1(\omega) = \frac{1}{\pi} P \int_{-\infty}^{\infty} \frac{\epsilon_2(\omega')d\omega'}{\omega' - \omega} \tag{1.1b}$$

$$\epsilon_2(\omega) = -\frac{1}{\pi} P \int_{-\infty}^{\infty} \frac{\epsilon_1(\omega')d\omega'}{\omega' - \omega} \tag{1.1c}$$

where P denotes the Cauchy principle value and implies that the principle part is to be taken at the point $\omega' = \omega$.[17,19] They noted no significant disparity in the frequency-dependent dielectric functions among armchair nanotubes with different indices in α-PNTs, and the zigzag α-PNTs show the same trend. They also discovered that the magnitude of the dielectric function for parallel polarization is generally larger than that for perpendicular polarization, which the authors hypothesize will result in asymmetric optical properties.[17] For the blue phosphorus α-PNT armchair nanotubes, $\varepsilon_1(0)$ was 2.7 for parallel polarization and 2 for perpendicular polarization. For the α-PNT zigzag nanotubes, $\varepsilon_1(0)$ was 1.7 for parallel polarization and 1.4 for perpendicular polarization. This demonstrates a directional dependence with the α-PNTs on the angle of incoming polarized light.

Interestingly, the β-PNTs were shown to be independent of the polarization direction, with a value of 2.9 for parallel polarization and 2.8 for perpendicular polarization.[17]

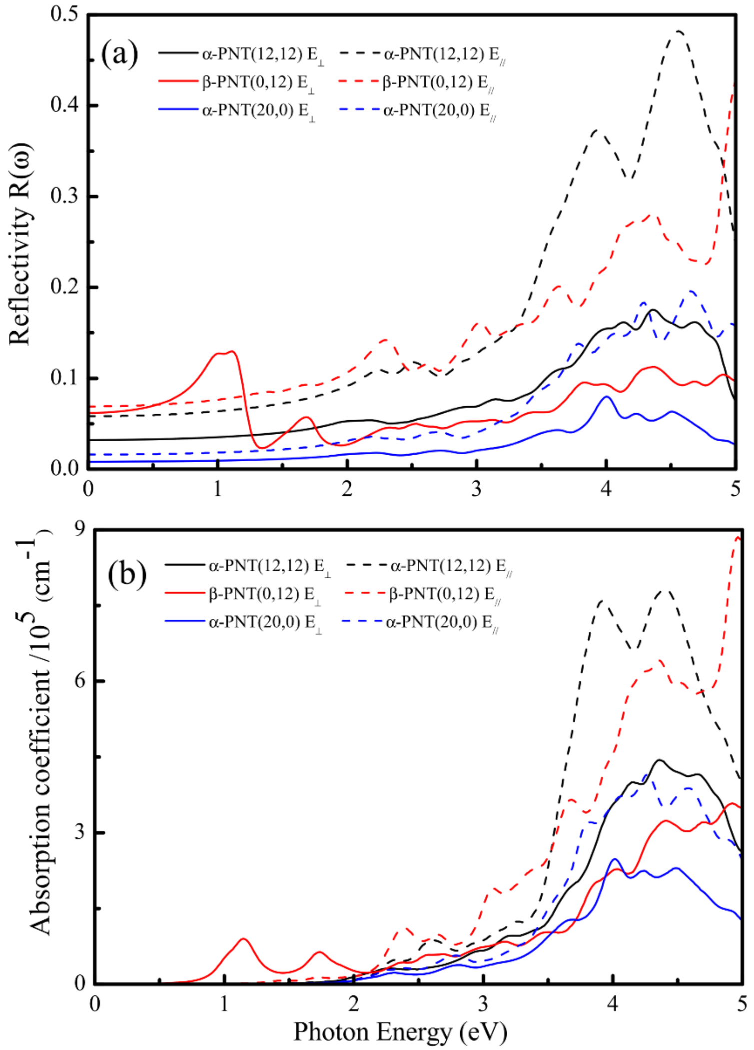

Figure 1.7 – Calculated optical quantities: (a) reflectivity (b) absorption coefficients of α-PNTs (12, 12), (20, 0) and β-PNTs (0, 12).[17]

The researchers graphed the reflectivity (see Figure 1.7a) of different phosphorus nanotubes using the following equation:

$$R(\omega) = \left|\frac{1-\sqrt{\epsilon_1(\omega)+i\epsilon_2(\omega)}}{1+\sqrt{\epsilon_1(\omega)+i\epsilon_2(\omega)}}\right|^2 \tag{1.2}$$

where the epsilon functions come from Equation 1.1.[17] With regard to the blue phosphorus α-PNTs and black phosphorus β-PNT (the armchair configuration), the phosphorus nanotubes had greater reflectivity for the parallel polarization than for the perpendicular polarization, but the zigzag α-PNT form showed very weak reflectivity in the visible frequencies, demonstrating strong asymmetric behavior regarding the polarization direction. Unfortunately, this weak reflectivity value may cause issues for reflecting or anti-reflecting applications.[17]

While not referenced in the Hu et al paper, there was research published in 1984 from Hideo Asahina and Akira Morita that worked with many of the same topics. Asahina and Morita's paper details the optical properties of black phosphorus single crystals as opposed to phosphorus nanotubes. The pair also utilized the frequency-dependent dielectric function from Equation 1.1a some 30 years before the Hu et al paper. However, it is their research into the reflective properties of black phosphorus that drew the most interest for this review.

Asahina and Morita cited a 1983 paper by themselves with Yusei Maruyama where they measured the reflectance spectra on the cleaved xy-surface of a black phosphorus single crystal at room temperature for linearly polarized light in the range from 400 to 2000 nanometers (see Figure 1.8).[11]

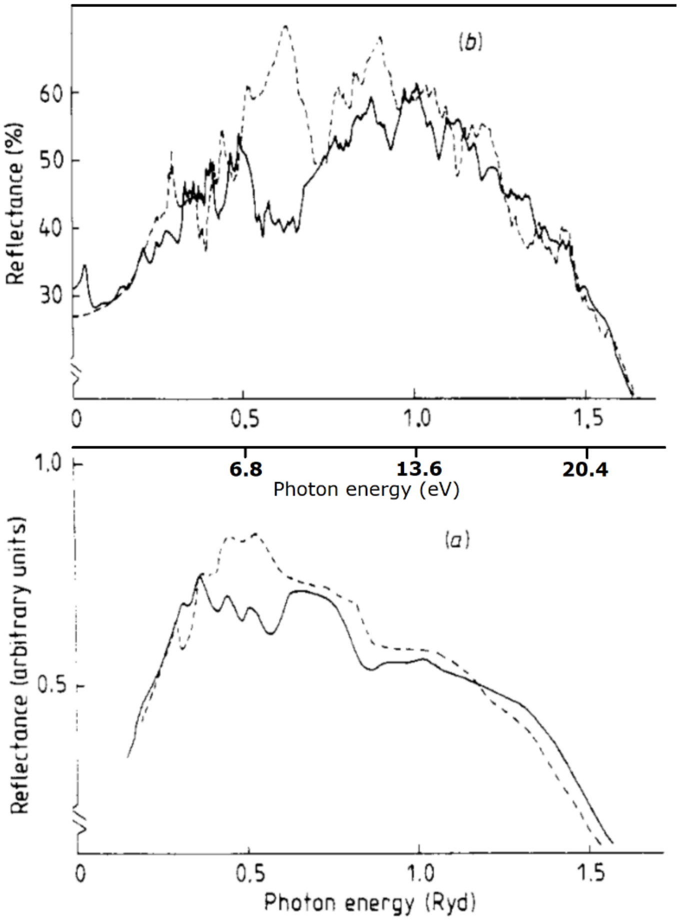

Figure 1.8 – Reflectance spectra from visible to vacuum ultraviolet: (a) experimental curves obtained by Taniguchi et al (1982) and (b) theoretical ones. Full curves are for the polarization $E \parallel \hat{x}$ and broken curves for the polarization $E \parallel \hat{y}$.[11]

To keep consistent with Figure 1.7, the x-axis units in Figure 1.8 for photon energy, Ryd, were converted from 0, 0.5, 1.0, and 1.5 Ryd to 0, 6.8, 13.6, and 20.4 eV, respectively, and added to the graph.[20] This demonstrates that different forms of phosphorus exhibit varying degrees of reflectance at different photon energies, which makes phosphorus a versatile material depending upon the specifications needed for optical devices.

1.4 Optical Compensator of Black Phosphorus

An optical compensator or waveplate is an optical device used in polarized light microscopy. Optical anisotropy is studied using a polarized light microscope with accessory plates that are divided into two primary categories: retardation plates, which have a fixed optical path difference, and compensators, which have variable optical path lengths.[21] Compensators and retarders come in two standard forms: half-wave plates (HWPs) and quarter-wave plates (QWPs), which require a birefringent material to accomplish the desired phase shift.[22] Traditional waveplates are composed of optically anisotropic quartz, mica, and gypsum minerals ground to a precise thickness and mounted between two optical windows having flat (plane) faces, which are designed to introduce a fixed amount of retardation between the orthogonal wave fronts passing through the crystal. Recently, manufacturers have also begun developing highly aligned and stretched linear organic polymers to produce anisotropic retardation plates.[21]

A paper published by Mao et al in 2016 suggested that the optical properties of few-layer black phosphorus could be a viable candidate for future waveplate applications. The low-energy band gap of black phosphorus had in the past limited the study of its optical anisotropy to the near-infrared (NIR) spectrum, however Mao et al were successful in direct observation of the optical anisotropy of few-layer black phosphorus in the visible spectrum by using polarized optical microscopy.[23] The researchers tested the black phosphorus samples on a fused silica substrate and a 300 nm SiO_2/Si substrate and found that the optical brightness of black phosphorus on the 300 nm SiO_2/Si substrate changed dramatically with the rotation angle (see Figure 1.9), which is demonstrated in other phosphorus allotropes.[11,16-17,23]

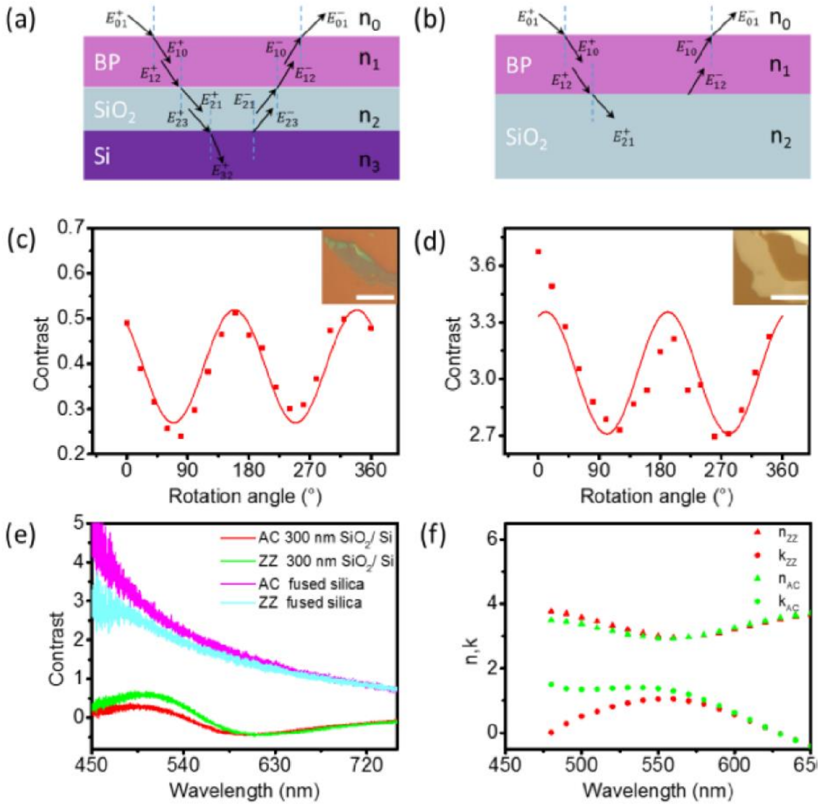

Figure 1.9 – Simulated and measured anisotropic optical contrast and refractive indices for few-layer BP on 300 nm SiO_2/Si and fused silica substrate. Optical reflection and transmission schematic for multi-thin films system: (a) BP on 300 nm SiO_2/Si and (b) fused silica. n stands for the refractive index of different media: air (n_0), BP (n_1), SiO_2 (n_2) and Si (n_3). Angle-dependent optical contrast of (c) the 5 nm BP samples on 300 nm SiO_2/Si and (d) fused silica under parallel polarizations. The wavelength of the incident light is 480 nm. Solid curves are fitted results using simulated equation. Insets are the corresponding optical images of the BP samples. The scale bar is 10 µm. (e) Optical contrast spectra along AC and ZZ crystalline direction of 5 nm thick BP on 300 nm SiO_2/Si and fused silica substrates, respectively. (f) Measured refractive indices for 5 nm thick BP along AC and ZZ crystalline directions. The solid triangles and dots are the real and imaginary parts of the refractive indices, respectively.[23]

1.5 Both Black and Red Phosphorus as a Photocatalyst

In a time when renewable energy is becoming increasingly necessary to sustain our needs, one avenue that has gained a lot of attention is hydrogen generation from water and other sources. To be applicable, a photocatalyst with a suitable conduction band energy (around 2.0 eV to utilize solar energy effectively) is necessary for transferring the photo-generated electrons to water.[24] The added challenge of being stable in water makes it difficult to develop new visible-light-driven photocatalysts, especially simple elemental ones that are economically viable.[24]

One work conducted by Lee et al, published in 2015, sought to construct a hybrid photocatalyst using semiconducting 2D black phosphorus with titanium dioxide (TiO_2). Black phosphorus layers (usually 1-3 phosphorene sheets), compared to graphene and MoS_2 based alternatives, have higher carrier mobility and both p-type and n-type configurations in field-effect transistor (FET) sensors, however few-layer black phosphorus tends to be unstable due to oxygen and humidity, so a stabilizing agent is introduced in the form of TiO_2.[25] Fabrication involved 0.025 mol of titanium isopropoxide dissolved in 40 mL of ethyl alcohol mixed with 0.2 grams of black phosphorus dispersed in 400 mL of anhydrous ethyl alcohol, then 2 mL of this solution was added drop-wise to DI water.[25] The titanium isopropoxide hydrolyzes in water to form $Ti(OH)_4$, which then forms the BP@TiO_2 photocatalyst based on the following proposed equations:

$$Ti - OH + HO - Ti \rightarrow Ti - O - Ti + H_2O \tag{1.3}$$

$$BP_{surface} - P - OH + HO - Ti \rightarrow BP_{surface} - P - O - Ti + H_2O \tag{1.4}$$

Figure 1.10 shows a model of the hybrid photocatalyst, along with additional data from the article. The researchers found that the hybrid photocatalyst held an approximately 92% efficiency after 15 runs, which is a vast improvement over pure few-layer black phosphorus, which degrades in air after several uses.[25]

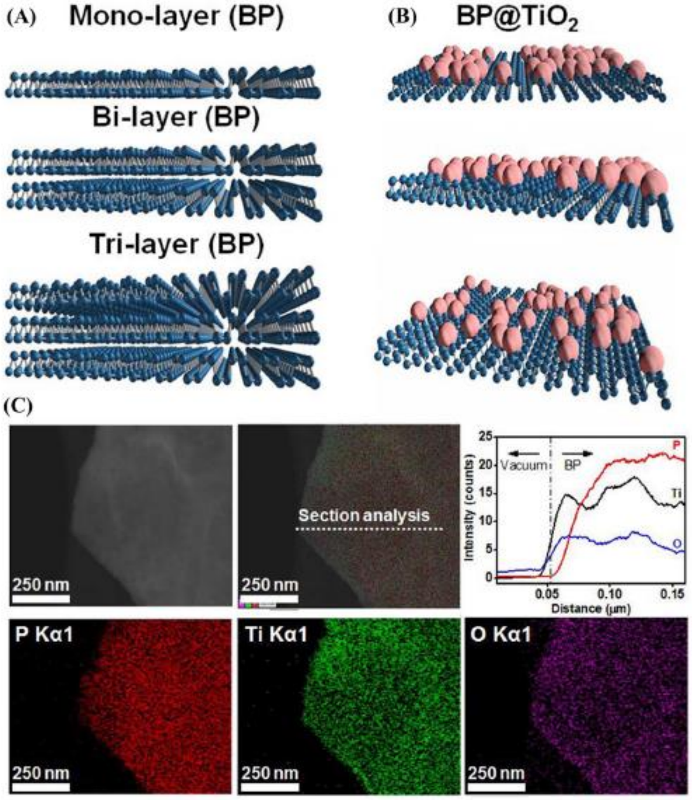

Figure 1.10 – (a) Modeled mono-, bi-layer, and tri-layered BP structures, (b) TiO_2 substitution on BP structure, and (c) line profile (top panel) and its elemental mapping (bottom panel) of P, Ti, and O elements in BP@TiO_2 hybrid photocatalyst.[25]

Other work being done with phosphorus photocatalysts includes a 2015 article by Shen et al in which they produce a purely elemental heterostructure by ball milling black phosphorus with red phosphorus, creating high visible-light-driven (VLD) photocatalytic activity comparable to that of CdS.[26] The authors used 50 wt% BP in the mixture, and found that varying the BP amount, both higher and lower, resulted in poorer results. However, they reported only 85% activity after 3 cycles,[26] which is less than the TiO_2 hybrid photocatalyst produced by Lee et al.

Red phosphorus can also be used as a photocatalyst. Wang et al measured the rate of hydrogen gas production by irradiating 100 mL of solution (50 mg of products in 5 mL of methanol, as a hole sacrificial agent, and 95 mL of water) using a 300-watt Xe lamp, with H_2 being produced at a rate of 0.08 μmol/hr for crystalline red phosphorus.[24] Amorphous red phosphorus was found to be only half as effective, possibly because the surface area of the crystalline red phosphorus (about 39 m^2/g) is larger than that of amorphous red phosphorus (about 18 m^2/g), i.e., increased surface area and a decrease in the number of electron–hole trapping centers.[24] To confirm the water photolysis process, a control experiment in the absence of methanol was performed. The results confirmed that H_2 comes from photoreduction of water, and the rate of H_2 formation also decreased by about 4 times in the absence of methanol, reaffirming that methanol most likely functions as a sacrificial agent to consume the photo-generated holes and improve the efficiency of red phosphorus.[24] Platinum metal was also added as a co-catalyst, created via the photo-reduction of H_2PtCl_6.[24] The researchers found the H_2 production rate increased with increasing Pt content, maximized around 1–3 wt% (12 times the activity without Pt), then decreased with additional Pt.[24] The team hypothesized that small amounts of Pt act as an effective co-catalyst by lowing the activation potential of H_2 formation and suppressing the recombination of photo-generated charges, but excess amounts of platinum, exceeding around 4 wt%, would increase the number of electron–hole recombination centers, resulting in a lower efficiency.[24]

A 2016 paper by Hu et al shows that the rate of hydrogen gas formation using red phosphorus has greatly improved over time. The group tested two different approaches, the first being micro-fibrous red phosphorus grown on a silicon dioxide fiber and the second being “smashed-fibrous” red phosphorous, which was ultrasonically smashed from bulk.[27] Using methanol as a sacrificial agent and Pt as a co-catalyst, like the Wang et al paper, and under visible light irradiation, the team measured a hydrogen gas production rate of 196 μmol/(hr·g). However, the paper justifies that since silicon dioxide is photoinactive and phosphorus comprises 31 wt% of the red phosphorus-SiO_2 fiber, the true rate of hydrogen production is estimated to be around 633 μmol/(hr·g).[27] The group obtained a similar value of 684 μmol/(hr·g) for the "smashed-fibrous" red phosphorus, with these rates being the highest values among purely elemental photocatalysts for visible light-driven hydrogen evolution from water.[27] Most of the authors contributed to a 2017 review paper that performed an extensive overview of neutral P, phosphide (P^{3-}), phosphate (P^{5+}), and phosphorus composite/doped photocatalysts, including theoretical models.[28]

A composite material that has been tested as a photocatalyst is P-CdS (red phosphorus and cadmium sulfide). The experimental conditions for measuring the rate of hydrogen gas production were quite similar to the Wang (2012) paper: irradiation of a 100-mL solution (50 mg of photocatalysts in 100 mL of 0.1 M Na_2S and 0.1 M Na_2SO_3 aqueous solution) using a 300-watt Xe lamp reduced Pt in added H_2PtCl_6 to create a 1 wt% Pt co-catalyst.[29] While pure CdS demonstrates a hydrogen generation of 364.5 μmol/(hr·g), 10 mol% RP added to the material ($P_{0.1}$-CdS) multiplied this H_2 generation by approximately 2.53, yielding a value of 923 μmol/(hr·g).[29]

Due to rising costs and availability of platinum metal, work has been done to try and replace it in the catalytic process without sacrificing performance. This is yet another avenue where red phosphorus has proven useful. While molybdenum phosphide (MoP) has proven effective in hydrogen evolution reactions (HERs), bulk molybdenum disulfide (MoS_2) demonstrates little HER activity.[30] However, a hybrid material of the formula $MoS_{2(1-x)}P_x$ (x ranging from 0 to 1) created from annealing bulk particulate MoS_2 with red phosphorus has shown great promise, with x = 0.53 demonstrating maximum performance of the material, where an overpotential of approximately 150 mV delivers a current density of 10 mV/cm^2, 90 mV less than is needed for pure MoP to achieve a similar current density.[30] While this is not directly referencing red phosphorus as a photocatalyst on its own, it does demonstrate its versatility in generating hydrogen gas from water in the production of a non-precious metal replacement to platinum as a catalytic material through annealing with MoS_2.[30]

As a counter to the Lee (2015) article, rather than using TiO_2 with 2D black phosphorus, work done by Sajid Ali Ansari and Moo Hwan Cho in 2016 introduced red phosphorus into TiO_2 via high energy ball milling to create a nanohybrid photocatalyst, which caused a shift in the light absorption ability from UV to the visible spectrum, and confirmed that the optimal RP loading and milling time can effectively improve the visible light driven-photocatalytic activity of TiO_2.[31] The positives of their methods include the ease of creating the RP-TiO_2-12 hour nanohybrids (50 wt% RP powder ball milled with TiO_2 for 12 hours at 250 rotations per minute), the cost effectiveness of using commercially available red phosphorus, and utilizing TiO_2, which is capable of harnessing solar energy for hydrogen generation via water splitting reactions.[31]

1.6 Black Phosphorus as a Saturable Absorber and Modulator

A saturable absorber is an optical component with a certain optical loss, which is reduced at high optical intensities.[32] A Polish team led by Jaroslaw Sotor generated ultrashort pulses with Er-doped and Tm-doped fiber lasers of 272 fs centered at 1560.5 nm and 739 fs centered at 1910.5 nm, respectively. These laser fibers contained approximately

300 nm thick layers of black phosphorus, and transmission increased by about 4.4%.[33] Pulse speeds of 805 fs and 940 fs have also been reported.[34-35] Jiang et al found comparable results using black phosphorus as a saturable absorber, however they also used a thulium/holmium-doped fiber laser (THDFL). This particular laser demonstrated a 100-nm wavelength range could be achieved from 1832 to 1935 nm by adjusting the pump power.[36] While this work was conducted in the near-IR region, work has also been done on the mid-IR region (between 2500 nm and 25000 nm). Qin et al worked with a 2.8 µm passively Q-switched Er:ZBLAN fiber laser using multi-layer black phosphorus as a saturable absorber. They found that the laser delivered a maximum average output power of 485 mW with a pulse energy of 7.7 µJ, pulse width of 1.18 µs, and repetition rate of 63 kHz.[37] Many of the team members also worked on another project investigating wavelengths of 1.03 µm, 1.93 µm, and 2.72 µm, which yielded similar results for multilayered black phosphorus, noting that saturable absorption at 2.72 µm approached the material’s absorption limit.[38] Similarly, Li et al used a passively Q-switched singly Ho^{3+}-doped fluoride fiber laser emitting at 2970.3 nm and mode-locked Ho^{3+}/Pr^{3+} co-doped fluoride fiber laser centered at 2866.7 nm, both utilizing the same black phosphorus saturable absorber. Here, they generated a pulse duration of 8.6 ps at a repetition rate of 13.987 MHz for the holmium/praseodymium laser (output power and pulse energy were 87.8 mW and 6.28 nJ, respectively) and a pulse duration of 2.41 µs at a repetition rate of 62.5 kHz for the holmium laser (the output power and pulse energy were 308.7 mW and 4.93 µJ, respectively).[39] Lastly, work done by Fan et al utilizing a passively Q-switched $Er:Lu_2O_3$ laser operation at 2.84 µm generated a minimum pulse duration of 359 ns with the highest average output power of 755 mW and a pulse energy of 7.1 µJ.[40] These results are all significant because very few current

saturable absorbers work stably in the mid-infrared spectral regime, and several different experiments confirm that black phosphorus is a cheap and viable candidate.[37]

It is also worth noting that research has been done investigating the damage done to black phosphorus saturable absorbers. While investigating black phosphorus as a reliable material for a saturable absorber, Lee et al found that the material was capable of handling operations with a high intracavity power (greater than the power level which would damage BP in a blocking interaction) when involved in a non-blocking interaction scheme using a side-polished fiber for passively mode-locked pulsed lasers.[35] They connected the black phosphorus-deposited side-polished fiber to the cavity set of their set-up at a high-powered laser setting of 23.3 dBm for 168 hours and found that the repetition rate (3.82 MHz) stayed constant throughout the exposure with only some fluctuation in spectral width (14.2 nm) centered at 1558.8 nm.[35]

The major difference between a saturable absorber and an optical modulator has to do with the type of Q-switching involved. For passive Q-switching, which has been discussed, the losses are automatically modulated with a saturable absorber, where the pulse is formed as soon as the energy stored in the gain medium has reached a sufficiently high level.[41] However, for active Q-switching, the losses are modulated with an active control element (active Q-switch) typically either an acousto-optic or electro-optic modulator, where the pulse is formed shortly after an electrical trigger signal arrives. There are also mechanical Q switches such as spinning mirrors, used as end mirrors of laser resonators. In any case, the achieved pulse energy and pulse duration depends on the energy stored in the gain medium, i.e. on the pump power and the pulse repetition rate.[41] Research into using black phosphorus as a saturable absorber demonstrated that it could also be used as an optical modulator.[36,38,40] A review of 2D layered materials for use as optical modulators was already written in detail by Zhipei Sun, Amos Martinez, and Feng Wang.[42] Of note, Sun et al stated that black phosphorus was an attractive material for mid- and near-IR optoelectronics due to the fact that few-layer phosphorene remains direct for all sample thicknesses. However, as observed by Liu et al, the major drawback to using black phosphorus in this application is its sensitivity to oxygen and humidity when in mono- or few-layers, requiring that in ambient conditions, the material be hermetically sealed.[15,42]

1.7 Photoconductivity and Photodetection of Both Black and Red Phosphorus

Notable research into the study of black phosphorus as an infrared photodetector dates back to work done by Baba et al in 1989. Here, the team was able to determine that black phosphorus crystals demonstrated photoconductive properties with a linear response for light intensity and a selective response for polarized light in the near-IR region.[43] Repeated work in 1991 showed that photoconduction was possible up to the mid-IR region as well.[44] However, while a paper published in 2001 showed that semiconducting black phosphorus could show metallic-like photoconduction at high pressure,[45] it would still be another couple of decades until 2D materials became a major research interest that this property would be reinvestigated. From a paper published in 2015 by Yuan et al, they were able to produce photo-response rise times of linear dichroic black phosphorus photodetectors upwards of 40 μs, which is reported as a major improvement over previously reported photodetectors based on layered chalcogenides, which produce photo-response rise times on the order of milliseconds and slower.[46] They were also able to show polarization sensitivity over a broad bandwidth from approximately 400 nm to 3750 nm (UV-Vis-to-mid IR region), affirming the near-IR results from the other work.[43,46]

Graphene photodetectors can suffer from very high dark current since certain graphene chiralities lack a band gap, whereas layered black phosphorous is ideal for photodetector applications due to its narrow but finite band gap.[47] Fabricated devices utilizing the band gap of black phosphorus have been shown to operate under bias with very low dark current, attaining an intrinsic responsivity up to 135 mA W^{-1} and 657 mA W^{-1} in 11.5-nm- and 100-nm-thick devices, respectively, at room temperature.[47]

Multilayer black phosphorus has also been used as a multispectral photodetector for use in imaging. Research conducted by IBM scientists Michael Engel, Mathias Steiner, and Phaedon Avouris demonstrated that a black phosphorus photodetector could not only handle imaging simple shapes, but also complex text patterns using scanning electron microscopy.[48] Their results are shown in Figure 1.11 below. This work demonstrated not only the application of black phosphorus photodetectors in the visible and near-IR spectral regime, but the clear imaging quality taken from the novel material.[48]

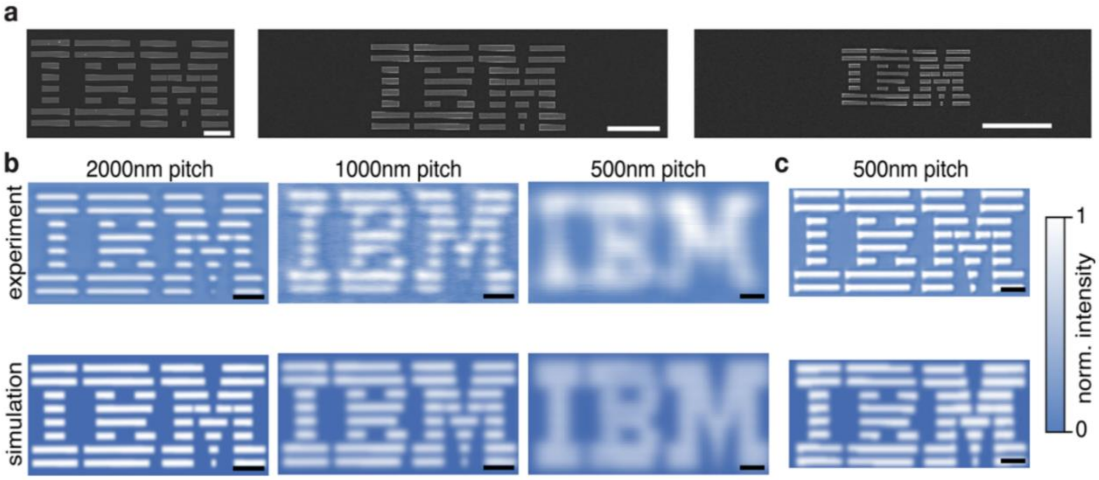

Figure 1.11 – (a) Scanning electron micrographs of test patterns on glass cover slides with feature sizes and pitch of 2000, 1000, and 500 nm. Scale bars are 10 µm. (b) Measured images excited at λ_{IR} = 1550 nm (top row) and simulated images (bottom row). Scale bars are 10, 5, and 2 µm. (c) Experimental image excited at λ_{IR} = 532 nm (top) exhibiting submicron features, along with the simulated image (bottom).[48]

An article by Penillard et al published in 2016 sought to use the photoconductive properties of black phosphorus to create optoelectronic devices, such as a microwave photoconductive switch, which allows optical control over the magnitude and phase of microwave signals.[49] The authors note that 2D black phosphorus is a very promising material for optoelectronic applications, because of its tunable band gap.[49]

The paper published in 2012 by Wang et al discussed previously also demonstrated the photoconductive properties of red phosphorus. While the paper focused on the applications of these properties, the researchers went into detail about which properties of red phosphorus come from photoconductivity. The group put 100 mg of red phosphorus inside a quartz tube, sealed under vacuum, and heated to 650°C to create a roughly 10-µm-thick phosphorus thin film.[24] The photocurrent was 0.09 A/cm^2 when light was applied from fiber optics equipped with a tungsten lamp of intensity 200 mW/cm^2, and dropped to

0.002 A/cm^2 without illumination, which verifies that electrons and holes are generated over red phosphorus under illumination with the proposed mechanism:[24]

$$P_{red} + hv \rightarrow h^+(P) + e^-(P) \tag{1.5a}$$

$$h^+ + CH_3OH \rightarrow HCOOH \text{ } or \text{ } HCHO \tag{1.5b}$$

$$e^- + H_2O \overset{Pt}{\rightarrow} H_2 + OH^- \tag{1.5c}$$

where $h^+(P)$ and h^+ designate the generated hole in the phosphorus atom and $e^-(P)$ designates the photo-generated electron from red phosphorus. Equation 1.5b is unbalanced and meant to demonstrate the sacrificial methanol agent oxidizing to either formic acid or formaldehyde in the presence of the red phosphorus hole left by the electron. A mobility of 8.05 cm^2/V·s was calculated from the sheet resistance and Hall coefficient, indicating that red phosphorus should be considered a p-type semiconductor.[24]

1.8 Perspective

Extensive studies have been carried on the development of inexpensive, versatile materials. Phosphorus has gradually attracted researchers' attention, with black phosphorus and red phosphorus being the two main allotropes of interest. The last few years have seen a dramatic increase in the study of phosphorus and its optical properties.

The nonlinear optical properties of black phosphorus flakes are anisotropic and can be tuned by the black phosphorus film thickness, which is not seen in common 2D layered materials used today. Phosphorus nanotubes utilize a possibly new allotrope of phosphorus, blue phosphorus, and exhibit optical reflectance dependent upon the angle of incoming polarized light. Phosphorus nanotubes also seem to exhibit these reflective properties differently depending upon which allotrope is used for the tube frame, black phosphorus or blue phosphorus. Since phosphorus displays a wide range of optical reflections depending upon allotrope, it makes this a desirable material for use in a variety of applications. Phosphorus also satisfies the needs of a visible light photoconductor, with a tunable band gap in the range of 0.3 eV to potentially 2.5 eV. With its semiconducting properties, it makes phosphorus applicable in areas where graphene (which exhibits metallic conduction characteristics) would be unsuitable.

The optical properties of phosphorus give rise to many theoretical applications, but there are a few where phosphorus allotropes are shown to work. Whereas traditional waveplates are composed of optically anisotropic quartz, mica, and gypsum minerals, studies have shown that few-layer black phosphorus is a viable candidate for future waveplates due to its refractive index. Our society has developed a need for green, reusable technologies and fuel sources, and phosphorus has proven an effective photocatalyst in H_2 generation from water, both in the black and the crystalline red allotropes. Black phosphorus layers have even been shown to exhibit both n-type and p-type semiconducting properties in FET sensors. Mixtures of black phosphorus with TiO_2, red phosphorus with TiO_2, and even black phosphorus with red phosphorus have also proven effective as visible-light-driven photocatalysts.

Future work will need to address a few key issues, such as improving efficiency over dozens of runs, finding lasting solutions to the air and humidity sensitivity of phosphorene, and being effective enough to replace toxic heavy metals currently used in devices. On the topic of toxicity, working with phosphorus creates inherent risk, as white phosphorus production is a real and dangerous issue in the field. Caution must always be taken when working with phosphorus allotropes. However, even with the drawbacks and hazards, phosphorus is proving to be the latest in a series of wonder materials as technology shifts to the nanoscale. It is also worth noting that while a lot of research has been done on black phosphorus nanomaterials, there are far fewer papers on the properties of red phosphorus. From the works that were covered in this review, it seems that red phosphorus could be the next material investigated for its optical properties.

Chapter 2: Liquid Exfoliation of 2D Black Phosphorus

2.1 Introduction

Modern research into nanotechnology was arguably inspired by the discovery of buckminsterfullerene (C_{60}) in 1985.[50] Carbon has proven to be an incredibly versatile element, forming a wide array of new allotropes and new nanostructures that can be used in a variety of applications. While the structure of graphite was identified in 1924, the material that would come to be known as graphene was first theorized in 1947.[51-53] In a 2004 paper by Novoselov et al, mechanical exfoliation via adhesive tape was employed to bulk graphite in a process that would come to be known as the Scotch-tape Method.[54] However, it would still be another 10 years before Liu et al applied this method to bulk black phosphorus.[15] Another dry transfer method that has been developed uses a viscoelastic material (Gel-Film®) adhered to a glass slide as a stamp by using mechanical exfoliation from bulk material.[55] Since no wet chemicals are used in this process, possibility for contamination is reduced and materials are saved. The paper claims that this process can be done in 15 minutes with practically 100% yield.[55] The paper also states that this process can be utilized for fabricating heterostructures, nanomaterials composed of different 2D layered materials, which have been reported for graphene, hexagonal boron nitride, and TMDs.[56-58]

Liquid exfoliation of layered materials is not a new technique in the development of 2D nanosheets, with research going back decades.[59] While there are four main types of liquid exfoliation (oxidation, intercalation, ion exchange, and sonication-assisted), oxidation will not be discussed for the sake of this work, as it appears unique to graphene.[60]

Liquid exfoliation techniques were first introduced as a solution to the large-scale production problem associated with mechanical exfoliation.[61-63]

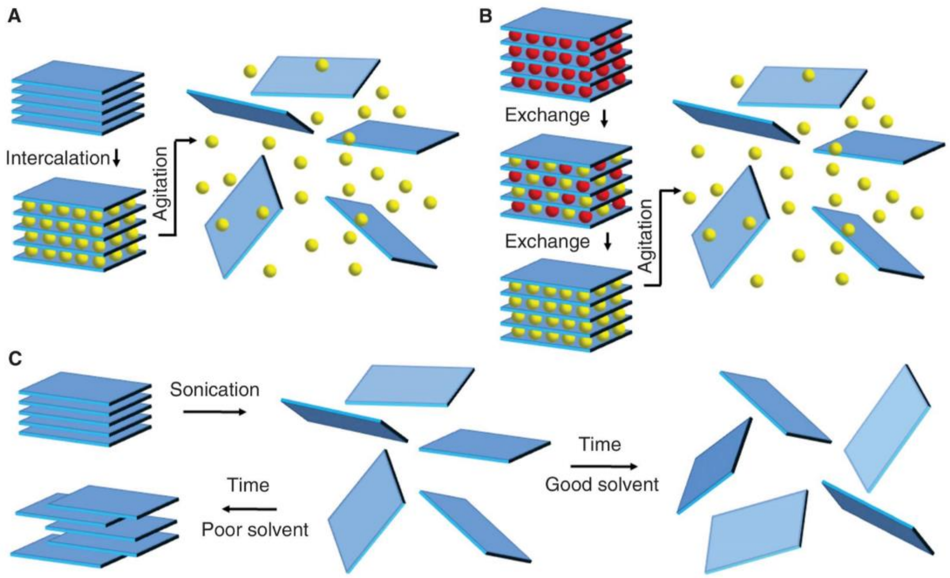

Figure 2.1 – Schematic description of the main liquid exfoliation mechanisms. (a) Ion intercalation. (b) Ion exchange. (c) Sonication-assisted exfoliation.[60]

Figure 2.1 illustrates the three main types of liquid exfoliation. In ion intercalation (Figure 2.1a), ions in yellow are intercalated between the layers of bulk solid in a liquid medium, swelling the crystal and weakening the van der Waals attractive forces, then agitation (shear forces, ultrasonication, or thermal) can separate the layers, resulting in an exfoliated dispersion.[60] Many transition metal dichalcogenides contain counterions between layers to balance surface charges.[64-65] The counterions, in red (Figure 2.1b), can be exchanged in a liquid environment for other, often larger ions, shown in yellow. As with intercalation, agitation results in an exfoliated dispersion.[60]

Sonication-assisted exfoliation does not require a solute to intercalate, but rather relies on a specialized solvent. However, there are cases in which an added compound can act as a mechanical wedge, such as a surfactant, NaOH, or naphthalene.[66-68] First described in 2014 with black phosphorus, bulk BP was exfoliated in *N*-methyl-2-pyrrolidone (NMP) at a concentration of 5 mg/mL using sonication (820 W at 37 kHz and 30% power) for 24 hours at a constant temperature below 30°C.[63] Purification occurred by centrifugation to remove larger solids, then spin-coating the solution onto a SiO_2/Si substrate at 6000 rpm to avoid restacking of the phosphorene sheets.[63] The various shapes and sizes of phosphorene obtained, with the largest in size being about 200 nm x 200 nm and a thickness of 3.5–5 nm, suggests that the flakes were 3-5 layers thick. While 1-2-layer thick phosphorene was also made according to the AFM data, these flakes were only 20 nm x 20 nm in size. The paper hypothesizes that increasing the sonication time to 48 hours will break down the thicker flakes into these 1-2-layer sheets.[63]

Using a similar process, Woomer et al performed a test of 18 different compounds to study the solvent effects on the concentration of phosphorene in solution (see Table 2.1). Approximately 10 mg of black phosphorus was added to 20 mL of each solvent and sonicated for 13 hours under anhydrous and air-free conditions.[69] The suspensions were centrifuged at 3000g for 30 minutes to remove unexfoliated BP, which was further purified via dialysis to remove small (< 2.5 nm) phosphorus fragments.[69] Woomer et al determined that benzonitrile was the best candidate for sonication-assisted exfoliation of phosphorene among their tested solvents.

Table 2.1 – Organic Solvents Used in Liquid Exfoliation of Black Phosphorus.[69]

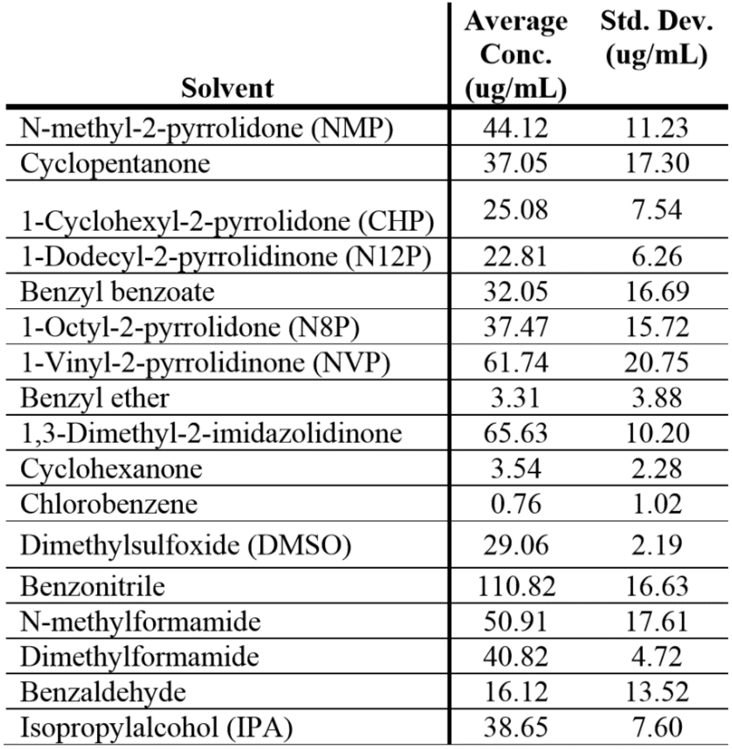

Solvent	**Average Conc. (ug/mL)**	**Std. Dev. (ug/mL)**
N-methyl-2-pyrrolidone (NMP)	44.12	11.23
Cyclopentanone	37.05	17.30
1-Cyclohexyl-2-pyrrolidone (CHP)	25.08	7.54
1-Dodecyl-2-pyrrolidinone (N12P)	22.81	6.26
Benzyl benzoate	32.05	16.69
1-Octyl-2-pyrrolidone (N8P)	37.47	15.72
1-Vinyl-2-pyrrolidinone (NVP)	61.74	20.75
Benzyl ether	3.31	3.88
1,3-Dimethyl-2-imidazolidinone	65.63	10.20
Cyclohexanone	3.54	2.28
Chlorobenzene	0.76	1.02
Dimethylsulfoxide (DMSO)	29.06	2.19
Benzonitrile	110.82	16.63
N-methylformamide	50.91	17.61
Dimethylformamide	40.82	4.72
Benzaldehyde	16.12	13.52
Isopropylalcohol (IPA)	38.65	7.60

It should be noted that a comprehensive review on the fabrication of phosphorene was recently published by Dhanabalan et al, and many of these publications are expanded upon in this work.[70]

2.2 The Drawbacks of Sonication

The use of sonication suffers from several drawbacks. The acoustic pressure created by sonication forms small bubbles between the layers in the bulk material. After reaching a critical size, the bubbles collapse with a gas-phase reaction zone effective temperature of 5200 ± 650 K, and the liquid-phase effective temperature is approximately 1900 K.[71] The ensuing shockwaves then break bulk flakes into thin layers by adding mechanical energy in the form of tensile stress to circumvent the attractive interactions between the layers.[72] However, fragmentation can occur in the vicinity of the bubbles, decreasing the overall surface area and creating many smaller flakes as opposed to one large flake, complicating large-scale synthesis of few-layer nanomaterials. Edge defects are consequently induced after prolonged ultrasonic irradiation, causing an increase in surface polarity.[72] For example, dangling carbon atoms situated at the edge of graphene sheets, when exposed to an ultrasonic bath at temperatures above 40°C, tend to react with radicals or ions resulting from the decomposition of water or air upon cavitation, leading to the formation of hydroxyl, carboxyl, or epoxy groups in graphene.[72]

This phenomenon is not unique to graphene sheets. Intensive ultrasonication of molybdenum disulfide, MoS_2, in isopropyl alcohol (IPA) (20 kHz, 500 W, probe diameter d = 3 mm, 30% amplitude) not only favored exfoliation, but also induced fragmentation of layers, leading to rupture of Mo–S–Mo bonds and exposure of coordinatively unsaturated Mo and S species, which can then react with IPA and/or atmospheric oxygen, generating surface hydroxyl, alkyl, and, to a lesser extent, oxidized species such as sulfate, carbonylic, and carboxylate groups (see Figure 2.2).[72-73]

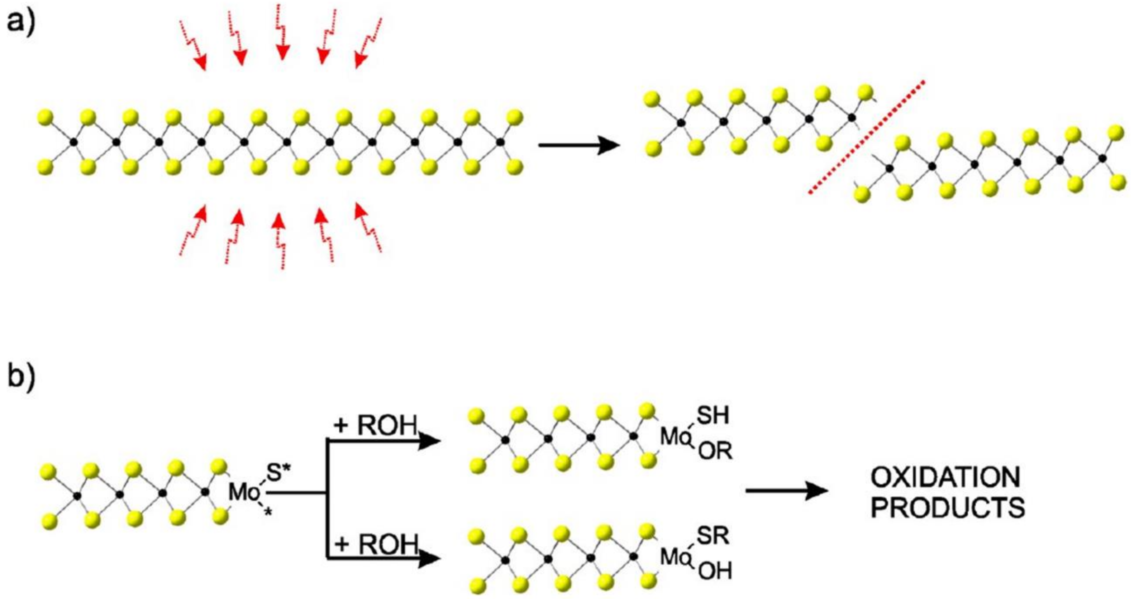

Figure 2.2 – (a) Breaking of the Mo–S–Mo bonds in MoS_2 due to energetic ultrasonication. (b) Reactions of fragmented MoS_2 with alcohol solvent, with predominant formation of hydroxy and alkoxy groups.[73]

According to the Tao et al review, despite recent advances achieved by optimization of ultrasonic parameters for exfoliation, several issues remain.[72] The exact output power levels on flakes during the process are unclear, in most cases, and the links of ultrasonic parameters and exfoliation dynamics that relate to the yield, quality, lateral size, and thickness of nanosheets need to be further explored.[72]

Liquid exfoliation techniques require agitation after diffusion of the target molecules or ions between layers. In this work, sonication-assisted exfoliation with surfactant will be tested and research into sonication-less exfoliation will be investigated using thermal agitation and applied solely to black phosphorus.

2.3 Sonication-Assisted Exfoliation of 2D BP with Surfactant

Synthesis of phosphorene flakes from bulk black phosphorus on the order of 1-5 sheets thick is well understood in the literature. Current deficiencies lie in the synthesis of large surface area sheets for mass production. Loosely following a liquid exfoliation procedure from Kang et al,[66] a black phosphorus crystal was placed in a 2% wt/vol solution of sodium dodecyl sulfate (SDS) in water (0.41 ± 0.001 g of SDS in 20 mL H_2O). Upon sonication, the SDS acts as a surfactant, wedging itself between the phosphorene sheets within the bulk black phosphorus, allowing for the sheets to be separated without the use of organic solvents. Rather than running this sonicated solution through a centrifuge to separate out the thick flakes, a clean SiO_2/Si substrate was placed in a Büchner funnel and the solution was vacuum filtrated. This was done to perform a quick test of a trivial transfer method applied to black phosphorus that was developed by the American Chemical Society (ACS) for graphene.[74] DI water was used to wash away the large chunks of bulk black phosphorus during vacuum filtration. The substrate contained a visible transparent film across the surface.

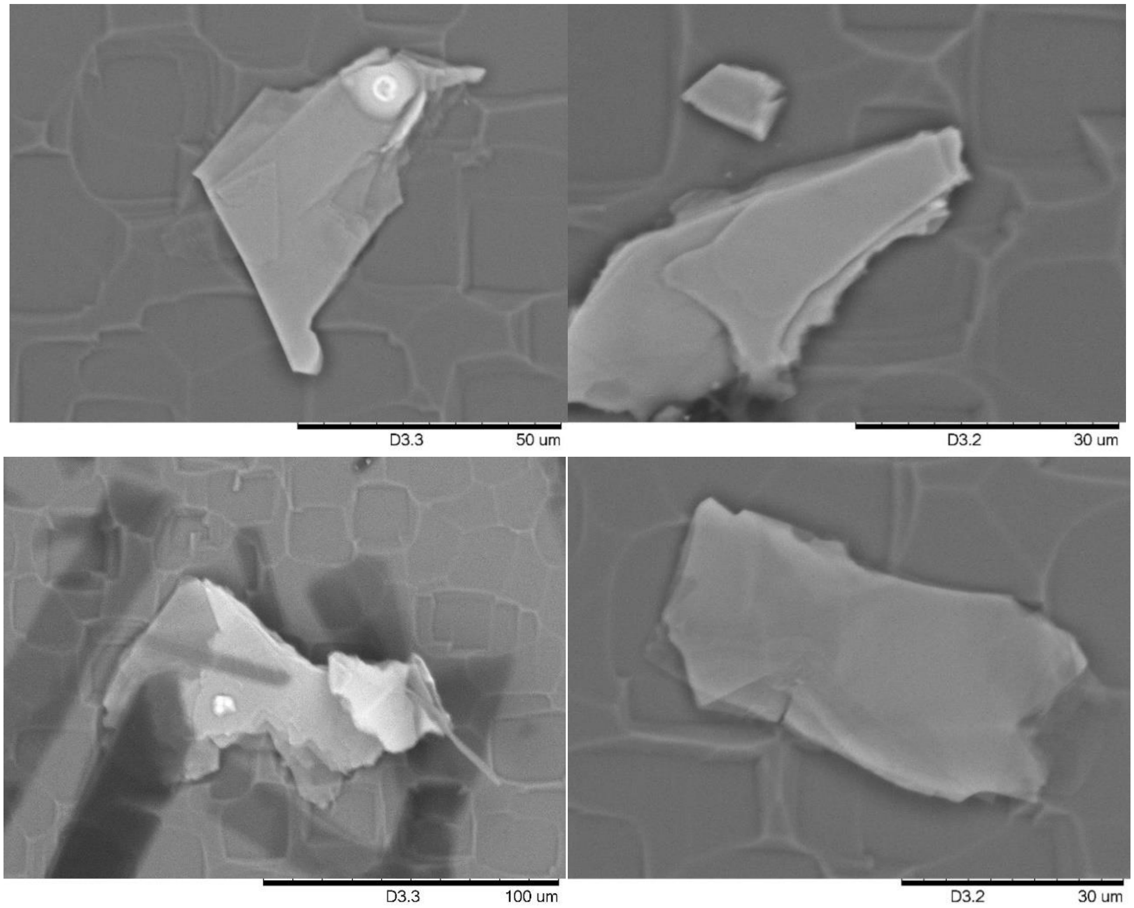

Figure 2.3 – SEM images of black phosphorus flakes at various magnifications on an SiO_2/Si substrate.

Background images appear to be the rough silicon surface. The obtained flake sizes were insufficient to perform the transfer method. This method demonstrates that black phosphorus can be successfully exfoliated using a surfactant, however due to ultrasonication of the solution, flake sizes do not exceed 100 microns in length. While the flakes in Figure 2.3 are tens-to-hundreds of layers thick, thinner flakes were not observed. For larger black phosphorus thin films, a technique must be developed without the damaging effects of sonicating the material.

2.4 Exotic Solvent Exfoliation

2.4.1 Experimental Procedure

A series of both common and exotic laboratory solvents (see Table 2.2) were used to exfoliate 2D BP without the use of sonication. The 0.88M BF_3 solution was prepared from boron trifluoride etherate and hexanes for this experiment, however this sample will be expanded upon in Chapter 3.

Table 2.2 – Common and Exotic Solvents Used in Liquid Exfoliation.

Solvent	Type		Solvent	Type
Ethylbenzene/Cyclohexanol	1:1 Mix		CCU in EtOH	DES
6M HCl	Acid		CCTU in EtOH	DES
20 wt% t-Butanol	Alcohol		Chlorobenzene	Halogenated
Cyclohexanol	Alcohol		Chloroform	Halogenated
Benzene	Aromatic		Saturated NaCl	Ionic
Ethylbenzene	Aromatic		Saturated NH_4Cl	Ionic
Nitrobenzene	Aromatic		[BMIM]PF_6	Ionic Liquid
Pyridine	Aromatic		Acetone	Ketone
Toluene	Aromatic		MEK	Ketone
Xylenes	Aromatic		0.88M BF_3	Lewis Acid
10 wt% KOH	Base		Aqua Regia	Oxidant
Glacial Acetic Acid	Carboxylic Acid		Piranha Solution	Oxidant

The ethylbenzene and cyclohexanol mixture was prepared in a 1:1 mole ratio. Aqua regia was prepared using concentrated HCl, then adding concentrated HNO_3 until a yellow color appeared, which results from an approximate 1:3 ratio of HNO_3 to HCl.[75] A variation on piranha solution was prepared using equal parts concentrated H_2SO_4, water, and a 30% H_2O_2 solution.

A deep eutectic solvent (DES) generally consists of two different solid compounds that when mixed together form a liquid at room temperature, and can come in four variations or ‘types’[76] (see Table 2.3), with choline chloride, a quaternary-ammonium salt, being a common choice for one part of the mixture.[77-78]

Table 2.3 – Classification of Deep Eutectic Solvents (DESs).[76,78]

Type I	Quaternary ammonium salt + metal chloride
Type II	Quaternary ammonium salt + metal chloride hydrate
Type III	Quaternary ammonium salt + hydrogen bond donor
Type IV	Metal chloride hydrate + hydrogen bond donor

Choline chloride (Alfa Aesar, 98+%), urea (J. T. Baker, certified), and thiourea (Fisher Scientific, certified) were weighed out in several different molar ratios to prepare two type III DESs for the exfoliation process (see Table 2.4).[79-81]

Table 2.4 – Weighed Masses of Choline Chloride (CC), Urea (U), and Thiourea (TU) and Molar Ratios of CCU and CCTU DESs.

Mass of CC (g)	Mass of U (g)	Mass of TU (g)	CCU (mol:mol)	CCTU (mol:mol)
1.22	1.15	-	1:2.19	-
1.24	0.80	-	1:1.50	-
1.36	0.62	-	1:0.94	-
2.35	0.49	-	2.06:1	-
2.02	-	0.55	-	1:2.00

Upon heating the vials in a water bath, the vial of 1:2.19 CCU melted first, followed by 1:1.50, and lastly the 1:0.94 ratio; the 2.06:1 CCU was the only sample not to completely liquify. All four ratios were kept in a vacuum oven for 2.5 hours to remove any excess water exposure from the original heating, where once again all samples liquified except the ratio with choline chloride in excess. Forty minutes after the samples were removed from the vacuum oven, the 2.06:1 CCU was completely solid, the 1:0.94 had mostly solidified, the 1:1.50 had large visible crystals throughout, but the 1:2.19 CCU only had small crystals on the bottom of the vial. After many hours, the 1:2.19 CCU DES showed no further signs of crystallization, thus this ratio was selected for experimentation. Ethanol (EtOH) was added to the vial to make a 50:50 volumetric mix of CCU to EtOH, based on previous work.[82] Light heating was applied to dissolve the rest of the CCU crystals. A pressure build-up was noted, as the lid popped off multiple times upon standing in ambient conditions due to the vapor pressure of warm unmixed ethanol.

The CCTU mixture was heated in a vacuum oven for 43 minutes. The mixture had mostly liquified, but there was still a large solid mass in the center of the liquid that would not melt. Twice the volume of EtOH was added to produce a 1:2 ratio of CCTU:EtOH, however the CCTU had solidified completely prior to the addition of EtOH. The ethanol did not appear to be mixing with the CCTU as a second liquid phase was evident, and light warming of the vial had little-to-no effect on the solution. The solution was heated at low power and stirred with a magnetic stir bar for about 10 minutes, with the stir bar providing strong mechanical mixing against the glass vial, breaking up the solid chunks as the heating dissolved the CCTU into the EtOH.

Black phosphorus crystals were synthesized using methods previously reported in the literature.[4,83-84] In brief, two previously run sealed ampules containing tin powder, tin(IV) iodide, unreacted RP, and small synthesized BP crystals were supplied by colleague Pedro E. Martins Amaral. While the exact amounts of each compound were unspecified, they were measured out according to previous literature reports.[4,83-84] It was hypothesized that running this reaction a second time would increase the yield of black phosphorus crystals. The heating and cooling ramp for the sealed ampules can be found in Figure 2.4, with reported temperatures being the temperatures set on the oven and not necessarily the temperature of the ampules themselves. The starting temperature of 300°C was raised straight from room temperature and left there for over a day to ensure an even temperature distribution. The ampules were kept at 600°C for 20 hours. After the ampules were kept at 500°C upon cooling for 3.5 hours, the oven was then turned off, and the ampules were left to cool in ambient conditions.

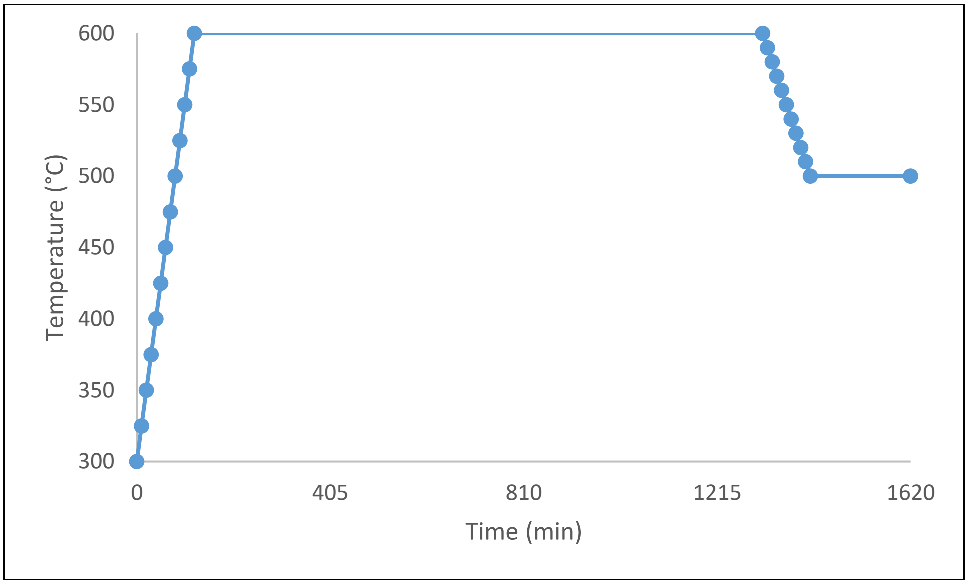

Figure 2.4 – Heating (25°C/10 min) and cooling (10°C/10 min) ramp for black phosphorus synthesis.

The two sealed ampules were cracked open, revealing dozens of large BP crystals. The glass shards were soaked for 20 minutes in hot toluene (Baker, certified) and the solution turned a deep yellow color. After waiting the 20 minutes, the shards were filtered using a Büchner funnel and Kitasato flask under vacuum. After scraping the black phosphorus from the shards and collecting the crystals, they were put in a vial with acetone, but still demonstrated a deep yellow color, suggesting high impurities. After rewashing in room temperature toluene and acetone, the crystals showed a faint hue of yellow under a new volume of acetone. After a third soaking of the BP crystals in hot toluene for 10-15 minutes, the crystals were vacuum filtered and washed with acetone. On this wash, a white precipitate with a spot of light green came out of the solution. This will be expanded upon in the next section. The BP crystals under acetone continued to show a yellow color in the solvent. After a fourth wash for 20 minutes in about 75 mL of boiling acetone, the crystals were vacuum filtrated again with additional room temperature acetone. The crystals were placed in a small capped vial of acetone and showed only a faint hue of yellow within the solvent. The BP crystals were washed for a fifth and final time with room temperature acetone using a Büchner funnel and Kitasato flask.

Approximately 1-2 mL of each solvent was placed in a screw-cap vial with small crystals of black phosphorus. These samples were then capped and wrapped with Parafilm, labeled, and dated to test whether exfoliation from bulk would occur with time.

2.4.2 Results and Discussion

The solvents sat undisturbed and were observed over the course of a month. Many of the solvents had no effect on the exfoliation of 2D black phosphorus, however, a notable few had positive results.

The ethylbenzene sample developed yellow bubbles/droplets at the bottom of the vial about a month after it was prepared (Figure 2.5a). The sample also developed a yellow bubble around the black phosphorus crystal (Figure 2.5b). A second sample of ethylbenzene and black phosphorus was prepared to reproduce these results. This is potentially significant, as few-layer phosphorene dispersions demonstrate a yellow color in solution.[66]

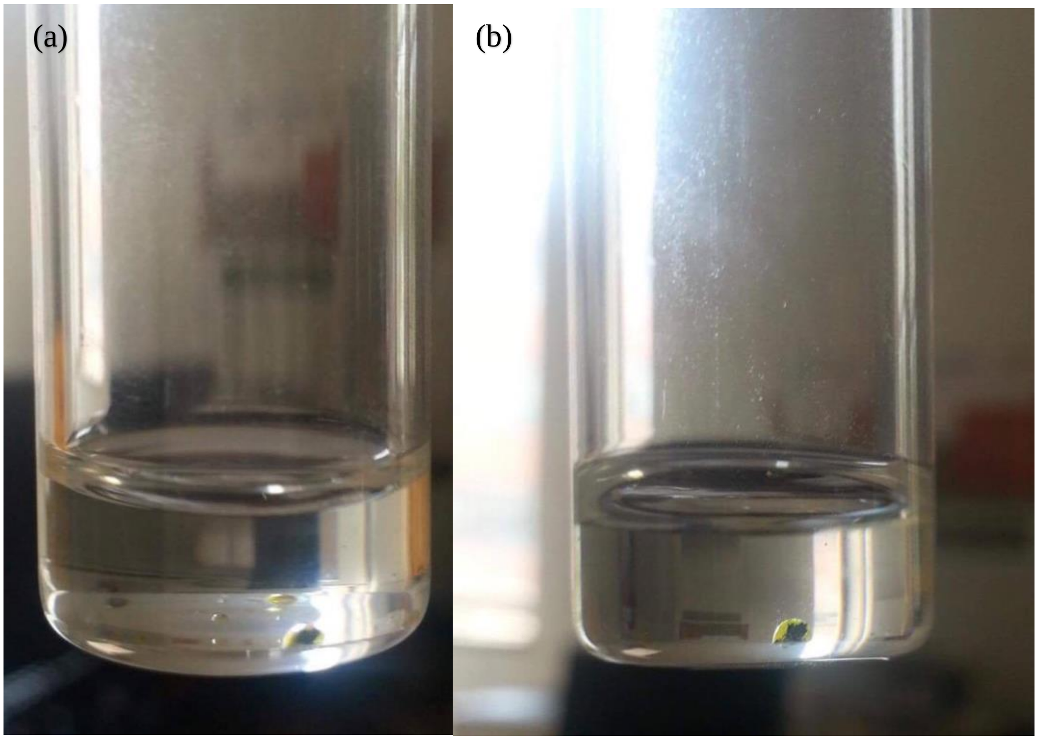

Figure 2.5 – BP in ethylbenzene sample. (a) Yellow droplets formed in solution. (b) Yellow bubble formed around BP crystal.

These droplets appear to be immiscible in the ethylbenzene solvent, leading to the liquid beading up rather than mixing into a solution. This could mean that the yellow solution is not 2D BP exfoliated by ethylbenzene, but impurities extracted from the BP crystals. A syringe and needle were used to extract the yellow solution. The solution was dried out and resulted in a white solid, which was then submitted for mass spectrometry (MS) analysis. The spectrum demonstrated the solid was phosphorus-rich, with phosphorus oxides potentially existing in the spectrum (see Figure 2.6). This shows that the yellow solution does in fact contain phosphorus, and the solution was oxidized when exposed to air, as 2D BP has been shown to do.[15,42]

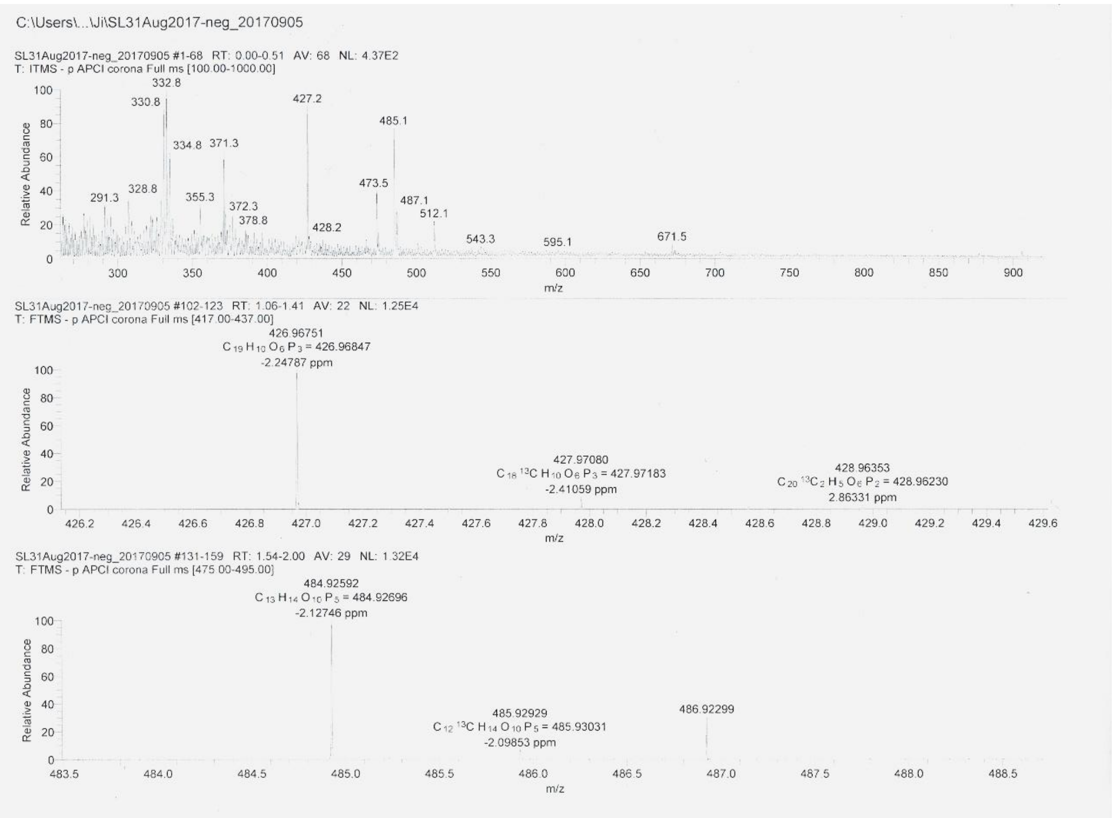

Figure 2.6 – Hi. res. (exact mass) chemical ionization (CI) MS analysis of yellow droplets from ethylbenzene solvent in methanol.

The lone pairs on the phosphorus atoms lead to its reactivity upon air exposure, leading to the degradation of the material's desirable properties over time.[85] Research has been done to form a protective, stable oxide layer at the surface of 2D black phosphorus.[86] Exfoliation experiments have been done with graphene oxide, however exfoliation techniques have not been attempted with oxidized, layered black phosphorus.[87] Aqua regia and piranha solution were used to test if oxidizing acids would rapidly or slowly oxidize black phosphorus, and if they could potentially yield pristine flakes protected by layers of oxidized phosphorus. Upon adding the black phosphorus crystal to aqua regia, the crystal immediately reacted with the oxidant, producing a small amount of smoke until the crystal was gone. While the sample in piranha solution did not immediately vanish like with aqua regia, it was gone within the course of a day, although no smoke was observed. Since testing could not be conducted on these samples, other common laboratory acids were used instead. Interestingly, acid alone (6M HCl and glacial acetic acid) had seemingly no effect on the BP crystals; nor did base (10 wt% KOH).

Only days after adding the BP crystal to the ionic liquid [BMIM]PF_6 (1-butyl-3-methylimidazolium hexafluorophosphate), small pieces of black phosphorus appeared to break away from the bulk material, demonstrating that the solvent was exfoliating the sample (Figure 2.7). It is worth noting that the low quality of the optical microscope images is due to the fact that the microscope does not operate well with liquid samples. These are included only to demonstrate that the very small flakes existed in the sample.

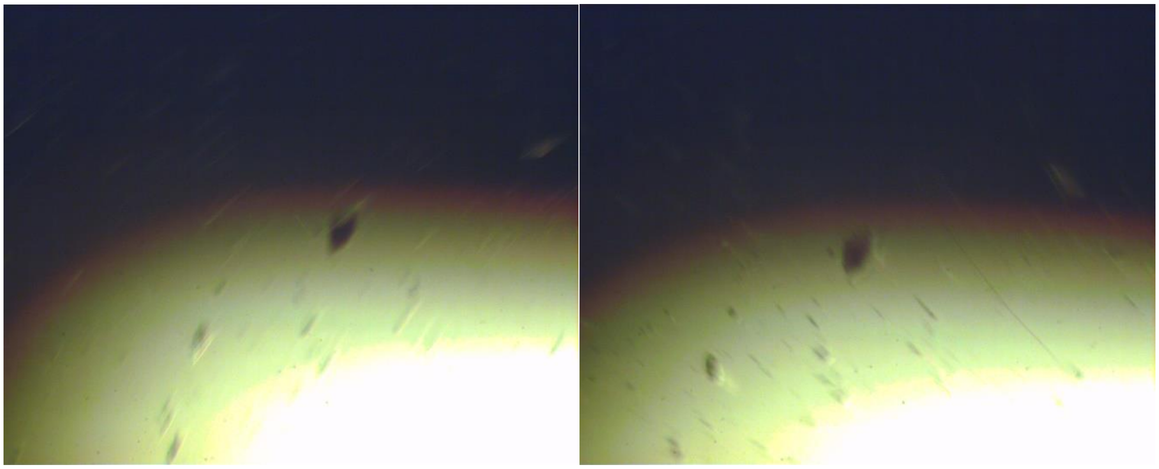

Figure 2.7 – Optical microscope images of black phosphorus flakes in [BMIM]PF_6 at 15x magnification.

A 200-nm pore-sized alumina filter was used for vacuum filtration of the [BMIM]PF_6 in the hopes that it would remove the solvent, however the ionic liquid was too viscous for filtration. The Büchner funnel and Kitasato flask were left on the vacuum line for several days to see if filtration would occur at a slower rate, but this had no effect. An ethanol-DI water (Milli-Q®) mixture was added, as ethanol-water mixtures have been shown to dissolve [BMIM]PF_6 in previous studies.[88] However, while this dissolved the ionic liquid, it also broke apart the alumina where the ionic liquid sat, allowing the suction to break holes in the remaining plastic layer underneath. It is uncertain what caused this result.

Several large chunks of the white precipitate from the BP crystal purification were kept for analysis. A mass spectrometry analysis could not be performed, as the solid did not dissolve in toluene, dichloromethane, xylene, or dimethylformamide (DMF). SEM images of the precipitate can be seen in Figure 2.8.

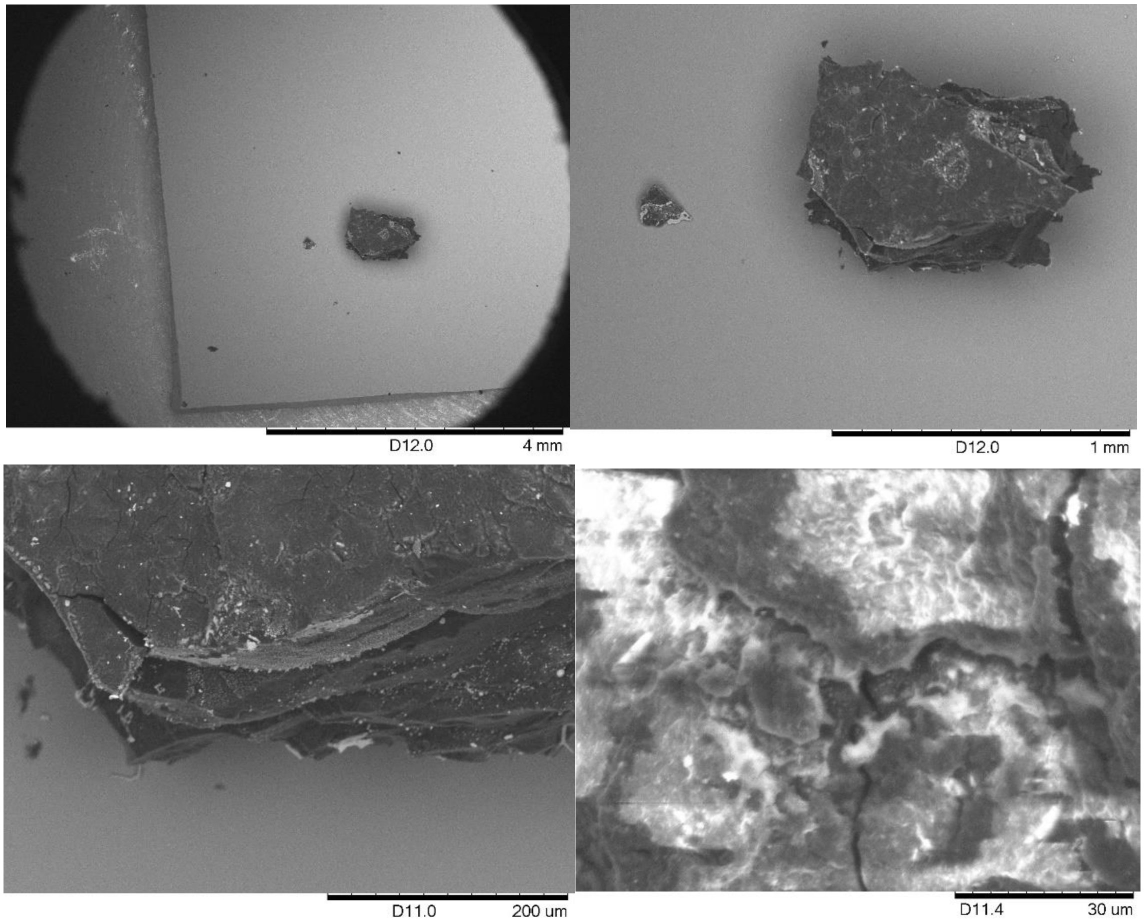

Figure 2.8 – SEM images of unknown precipitate at various magnifications on Si/SiO_2 substrate.

A UV-Vis absorption spectrum of the yellow solution from the BP-in-acetone vial was obtained using acetone in a quartz cuvette as a blank (see Figure 2.9).

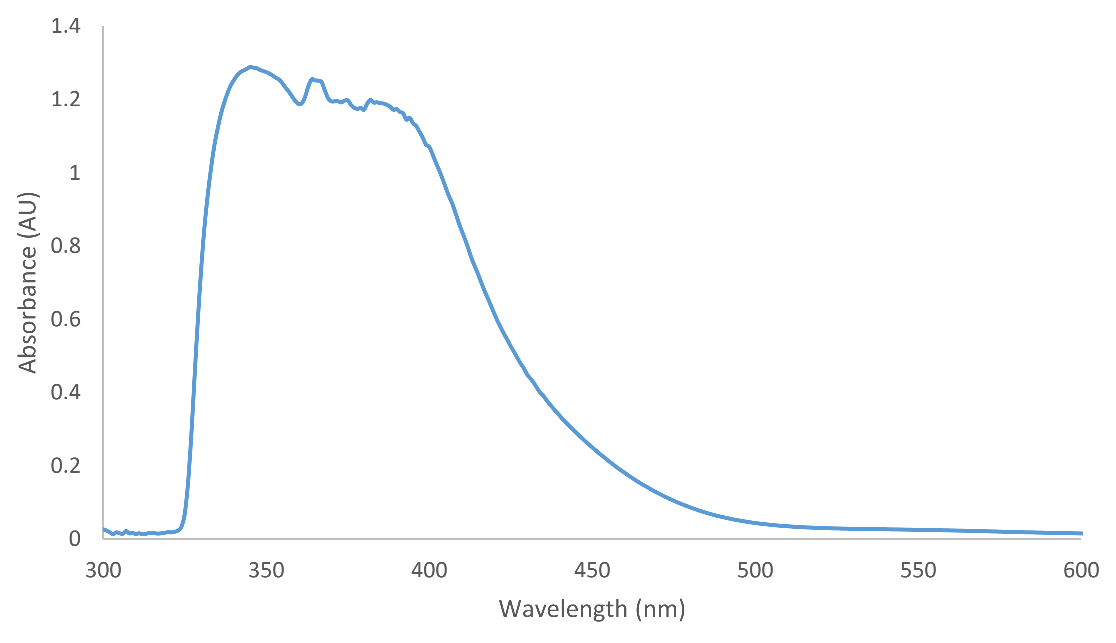

Figure 2.9 – Absorption spectrum for the yellow acetone solution.

The spectrum shows an interesting response similar to the absorption spectra for tin(IV) oxide, SnO_2, and the triiodide ion, I_3^-.[89-91] Tin(IV) oxide can be produced when the SnI_4 catalyst reacts with water and then undergoes thermal decomposition:[92-93]

$$SnI_4 + 4\,H_2O \rightarrow Sn(OH)_4 + 4\,HI \tag{2.1a}$$

$$Sn(OH)_4 \xrightarrow{\Delta} SnO_2 + 2\,H_2O \tag{2.1b}$$

These reaction conditions are met with ambient water and exposure to the hot toluene solvent during purification of the BP crystals. Elemental iodine can be formed from the decomposition of tin(IV) iodide, and while stoichiometric amounts of tin powder are added to avoid this, it is still possible for small amounts of I_2 to form.[84] This can further react with iodide ions from the SnI_4 catalyst, forming the triiodide ion:

$$I_2 + I^- \rightleftharpoons I_3^- \tag{2.2}$$

Another notable I_3^- peak is missing from the spectrum at 300 nm.[90] However, low concentration iodine can turn an organic solution yellow, further leading to the hypothesis that this reaction had occurred. It is still unknown what the solid impurity was, but SnO_2 is a potential candidate.

2.4.3 Conclusion

Liquid exfoliation of black phosphorus from bulk without sonication has shown promise. While 2D flakes of black phosphorus were not confirmed, the ionic liquid [BMIM]PF_6 showed the solvent can break off smaller pieces of BP from bulk with no additional assistance (heat, sonication, etc.). Ethylbenzene demonstrated yellow liquid droplets in solution, which when exposed to air dried into a white solid. Mass spectrometry analysis demonstrated this solid contained phosphorus-rich compounds, proving that phosphorus was pulled from the bulk crystal. Aqua regia and piranha solution reacted with the black phosphorus crystals. The nitric acid in aqua regia acts as a powerful oxidizing agent to form phosphoric acid. Piranha solution is also a powerful oxidizer; therefore, a similar result is expected.

2.4.4 Future Work

Due to the success of the ionic liquid [BMIM]PF_6 in breaking off pieces of BP from bulk, an ionic liquid study can be conducted to test different anionic species, cationic species, or both. While sonication-assisted studies have already been conducted using ionic liquids,[94-95] studies of solvent effects without the damaging effects of sonication have not, although theoretical studies have suggested that an external stimulus is necessary due to unfavorable exfoliation thermodynamics.[96] A potential replacement for sonication will be explored in the next section.

2.5 The Freeze-Thaw Method

2.5.1 Background

The freeze-thaw method of liquid exfoliation was first introduced in 2014 as an alternative to damaging sonication-assisted exfoliation techniques, as well as costly surfactants.[97] The solvent, water, is flash frozen using liquid nitrogen with the bulk material, then warmed to melt the solution, and repeated a number of times (2-6, ideally) to produce thin flakes (see Figure 2.10).

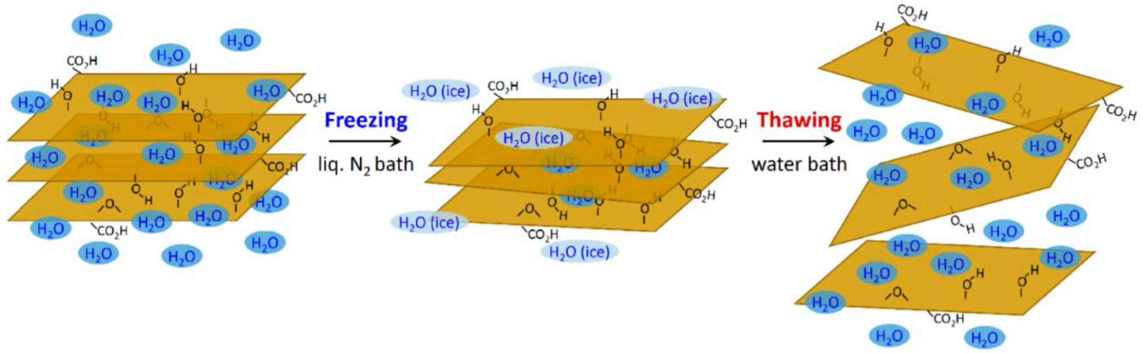

Figure 2.10 – Exfoliation of graphite oxide via rapid freezing of hydrated graphite oxide flakes in water and subsequent thawing of the resultant solid.[97]

This method was used for the exfoliation of graphene oxide (GO) layers. Recent work on GO exfoliation notes that water is an optimal solvent for this method, due to its uncommon freezing behavior; its volume contracts when cooled down to 4°C, slightly expands between 4°C to 0°C, and at 0°C it significantly expands up to 9% upon freezing and is converted into ice.[87] Another benefit of this method actually lies with the choice of bulk material. The distance between graphene oxide planes increases with ambient water, causing the material to swell, because the material contains bulk liquid water molecules intercalated between layers.[98] Thus, as the water between the GO layers freezes, the volume of water increases, which further pushes apart the GO layers. As the ice begins to thaw upon heating, more water fills in the increased space created by the increased volume of ice between layers. Repeated cycles of freezing and thawing will separate the graphitic layers from each other considerably.[87]

Currently, there appears to be nothing in the literature about this method's application to black phosphorus. This opens the door to exploring the freeze-thaw method as an inexpensive alternative to the production of 2D black phosphorus.

2.5.2 Experimental Procedure

A UV-Vis study was conducted to confirm the exfoliation of 2D black phosphorus based on the 2014 work by Ogino et al.[97] Several previously prepared large crystals of black phosphorus were placed in a test tube filled with deionized water and deoxygenated under a Schlenk line of N_2 gas for 30 minutes. Previous work has shown that oxygen concentrations using this method can be reduced to 0.2-0.4 ppm.[99] A large test tube was obtained and washed with DI water and acetone to remove impurities. After 20 minutes in a vacuum oven, the tube was filled with separately degassed DI water to serve as a reserve for the quartz cuvette. Tests were not conducted to determine which was the more important method between degassing or deoxygenating, however and examination of the two methods will be discussed briefly in the next section. To save solution, only 0.5-1 mL of the sample was used and then diluted by a factor of 100 with the degassed DI water.

Degassing of the reserve DI water occurred by putting a glass stopper in a Kitasato flask with the DI water and a stir bar. A vacuum was applied as the stir bar spun, releasing any dissolved gases from the water. This sat for 20 minutes to ensure optimal removal of dissolved oxygen.

Using the degassed DI water as a blank, “Trial 0” was the deoxygenated DI water with the black phosphorus at the bottom prior to the start of the freeze-thaw process, diluted with the degassed water. Rather than using liquid nitrogen for the freezing process, a standard freezer will be utilized to hopefully increase the simplicity of the process, as well as make the method more cost-effective. The temperature of the freezer used is approximately -15°C, as confirmed by a standard mercury thermometer. The sample was left in the freezer for 30 minutes to allow complete freezing of the solution to occur. Only when complete freezing had occurred was the solution thawed in a warm water bath for each trial (see Figure 2.11). The solution was thawed each time in a water bath at approximately 40°C.

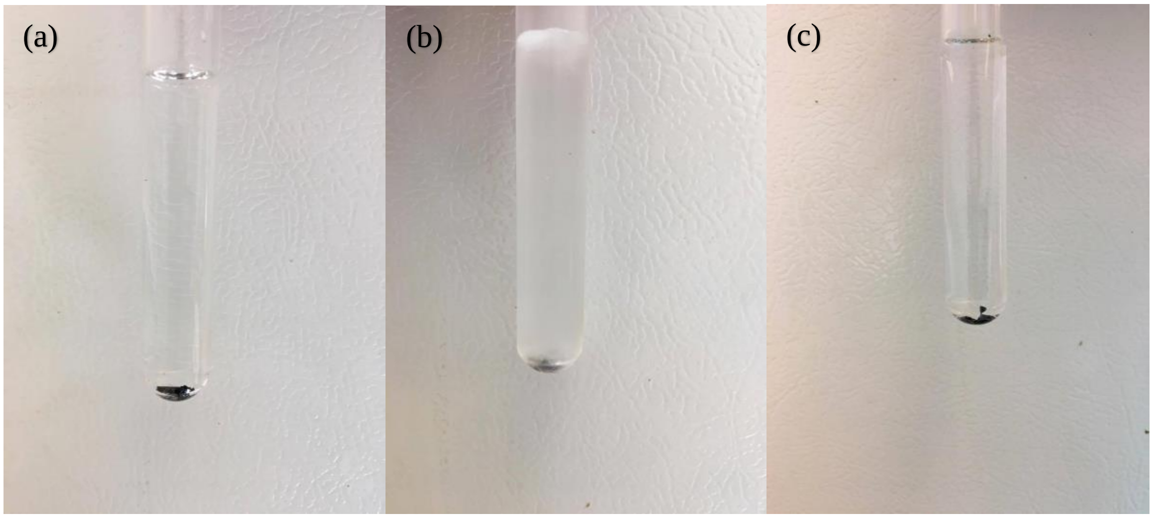

Figure 2.11 – Black phosphorus in Milli-Q® water. (a) Before freezing, (b) after first freezing session, and (c) after first thawing session.

It should be noted that before Trial 3 was taken in the UV-Vis spectrometer, over 3 mL of DI water was added to the solution, which will cause a decrease in the exfoliated black phosphorus concentration, and thus a decrease in the absorbance peak intensities. After Trial 4, the sample was placed in the freezer over the weekend. It is not believed that staying frozen over this time will affect the results.

2.5.3 Results and Discussion

The UV-Vis absorption spectrum for the BP samples increased with each successive freeze-thaw trial (see Figures 2.12-2.14). The spectrum in Trial 3 was decreased in intensity by the addition of 3 mL of Milli-Q® water, so the figures are broken down in sections to demonstrate that the peak intensities increased with each trial except in trials 3 and 4, because the solution was diluted and reduced future trial peak intensities. Spectra were obtained using an Agilent 8453 UV-Vis instrument.

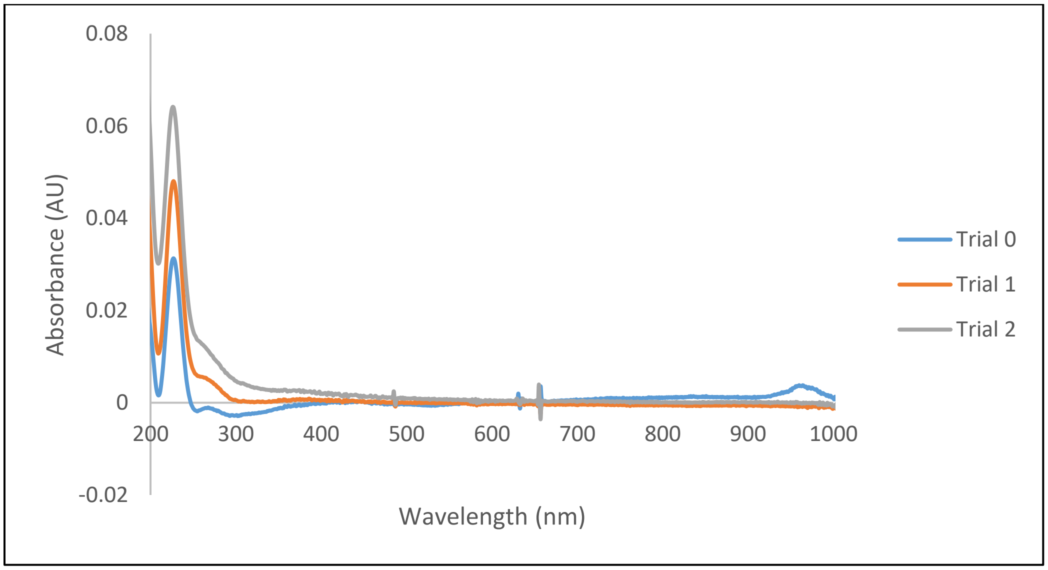

Figure 2.12 – UV-Vis absorption spectra of BP in Milli-Q® water utilizing the freeze-thaw method, Trials 0-2.

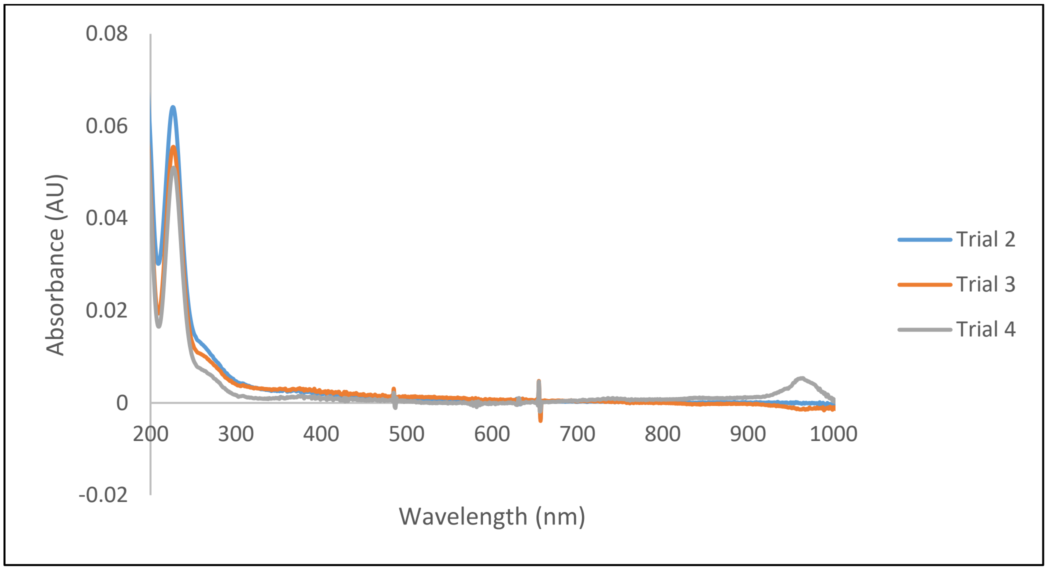

Figure 2.13 – UV-Vis absorption spectra of BP in Milli-Q® water utilizing the freeze-thaw method, Trials 2-4.

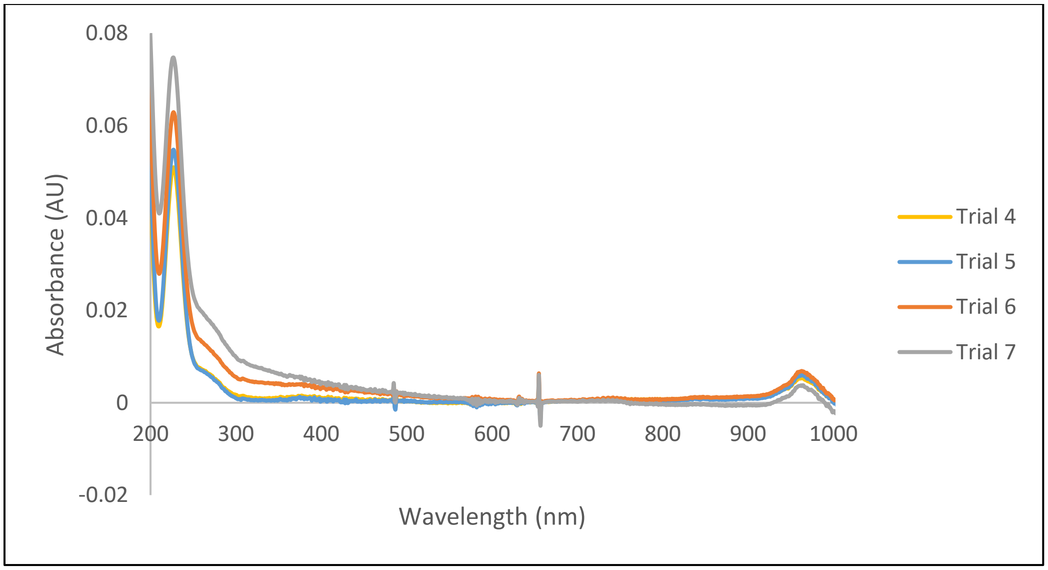

Figure 2.14 – UV-Vis absorption spectra of BP in Milli-Q® water utilizing the freeze-thaw method, Trials 4-7.

The most intense peak corresponded to a wavelength of 227 nm for each trial except for Trial 2, which peaked at 226 nm. There also appears to be a weaker shoulder peak around 270 nm. Spikes in the spectra also appear around 485 nm and 655 nm. However, the most interesting peak during the eight freeze-thaw trials came about between 960-965 nm in the near-IR region. Some of the absorption spectra contain this peak while some do not. It was observed that the reason for this was due to the variation in time in which each spectrum was taken; the peak decreased with time to the point of flatlining if the spectrum was not taken fast enough. These peaks were not due to lamp or filter changes from the instrument, and a blank was run 10-15 minutes after turning the instrument on, then waiting 20 minutes, and running the blank a second time to confirm that this peak was not a baseline glitch. If this peak is due 2D black phosphorus, it could be that any oxygen gas that is still present in the solution, or newly dissolved upon contact with the atmosphere, degraded the thinnest flakes, causing the peak to disappear with time. Table 2.5 compares the peak intensities for 227 nm (Peak 1) and between 960 nm and 965 nm (Peak 2), if present. It is worth noting that after reviewing the data, there appear to be increases in absorbance around 960-965 nm in every trial, but some trials are too small to confidently claim that these are in fact peaks, and their time-sensitivity makes confirming these increases impossible.

Table 2.5 – UV-Vis Peak Maxima for the Freeze-Thaw Trials of BP in DI Water.

Trial	Peak 1 (nm)	Absorbance 1 (AU)	Peak 2 (nm)	Absorbance 2 (AU)
0	227	0.031	960	0.004
1	227	0.048	-	-
2	226	0.064	-	-
3	227	0.056	-	-
4	227	0.051	964	0.005
5	227	0.055	965	0.006
6	227	0.063	963	0.007
7	227	0.075	964	0.004

The values at 227 nm correspond to peaks that have been hypothesized for phosphorene.[100] A 2014 theoretical study by Sa et al plotted absorbance spectra for phosphorene under different tensile stresses (see Figure 2.15). Notable in its absence is the peak between 960-965 nm.

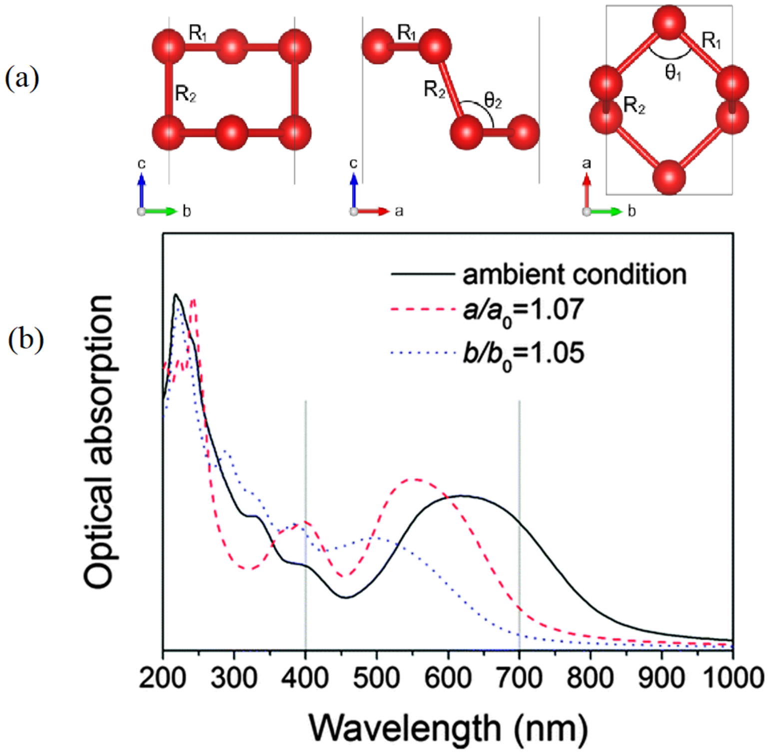

Figure 2.15 – (a) Crystal structure of phosphorene. R_1 and R_2 indicate the intraplanar and interplanar P−P bond length, θ_1 and θ_2 show the intraplanar and interplanar bond angle. (b) Optical spectra for phosphorene at ambient condition, under 7% tensile strain along the a axis, and under 5% tensile strain along the b axis, where the solid vertical lines show the wavelength range of visible light.[100]

The Woomer et al paper obtained absorption spectra for 2D black phosphorus under a variety of centrifugal speeds.[69] Their results can be seen in Figure 2.16, and while their absorbance data only extends to approximately 250 nm and is far broader in width than the peaks obtained in Figures 2.12-2.14, it demonstrates peak maxima that correspond to the peaks obtained in this work. Again, the peak around 965 nm is absent.

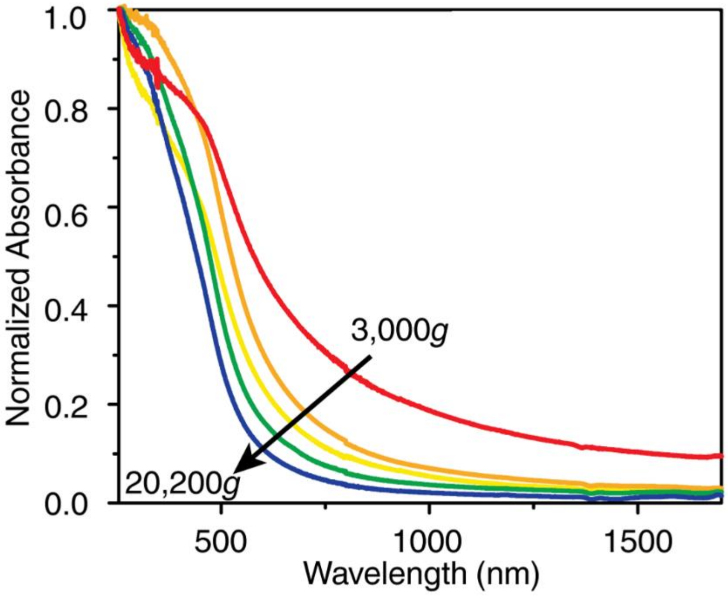

Figure 2.16 – Absorbance of 2D phosphorus suspensions that were prepared by fractionation at relative centrifugal forces (RCFs) near 3.0, 5.9, 9.7, 14.5, and 20.2 thousand g's (red to blue).[69]

To test degradation over time, an aliquot of the deoxygenated BP in DI water sample was added straight to a quartz cuvette with no dilution from the degassed DI water, and several spectra were taken at various times. The results showed only a slow decreasing of the peak around 965 nm. It is worth noting that at the diluted concentrations, the 965-nm peak rapidly decreased with time, whereas the same peak without dilution degraded far more slowly. This could be due to the addition of the degassed DI water, which underwent a different process for removing dissolved oxygen. If more dissolved oxygen existed in the degassed sample, which is likely, then adding it to the deoxygenated sample could have caused faster degradation of the thinner 2D BP flakes.

2.5.4 Conclusion

A UV-Vis absorption experiment has been conducted to demonstrate exfoliation of 2D black phosphorus. With each undisturbed freeze-thaw session, the absorption peak at 227 nm increased. This peak has been demonstrated in previous works to correspond to few-layer phosphorene. A new peak between 960 nm and 965 nm rapidly disappears with time when diluted with degassed DI water, but decreases in intensity far more slowly when not diluted. This could be due to dissolved oxygen reacting with and degrading few-layer phosphorene flakes. With no degradation of the 227-nm peak, it is possible that this peak relates to thicker flakes while the smaller peak corresponds to thinner flakes. Future studies will need to be done to confirm this.

2.5.5 Future Work

Water has been identified as an optimal solvent for this method, due to its uncommon freezing behavior. Future studies can be conducted with other water-based solvents, such as the 20 wt% t-butyl alcohol used in the sonication-less liquid exfoliation study. Other water-based solvents worth testing include SDS and other surfactants, saturated salt solutions at varying saline concentrations, and water-ammonia mixtures for its success in exfoliating hydrophobic materials, such as graphite.[101]

The challenge with this method is determining a solvent that will expand in volume upon freezing. While water is a simple solvent and easily accessible, expanding the method to other solvents could demonstrate superior results. The most common substances that share water’s freezing property are actually elements: gallium, silicon, germanium, and bismuth.[5] Remarkably, while most of these elements have melting points in the hundreds-to-thousands of degrees Celsius, the melting point of gallium is only 29.7646°C (see Table 2.6).[102] This makes pure gallium a candidate for the freeze-thaw method, with only light heating necessary to melt the metal.

Table 2.6 – Densities of Select Elements and Water at Standard Temperature and Pressure (STP) and their Melting Points (MPs).[102-104]

Substance	Formula	Melting Point (°C)	ρ_{STP} (g/cm^3)	ρ_{MP} (g/cm^3)
Bismuth	Bi	271.402	9.79	10.05
Gallium	Ga	29.7646	5.91	6.08
Germanium	Ge	938.25	5.3234	5.60
Silicon	Si	1414	2.3296	2.57
Water	H_2O	0	0.9970470	0.9167

The density value used for water at the melting point is for hexagonal ice, the most common form of ice at ambient pressure (101.325 kPa); supercooled water values were not considered.[103] Certain alloys, such as Wood's metal (about 50% Bi, 25% Pb, 12.5% Cd, and 12.5% Sn by weight, m.p. 70°C), while possessing relatively low melting points, do not have easily accessible data concerning their density changes with temperature, so it is unclear if these alloys would be sufficient for the freeze-thaw method.[105-106] This is possibly due to the numerous variations in amounts of each metal that can occur in simply one alloy, which could lead to future studies on desirable ratios in eutectic alloys that expand in volume upon freezing, should any exist.

While there appears to be nothing in the literature concerning liquid metal as a solvent, liquid gallium has been used as a catalyst/substrate for CVD growth of graphene. A 2014 paper by Zeng et al takes advantage of a liquid's quasi-atomically smooth surface to avoid defects or grain boundaries found with solid metals, removing the need for various complex pretreatments as often required with solid catalysts and reducing restrictions on the need to finely control the growth conditions.[107]

The [BMIM]PF_6 ionic liquid could also be a potential candidate for the freeze-thaw method. With a freezing point of 10°C, a standard freezer is sufficient to solidify the solution.[108] While the volume of [BMIM]PF_6 does not increase upon freezing like with water, as is true of most compounds, the solvent was successful in breaking apart bulk black phosphorus on its own, as discussed previously in this work. Thus, added temperature fluctuations and physical transitions could prove beneficial to the exfoliation process.

Chapter 3: Synthesis of BPO_4 from Black and Red Phosphorus

3.1 Statement of Purpose

In Chapter 2, various common and exotic laboratory solvents were used for the liquid exfoliation of 2D black phosphorus. The 0.88 M BF_3 in hexanes was intended for this experiment, however the solution produced an unexpected result when exposed to air. This work provides evidence that boron phosphate, BPO_4, was produced from the reaction of boron trifluoride, bulk black phosphorus, and exposure to ambient conditions, which would mark the first time BPO_4 has been produced using this method. Reactivity of the starting materials, relevant chemical reactions for the reactants, as well as an infrared spectroscopy study of the product are detailed and investigated in this chapter. The uses and importance of boron phosphate will also be discussed.

3.2 Introduction

3.2.1 Boron Trifluoride

Boron trifluoride (BF_3) is a volatile non-polar molecule of trigonal planar geometry. BF_3 forms a range of complexes with ethers, nitriles, and amines, and is commercially available as the sp^3-hybridized adduct $(CH_3CH_2)_2O{\cdot}BF_3$ (boron trifluoride etherate).[109] Being a liquid at room temperature, it is a convenient means of handling BF_3, which has many applications as a catalyst in organic reactions such as Friedel–Crafts alkylations and acylations.[109]

Unlike other common boron trihalides, which react with water to form boric acid and hydrogen halides, boron trifluoride creates a side product, fluoroboric acid:[109]

$$BX_3 + 3\,H_2O \rightarrow B(OH)_3 + 3\,HX \qquad X = Cl, Br, I \tag{3.1a}$$

$$4\,BF_3 + 6\,H_2O \rightarrow 3\,[H_3O]^+ + 3\,[BF_4]^- + B(OH)_3 \tag{3.1b}$$

This is because the ions $[BCl_4]^-$, $[BBr_4]^-$, and $[BI_4]^-$ are stabilized only in the presence of large cations, such as $[^nBu_4N]^+$.[109] This means 75% of the boron available to create boric acid is lost in the creation of the tetrafluoroborate ion. Fortunately, tetrafluoroborate can further hydrolyze under the following reaction:[110]

$$BF_4^- + 3\,H_2O \rightleftharpoons H_3BO_3 + 3\,H^+ + 4\,F^- \tag{3.2}$$

This means that under very dilute conditions, fluoroboric acid (HBF_4) will produce H_3BO_3.

While boron trifluoride etherate is a clear liquid, as the solution is kept, the adduct will slowly oxidize due to air exposure, darkening the liquid from clear to yellow and eventually brown.[111] This is true of other BF_3 adducts as well.[112]

3.2.2 Degradation of Few-Layer Black Phosphorus

Briefly discussed in Chapter 1, few-layer black phosphorus and phosphorene degrade under ambient conditions.[15,42] While it has been understood that ambient conditions are responsible, there is debate in the literature as to whether oxygen or water is to blame.[85,113] Figure 3.1 demonstrates the proposed breakdown of black phosphorus in water with reaction energy ΔE = -1.2 eV.[114]

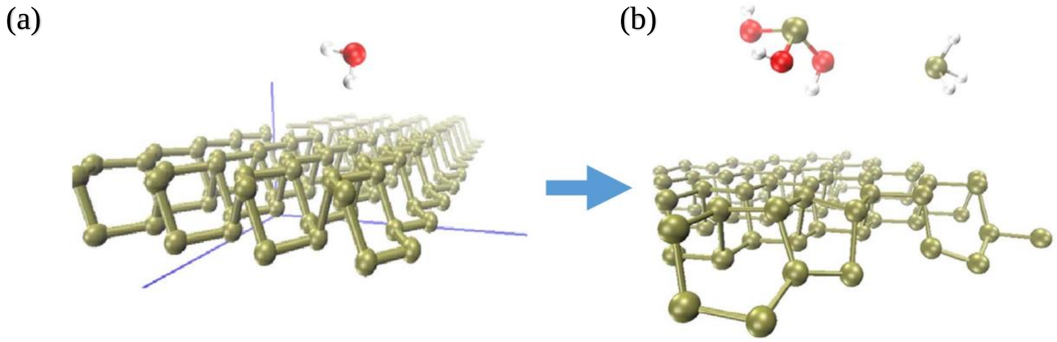

Figure 3.1 – Edge selective degradation model for BP exposed to pure neutral water. Green, red and white spheres represent P, O, and H atoms, respectively. (a) Reactants (BP edge + three water molecules). (b) Reaction products (BP defective edge + phosphine gas (PH_3) + phosphorous acid (H_3PO_3)).[114]

Recent research suggests that black phosphorus is in fact mostly stable in deoxygenated water, however oxygen gas in conjunction with ambient water is to blame for the degradation of few-layer black phosphorus (see Figure 3.2).[113-115]

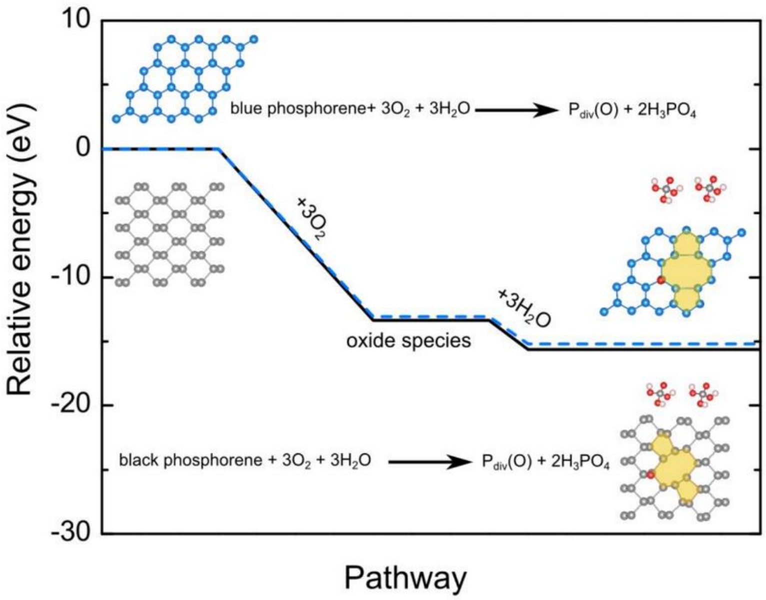

Figure 3.2 – Relative energy for reactions of black (solid curve) and blue (dashed curve) phosphorene with O_2 and H_2O. $P_{div}(O)$ represents defective phosphorene with one divacancy (two removed P atoms) and one O atom.[115]

Therefore, when oxygen is present, the few-layer black phosphorus or phosphorene surface becomes oxidized, and the newly oxidized surface further reacts with ambient water to form phosphoric acid. This greatly reduces the likelihood of side products, such as H_3PO_3 and PH_3.

3.2.3 Stability of Red Phosphorus

Briefly discussed in Chapter 1, red phosphorus is a semi-stable polymeric allotrope of phosphorus of five known types, whose stability lies between the highly reactive white and the most thermodynamically stable black allotrope, with black sharing many stability and reactivity traits with violet phosphorus (red phosphorus Type V).[1-2,5,7] While red phosphorus does not ignite upon contact with air at room temperature as with the white allotrope, red phosphorus has been known to slowly oxidize in damp, moist air at room temperature, forming orthophosphoric acid, H_3PO_4.[1,5] However, a relatively uncommon oxygen acid of phosphorus is also produced via the oxidation of red phosphorus: hypodiphosphoric acid:[5]

$$\frac{2}{n} P_n + 2\, O_2 + 2\, H_2O \rightarrow H_4P_2O_6 \tag{3.3}$$

where P_n is the polymer chain of red phosphorus of *n* number of atoms. Phosphine gas has also been noted as a product of red phosphorus oxidation in air.[116] It appears the relative stability of the red phosphorus allotrope, as well as side products such as hypodiphosphoric acid and PH_3, diminishes its oxidative yield into H_3PO_4 compared to that of BP.

In studies of the flame-retardant effects of boron compounds on red phosphorus-containing epoxy resins, Dogan and Unlu noted that the experimental char yields were higher than anticipated using calculations.[117] The team determined that rather than completely vaporizing, some amount of red phosphorus reacted with the B_2O_3 and stayed in the condensed phase, resulting in the formation of boron phosphate.[117] While red phosphorus was not explored in this work, future studies will be discussed concerning the formation of boron phosphate from RP.

3.2.4 Boron Phosphate

Boron phosphate (BPO_4) is a useful dehydration catalyst for organic synthesis reactions and an important phosphating agent, with research into the synthesis of BPO_4 dating back over a century.[118-121] The crystal structure of boron phosphate is analogous to the silica mineral high-cristobalite, also called β-cristobalite (see Figure 3.3), while other crystal structures have been created under high pressure conditions.[119-120,122] Boron phosphate of various phosphorus/boron ratios can be obtained.[123]

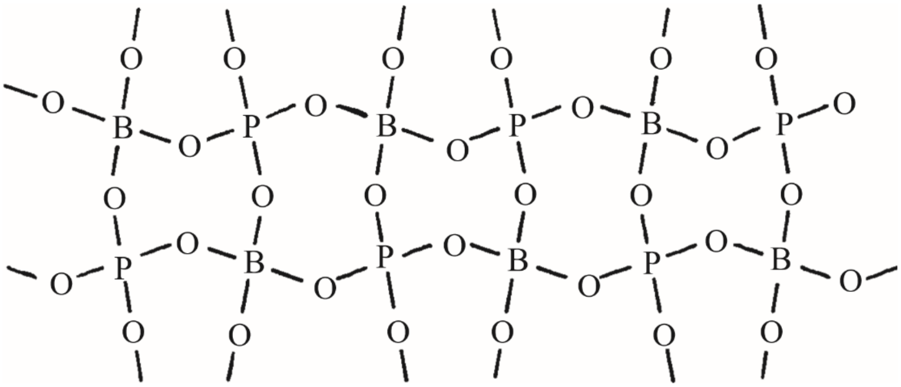

Figure 3.3 – Structure of boron phosphate.[120]

Several different synthetic routes have been taken to create BPO_4. In 1904, Mylius and Meusser were able to create boron phosphate with a relatively straightforward process using boric acid and phosphoric acid at high temperature.[121] However, in 1999, Kmecl and Bukovec determined that this reaction occurs at room temperature and depends on the diffusion rate of water:[119]

$$H_3PO_4 + H_3BO_3 \rightarrow BPO_4 + 3\ H_2O \tag{3.4}$$

Synthesis of BPO_4 involving boric acid and phosphoric acid created from the degradation of ammonium polyphosphate has also been reported.[124] Research conducted by Baykal et al in 2001 showed that boron phosphate can also be produced from the reactions of boron trioxide (B_2O_3) and diammonium hydrogen phosphate or phosphorus pentoxide (P_2O_5):[120]

$$B_2O_3 + 2\ (NH_4)_2HPO_4 \rightarrow 2\ BPO_4 + 4\ NH_3 + 3\ H_2O \tag{3.5a}$$

$$B_2O_3 + P_2O_5 \rightarrow 2\ BPO_4 \tag{3.5b}$$

Investigations into the flame-retardant behavior of bisphenol A bis(diphenyl phosphate) with zinc and other metal borates have yielded boron phosphate as a side product.[125-127] While other boron-based compounds have been used in the synthesis of BPO_4, such as the mineral borax ($Na_2B_4O_7 \cdot 10H_2O$),[120] research into the compound's development has slowed dramatically in the last few decades, with new research utilizing BPO_4 either sticking to applications or retreading previously determined synthetic routes with only slight variations on reactants (e.g., using tripropylborate versus triethylborate).[128-133]

3.3 Experimental Procedure

Boron trifluoride etherate (Acros, 48% BF_3) was obtained for use as a solvent in 2D black phosphorus liquid exfoliation (see Chapter 2). Several milliliters of hexanes (Fisher, HPLC Grade) were distilled with a distillation chip and 2 chips of sodium (Na) metal. The sodium metal will react with any water in the hexanes, leaving solid sodium hydroxide (NaOH) and unreacted sodium metal behind in the distillation. The dry hexanes were capped with a rubber septum and 2.0 mL were dry transferred under nitrogen gas to a vial containing a small crystal of BP that was previously evacuated. Approximately 0.25 mL of the boron trifluoride etherate was transferred to the dry hexanes under nitrogen. The reported density for the BF_3 etherate solution from the Fisher Scientific website (makers of the Acros product) is 1.1200 g/cm^3. This means that the 0.25 mL aliquot has a mass of 0.28 grams of $BF_3{\cdot}O(CH_2CH_3)_2$. 48% of this is 0.134 grams (pure BF_3), and using the molar mass (67.806 g/mol),[134] this is approximately 1.98 mmol of BF_3. Therefore, 1.98 mmol of BF_3 divided by 2.25 mL of combined solution (diethyl ether and dry hexanes) results in $[BF_3] = 0.88$ M. However, two separate colorless layers initially formed.

While the lone-pair electrons from the oxygen atom in the ether interact with the boron due to the empty p-orbital in boron, no method was implemented to directly remove the diethyl ether and purify BF_3. This is because of the equilibrium that exists between the boron trifluoride, diethyl ether, and the adduct:

$$BF_3 \cdot O(CH_2CH_3)_2 \rightleftharpoons BF_3 + (CH_3CH_2)_2O \tag{3.6}$$

The energy of this reaction is $\Delta E = +9.5$ kcal/mol with $\Delta G = 10.5$ kcal/mol.[135-136] Although these values indicate this reaction will not occur spontaneously, the hexanes and diethyl ether are miscible, and as some lone diethyl ether exists, the ether will mix with the hexanes, and the non-polar BF_3 molecule will dissolve into the non-polar hexanes. This will allow for the two separate layers to mix over time and allow for free BF_3 to interact with the black phosphorus. The equilibrium will shift to the right of Equation 3.6, creating additional free BF_3 and diethyl ether, allowing for interaction with black phosphorus. Like the black phosphorus crystals in exotic solvents (see Chapter 2), this vial sat undisturbed until a color change was observed.

3.4 Results and Discussion

The BF_3 in hexanes, still with an obvious second layer, turned from clear to a yellow color after five days. Seven days later (12 days after the experiment began), a deeper yellow color occurred, indicating that the reaction was persisting, and the product concentration was increasing. To test if this color was due to few-layer black phosphorus, several drops of the boron trifluoride-BP solution were placed on a glass slide. The specimen slide was placed in the vacuum oven to remove the hexanes/diethyl ether solvent and to remove smoke from the lab that formed from the sample upon contact with air.

After another day, the boron sample was removed from the vacuum oven. Upon closer inspection, the BF_3-treated black phosphorus (BF_3-BP) residue appeared white. The specimen plate was placed under the optical microscope and crystals were observed (see Figure 3.4).

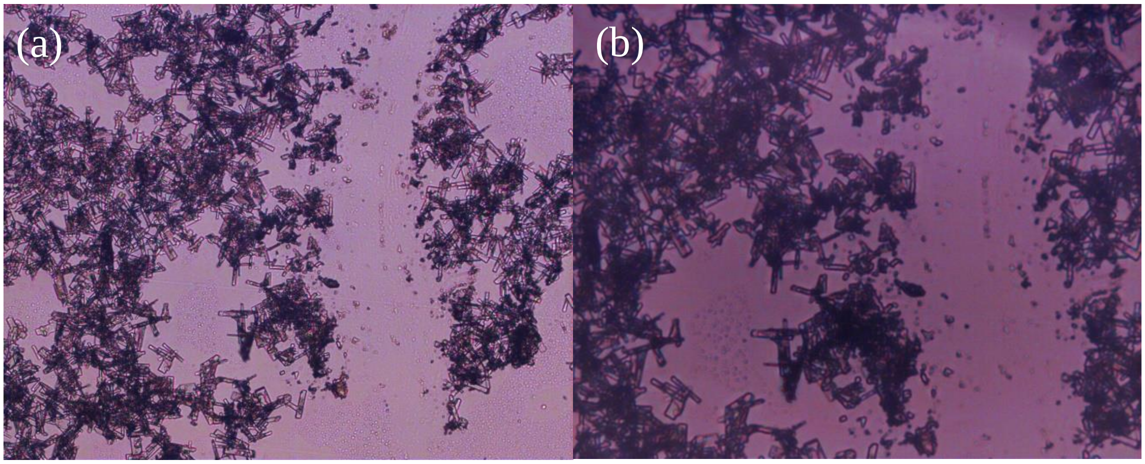

Figure 3.4 – Optical images of BF_3-BP solid at (a) 10x magnification and (b) 15x magnification.

An Si/SiO_2 substrate was cleaned by washing with acetone and sonicating. The substrate was mounted inside a Hitachi TM-1000 Scanning Electron Microscope (SEM) stage using conductive tape, and a couple of small pieces of the BF_3-BP residue were scraped onto it. Figure 3.5 shows some of these images. The substrate was removed from the SEM and transferred to a vial, however, the substrate was not held level for the duration and it is likely some of the flakes fell off. Additional images collected can be found in Appendix B.

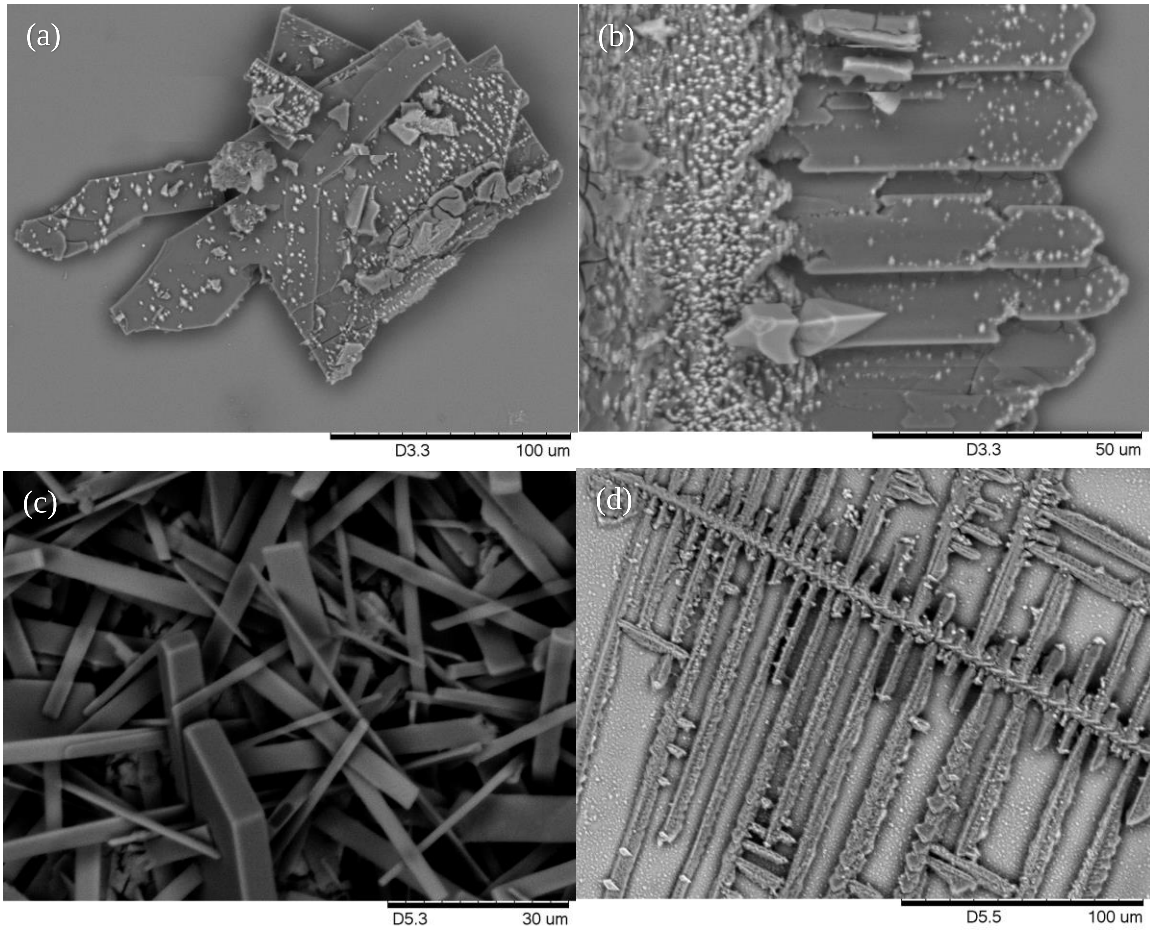

Figure 3.5 – SEM images of BF_3-BP solid at various magnifications.

Most of the images taken appear to be flakes (Figures 3.5a-b), wafers or rods (Figure 3.5c), and other solid products (Figure 3.5d). This confirms that not only has exfoliation occurred, but a chemical reaction has also taken place. To gain a better understanding as to what occurred, an ATR-IR spectrum was obtained from the white solid (see Figure 3.6). Infrared measurements were obtained with a Smiths IlluminatIR II Standard optical microscope attachment.

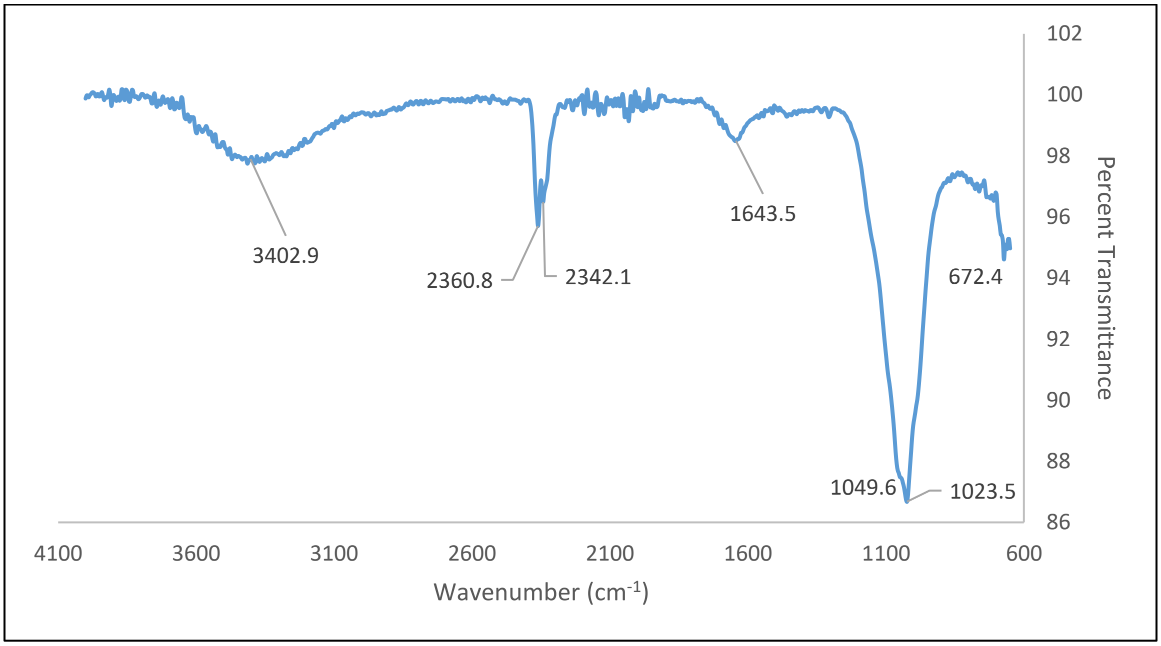

Figure 3.6 – ATR-IR spectrum of the unknown BF_3-BP solid.

The broad weak peak centered around 3403 cm^{-1} is characteristic of O-H stretching modes, most likely due to adsorbed water on the sample, although O-H bonds attached to P and B atoms cannot be ruled out.[119] The peak around 1643 cm^{-1} can also be explained by the deformation mode of adsorbed water.[119] The strong peak below 1100 cm^{-1} appears to be an amalgam of several different peaks, due to its many bulges and shoulders. Figure 3.7 shows an expansion of this region for better clarity.

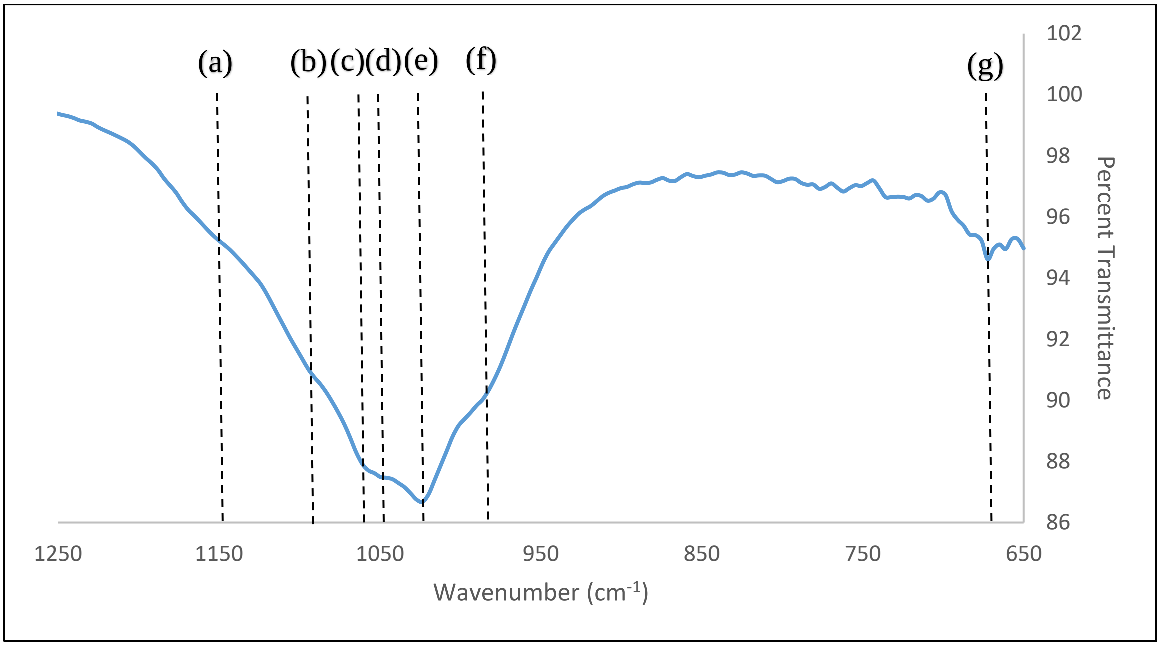

Figure 3.7 – ATR-IR spectrum of the unknown BF_3-BP solid, expanded. (a) 1150 cm^{-1}, (b) 1091 cm^{-1}, (c) 1053 cm^{-1}, (d) 1046 cm^{-1} (e) 1027 cm^{-1}, (f) 990 cm^{-1}, and (g) 672 cm^{-1}.

A potential peak or collection of peaks around 672 cm^{-1} correspond to bending vibrations of various borate segments, while the bands between 950-1150 cm^{-1} have characteristics of P-O stretches and B-O stretches for tetrahedrally-coordinated phosphorus and boron compounds, with these two stretching modes having very similar and almost equivalent frequencies, compiled in Table 3.1 below.[119,137-146]

Table 3.1 – Infrared Spectra Wavenumbers with Peak Assignments.[119,137-146]

Wavenumber (cm^{-1})	Peak Assignment
600-800	Bending vibrations of various borate segments
966-1082	Normal frequencies of isolated PO_4^{3-} ion
907-1014	Stretching vibrations of B-O bonds in $[BO_4]$ units
917-1200	B-O stretching vibrations of $[BO_4]$ tetrahedra
962-1100	Fundamental frequencies of the $[PO_4]$ group
1012-1022	Stretching vibration modes of $[BO_4]$ units
1150	$[BO_4]$ vibrations in hydrated boralites

The very weak band of sharp peaks between 1900-2300 cm^{-1} were not assigned to any known stretching or bending modes. In the study of borophosphate glasses, it was found that B-O-P bonds can slightly shift peaks in the IR spectrum, as well as broaden them, and the B:P ratio can vary.[147-148] However, the peaks centered around 2350 cm^{-1} do not seem to reflect known stretching or bending modes for B-O or P-O (see Figure 3.8).

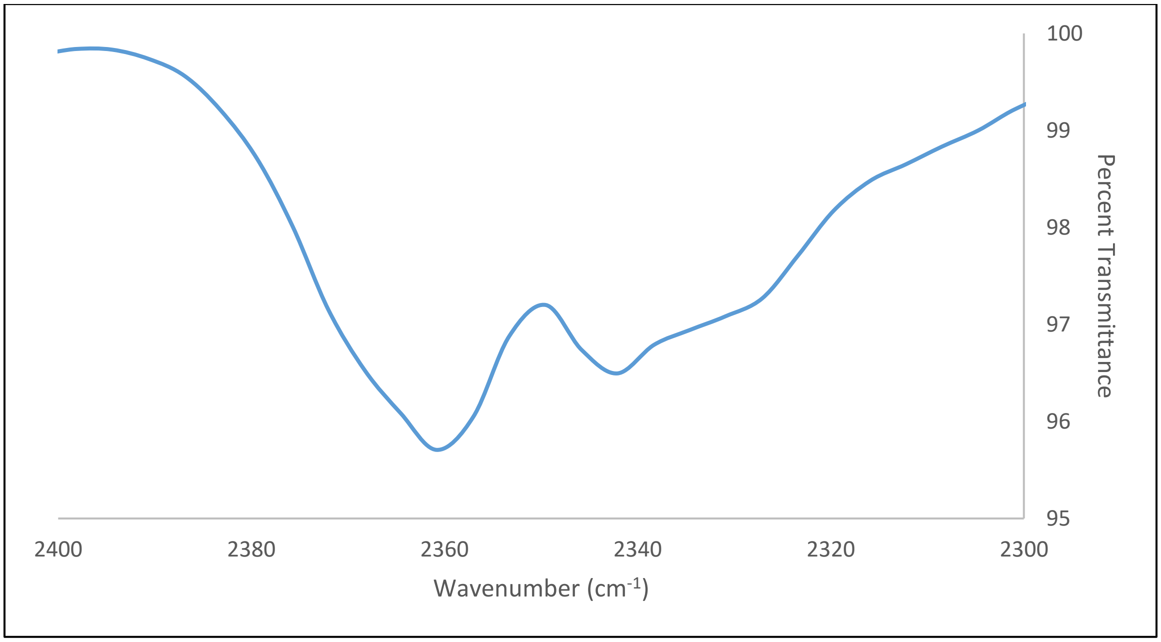

Figure 3.8 – ATR-IR spectrum of unknown BF_3-BP solid, expanded (2300-2400 cm^{-1}).

A stretching mode for P-OH is reported around 2361 cm^{-1}, which does line up perfectly with the obtained IR spectrum, however, the peak in the IR appears far sharper than is expected for the broader P-OH stretch, and the P-OH bending mode around 1731 cm^{-1} is missing from Figure 3.6.[149] While these peaks are not explicitly assigned, similar peaks exist in the spectrum for calcium phosphate from Granados-Correa et al, however they are missing from other calcium phosphate IR spectra.[143,150] Also, while similar peaks appear in some capacity for the IR spectra of BF_3 and H_3BO_3, other characteristic peaks for these two compounds are missing, indicating that the peaks in Figure 3.8 are not due to unreacted boron trifluoride or boric acid.[151-152] Although the SEM images taken of the solid in Figure 3.5 showed what appears to be black phosphorus flakes with only minor visible reaction product, the obtained IR spectrum does not clearly demonstrate that the majority of the product obtained is unreacted BP (see Figure 3.9). Also, the peaks centered around 2350 cm^{-1} do not appear to be indicative of bulk black phosphorus.

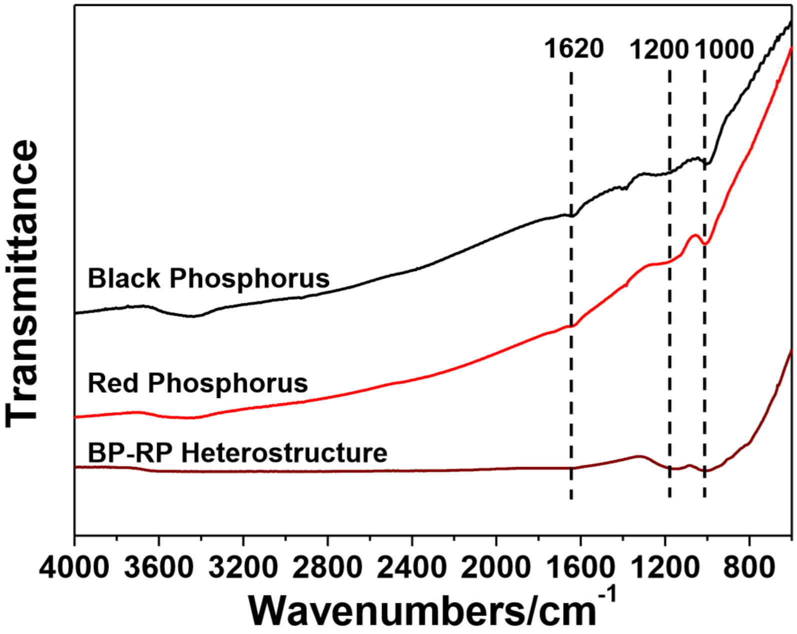

Figure 3.9 – Infrared spectra of black phosphorus, red phosphorus, and BP-RP heterostructure.[153]

The most probable explanation of these peaks comes from external carbon dioxide (CO_2), either ambient or adsorbed onto the surface of the solid. Carbon dioxide has a known IR-active asymmetric stretching mode between 2340-2360 cm^{-1}, as well as bending deformations around 667 cm^{-1}, which also fits the obtained spectrum in Figure 3.6.[109,154]

The peaks in the IR spectrum are significant in not just what is present, but also what is absent. While many characteristic phosphate and P-O stretches exist in the IR spectrum, a key mode that is not present is the strong P=O stretching mode for phosphoric acid, which appears between 1200-1410 cm^{-1}.[155-156] Also, P-O-P modes do not appear to be present between 700-820 cm^{-1}, as also noted by Baykal et al.[120,157-158] In the same range, B-O-B modes appear to be missing, although a broad shoulder in this region makes confirming these difficult.[148] There are also no bands around 1470 cm^{-1} and 790 cm^{-1}, which are indicative of boric acid, meaning no free acid exists in the sample.[119] Other B-O stretching modes for trigonal boron (BO_3 units) between 1200-1600 cm^{-1} are also absent.[137-139,142,159] IR-active peaks expected for B-F stretches from the tetrafluoroborate ion due to Equation 3.1b are also not seen in the spectrum, either because there is no tetrafluoroborate in the sample, the peaks are too weak to be visible, or they are hidden by other peaks of similar frequencies overlapping the bands.[160-161] Impurities from unreacted BF_3 etherate are not seen in the IR spectrum.[162]

Based on the IR spectrum analysis, the white solid material produced from the BF_3-treatment of bulk black phosphorus and air exposure is boron phosphate (BPO_4), which is further corroborated by independent IR studies of BPO_4.[119-120] Hi-res CI MS analysis performed on the material was inconclusive, which can be attributed to the low mass-to-charge ratio (m/z) of the phosphate (PO_4^{3-}) and boron (B^{3+}) species and the material's involatile nature, although a Knudsen Effusion Mass Spectrometry (KEMS) study has been done on BPO_4.[163] Exfoliation of black phosphorus of unknown flake thickness from bulk was successful using BF_3 etherate and hexanes, but upon contact with ambient water and oxygen, a reaction occurred to create boron phosphate under the proposed reaction scheme, following Equations 3.1b, 3.2, 3.4, 3.6, and Figure 3.2:

$$8\ BF_3 + P_{blk} + 12\ O_2 + 24\ H_2O \rightarrow 6\ H_3OBF_4 + 2\ H_3BO_3 + 4\ P_{div}(O) + 8\ H_3PO_4 \tag{3.7a}$$

$$6\ H_3OBF_4 + 2\ H_3BO_3 + 8\ H_3PO_4 \rightarrow 6\ H_3PO_4 + 2\ BPO_4 + 6\ H_2O + 6\ H_3OBF_4 \tag{3.7b}$$

$$6\ H_2O + 6\ H_3OBF_4 \rightarrow 12\ H_2O + 6\ HBF_4 \tag{3.7c}$$

$$12\ H_2O + 6\ HBF_4 \rightarrow 2\ HBF_4 + 4\ H_3BO_3 + 16\ HF \tag{3.7d}$$

$$6\ H_3PO_4 + 2\ BPO_4 + 4\ H_3BO_3 \rightarrow 2\ H_3PO_4 + 6\ BPO_4 + 12\ H_2O \tag{3.7e}$$

$$12\ H_2O + 2\ HBF_4 + 16\ HF \rightarrow 6\ H_2O + 2\ H_3BO_3 + 24\ HF \tag{3.7f}$$

$$2\ H_3PO_4 + 6\ BPO_4 + 6\ H_2O + 2\ H_3BO_3 \rightarrow 8\ BPO_4 + 12\ H_2O \tag{3.7g}$$

When Equations 3.7a-g are added together into a net equation, the overall reaction of BF_3 with black phosphorus, P_{blk}, in air is obtained:

$$8\ BF_3 + P_{blk} + 12\ O_2 + 12\ H_2O \rightarrow 8\ BPO_4 + 4\ P_{div}(O) + 24\ HF \tag{3.8}$$

As with Figure 3.2, the 4 P_{div}(O) in Equations 3.7a and 3.8 indicates four divacancies (8 overall P atoms removed from the P_{blk} flakes) with four O atoms bonded to the flakes. This chemical equation is the ideal scenario, with boron and phosphorus in a 1:1 ratio in anhydrous BPO_4, HF gas removed by the vacuum oven, and if black phosphorus is the limiting reagent, minute quantities of the P_{div}(O) remaining as phosphorus oxides. Again, it is hypothesized that this was possible \using the BF_3 in etherate liquid adduct by adding dry hexanes to the mixture for separation, as the adduct is safer and easier to handle than pure BF_3 gas.

3.5 Conclusion

Based on SEM images, analysis of the IR spectrum, and understanding of previously known chemical equations and reactions, the white solid material produced from the BF_3-treatment of bulk black phosphorus and air exposure is boron phosphate. Initial exfoliation of BP flakes from bulk material appears successful, with BPO_4 created after oxidation and reaction of the starting materials from solution. Infrared analysis confirms the presence of phosphate and tetra-coordinated boron species, with little evidence of boric acid, B_2O_3, phosphoric acid, or phosphorus oxides remaining.

3.6 Future Work

Exfoliation of black phosphorus using boron trifluoride can be proven by limiting the exposure to ambient conditions. Due to the Lewis acidity of BF_3, transfer of the BF_3-BP solution to a basic solution under an inert atmosphere (N_2, Ar, etc.) could remove any BF_3 attached to the BP flakes, allowing for isolation of few-layer black phosphorus, or even single-layer phosphorene. Exfoliation experiments should be investigated using other boron trihalides (BCl_3, BBr_3, BI_3) and other boron compounds (triphenylborane or tris(pentafluorophenyl)borane) by comparing steric interactions and Lewis acid strength to determine the best compound for phosphorene yield.

A ^{31}P-NMR and ^{11}B-NMR can be run as additional verification of the boron phosphate product, which has precedent in the literature.[124-127,164] Investigations into the formation of boron phosphate from red phosphorus can be undertaken to determine product yields of different allotropes and the various red phosphorus types. Characterization of the numerous solid structures noted by SEM can also be undertaken.

List of References

1. Corbridge, D. E. C., *Phosphorus: Chemistry, Biochemistry and Technology*. 6th ed.; CRC Press: Boca Raton, FL, 2013.

2. Bachhuber, F.; von Appen, J.; Dronskowski, R.; Schmidt, P.; Nilges, T.; Pfitzner, A.; Weihrich, R. The Extended Stability Range of Phosphorus Allotropes. *Angew. Chem., Int. Ed.* **2014,** *53* (43), 11629-11633.

3. Ruck, M.; Hoppe, D.; Wahl, B.; Simon, P.; Wang, Y.; Seifert, G. Fibrous Red Phosphorus. *Angew. Chem., Int. Ed.* **2005,** *44* (46), 7616-7619.

4. Smith, J. B.; Hagaman, D.; Ji, H.-F. Growth of 2D Black Phosphorus Film from Chemical Vapor Deposition. *Nanotechnology* **2016,** *27*, 215602.

5. Wiberg, N.; Holleman, A. F.; Wiberg, E., *Inorganic Chemistry*. 1st ed.; Academic Press: New York, 2001; pp 1028.

6. Böcker, S.; Häser, M. Covalent Structures of Phosphorus: A Comprehensive Theoretical Study. *Z. Anorg. Allg. Chem.* **1995,** *621*, 258-286.

7. Roth, W. L.; DeWitt, T. W.; Smith, A. J. Polymorphism of Red Phosphorus. *J. Am. Chem. Soc.* **1947,** *69* (11), 2881-2885.

8. Shen, Z.; Hu, Z.; Wang, W.; Lee, S.-F.; Chan, D. K. L.; Li, Y.; Gu, T.; Yu, J. C. Crystalline Phosphorus Fibers: Controllable Synthesis and Visible-Light-Driven Photocatalytic Activity. *Nanoscale* **2014,** *6*, 14163-14167.

9. Winchester, R. A. L.; Whitby, M.; Shaffer, M. S. P. Synthesis of Pure Phosphorus Nanostructures. *Angew. Chem., Int. Ed.* **2009,** *48*, 3616-3621.

10. Warschauer, D. Electrical and Optical Properties of Crystalline Black Phosphorus. *J. Appl. Phys.* **1963,** *34* (7), 1853-1860.

11. Asahina, H.; Morita, A. Band Structure and Optical Properties of Black Phosphorus. *J. Phys. C: Solid State Phys.* **1984,** *17* (11), 1839-1852.

12. Dai, J.; Zeng, X. Bilayer Phosphorene: Effect of Stacking Order on Bandgap and Its Potential Applications in Thin-Film Solar Cells. *J. Phys. Chem. Lett.* **2014,** *5*, 1289-1293.

13. Tran, V.; Soklaski, R.; Liang, Y.; Yang, L. Layer-Controlled Band Gap and Anisotropic Excitons in Few-Layer Black Phosphorus. *Phys. Rev. B* **2014,** *89*, 1-6.

14. Zhang, G.; Huang, S.; Chaves, A.; Song, C.; Özçelik, V. O.; Low, T.; Yan, H. Infrared Fingerprints of Few-Layer Black Phosphorus. *Nat. Commun.* **2017,** *8*, 14071.

15. Liu, H.; Neal, A. T.; Zhu, Z.; Luo, Z.; Xu, X.; Tománek, D.; Ye, P. D. Phosphorene: An Unexplored 2D Semiconductor with a High Hole Mobility. *ACS Nano* **2014,** *8* (4), 4033-4041.

16. Li, D.; Jussila, H.; Karvonen, L.; Ye, G.; Lipsanen, H.; Chen, X.; Sun, Z. Polarization and Thickness Dependent Absorption Properties of Black Phosphorus: New Saturable Absorber for Ultrafast Pulse Generation. *Sci. Rep.* **2015,** *5*, 15899.

17. Hu, T.; Hashmi, A.; Hong, J. Geometry, Electronic Structures and Optical Properties of Phosphorus Nanotubes. *Nanotechnology* **2015,** *26* (41), 415702.

18. Zhu, Z.; Tománek, D. Semiconducting Layered Blue Phosphorus: A Computational Study. *Phys. Rev. Lett.* **2014,** *112*, 176802.

19. Toll, J. S. Causality and the Dispersion Relation: Logical Foundations. *Phys. Rev.* **1956,** *104* (6), 1760-1770.

20. Mohr, P. J.; Newell, D. B.; Taylor, B. N. CODATA Recommended Values of the Fundamental Physical Constants: 2014. *J. Phys. Chem. Ref. Data* **2016,** *45* (4), 043102.

21. Collins, R. W. Automatic Rotating Element Ellipsometers: Calibration, Operation, and Real-Time Applications. *Rev. Sci. Instrum.* **1990,** *61* (8), 2029-2062.

22. Peters, T.; Ivanov, S. S.; Englisch, D.; Rangelov, A. A.; Vitanov, N. V.; Halfmann, T. Variable Ultrabroadband and Narrowband Composite Polarization Retarders. *Appl. Opt.* **2012,** *51* (31), 7466-7474.

23. Mao, N.; Tang, J.; Xie, L.; Wu, J.; Han, B.; Lin, J.; Deng, S.; Ji, W.; Xu, H.; Liu, K.; Tong, L.; Zhang, J. Optical Anisotropy of Black Phosphorus in the Visible Regime. *J. Am. Chem. Soc.* **2016,** *138* (1), 300-305.

24. Wang, F.; Ng, W. K. H.; Yu, J. C.; Zhu, H.; Li, C.; Zhang, L.; Liu, Z.; Li, Q. Red Phosphorus: An Elemental Photocatalyst for Hydrogen Formation from Water. *Appl. Catal., B* **2012,** *111*, 409-414.

25. Lee, H. U.; Lee, S. C.; Won, J.; Son, B.-C.; Choi, S.; Kim, Y.; Park, S. Y.; Kim, H.-S.; Lee, Y.-C.; Lee, J. Stable Semiconductor Black Phosphorus (BP)@Titanium Dioxide (TiO_2) Hybrid Photocatalysts. *Sci. Rep.* **2015,** *5*, 8691.

26. Shen, Z.; Sun, S.; Wang, W.; Liu, J.; Liu, Z.; Yu, J. C. A Black-Red Phosphorus Heterostructure for Efficient Visible-Light-Driven Photocatalysis. *J. Mater. Chem. A* **2015,** *3* (7), 3285-3288.

27. Hu, Z.; Yuan, L.; Liu, Z.; Shen, Z.; Yu, J. C. An Elemental Phosphorus Photocatalyst with a Record High Hydrogen Evolution Efficiency. *Angew. Chem., Int. Ed.* **2016,** *55* (33), 9580-9585.

28. Hu, Z.; Shen, Z.; Yu, J. C. Phosphorus Containing Materials for Photocatalytic Hydrogen Evolution. *Green Chem.* **2017,** *19* (3), 588-613.

29. Shi, Z.; Dong, X.; Dang, H. Facile Fabrication of Novel Red Phosphorus-CdS Composite Photocatalysts for H_2 Evolution under Visible Light Irradiation. *Int. J. Hydrogen Energy* **2016,** *41* (14), 5908-5915.

30. Ye, R.; del Angel-Vicente, P.; Liu, Y.; Arellano-Jimenez, M. J.; Peng, Z.; Wang, T.; Li, Y.; Yakobson, B. I.; Wei, S.-H.; Yacaman, M. J.; Tour, J. M. High-Performance Hydrogen Evolution from $MoS_{2(1-x)}P_x$ Solid Solution. *Adv. Mater.* **2016,** *28* (7), 1427-1432.

31. Ansari, S. A.; Cho, M. H. Highly Visible Light Responsive, Narrow Band Gap TiO_2 Nanoparticles Modified by Elemental Red Phosphorus for Photocatalysis and Photoelectrochemical Applications. *Sci. Rep.* **2016,** *6*, 25405.

32. Garside, B. K.; Lim, T. K. Laser Mode Locking using Saturable Absorbers. *J. Appl. Phys.* **1973,** *44* (5), 2335-2342.

33. Sotor, J.; Sobon, G.; Macherzynski, W.; Paletko, P.; Abramski, K. M. Black Phosphorus - A New Saturable Absorber Material for Ultrashort Pulse Generation. *Appl. Phys. Lett.* **2015,** *107*, 051108.

34. Luo, Z. C.; Liu, M.; Guo, Z. N.; Jiang, X. F.; Luo, A. P.; Zhao, C. J.; Yu, X. F.; Xu, W. C.; Zhang, H. Microfiber-based Few-Layer Black Phosphorus Saturable Absorber for Ultra-Fast Fiber Laser. *Opt. Express* **2015,** *23* (15), 20030-20039.

35. Lee, D.; Park, K.; Debnath, P. C.; Kim, I.; Song, Y.-W. Thermal Damage Supression of a Black Phosphorus Saturable Absorber for High-Power Operation of Pulsed Fiber Lasers. *Nanotechnology* **2016,** *27*, 365203.

36. Jiang, T.; Yin, K.; Zheng, X.; Yu, H.; Cheng, X.-A. Black Phosphorus as a New Broadband Saturable Absorber for Infrared Passively Q-Switched Fiber Lasers. 2015, arXiv:1504.07341 [physics.optics]. arXiv.org e-Print archive. https://arxiv.org/abs/1504.07341 (accessed Dec 23, 2016).

37. Qin, Z.; Xie, G.; Zhang, H.; Zhao, C.; Yuan, P.; Wen, S.; Qian, L. Black Phosphorus as a Saturable Absorber for the Q-Switched Er:ZBLAN Fiber Laser at 2.8 µm. *Opt. Express* **2016,** *23* (19), 24713-24718.

38. Kong, L.; Qin, Z.; Xie, G.; Guo, Z.; Zhang, H.; Yuan, P.; Qian, L. Multilayer Black Phosphorus as Broadband Saturable Absorber for Pulsed Lasers from 1 to 2.7 µm Wavelength. *Laser Phys. Lett.* **2016,** *13*, 045801.

39. Li, J.; Luo, H.; Zhai, B.; Lu, R.; Guo, Z.; Zhang, H.; Liu, Y. Black Phosphorus: A Two-Dimension Saturable Absorption Material for Mid-Infrared Q-Switched and Modelocked Fiber Lasers *Sci. Rep.* **2016,** *6*, 30361.

40. Fan, M.; Li, T.; Zhao, S.; Li, G.; Gao, X.; Yang, K.; Li, D.; Kränkel, C. Multilayer Black Phosphorus as Saturable Absorber for an Er:Lu_2O_3 Laser at ~3 μm *Photonics Res.* **2016,** *4* (5), 181-186.

41. Degnan, J. J. Optimization of Passively Q-Switched Lasers. *IEEE J. Quantum Electron.* **1995,** *31* (11), 1890-1901.

42. Sun, Z.; Martinez, A.; Wang, F. Optical Modulators with 2D Layered Materials. *Nat. Photonics* **2016,** *10*, 227-238.

43. Baba, M.; Takeda, Y.; Shibata, K.; Ikeda, T.; Morita, A. Optical Properties of Black Phosphorus and its Application to the Infrared Detector. *Jpn. J. Appl. Phys.* **1989,** *28* (11), 2104-2104.

44. Baba, M.; Nakamura, Y.; Shibata, K.; Morita, A. Photoconduction of Black Phosphorus in the Infrared Region. *Jpn. J. Appl. Phys.* **1991,** *30* (7A), 1178-1181.

45. Akahama, Y.; Kawamura, H. Optical and Electrical Studies on Band-Overlapped Metallization of the Narrow-Gap Semiconductor Black Phosphorus with Layered Structure. *Phys. Status Solidi B* **2001,** *223* (1), 349-353.

46. Yuan, H.; Liu, X.; Afshinmanesh, F.; Li, W.; Xu, G.; Sun, J.; Lian, B.; Curto, A. G.; Ye, G.; Hikita, Y.; Shen, Z.; Zhang, S.-C.; Chen, X.; Brongersma, M.; Hwang, H. Y.; Cui, Y. Polarization-Sensitive Broadband Photodetector using a Black Phosphorus Vertical p-n Junction. *Nat. Nanotechnol.* **2015,** *10*, 707-713.

47. Youngblood, N.; Chen, C.; Koester, S. J.; Li, M. Waveguide-Integrated Black Phosphorus Photodetector with High Responsivity and Low Dark Current. *Nat. Photonics* **2015,** *9*, 247-252.

48. Engel, M.; Steiner, M.; Avouris, P. Black Phosphorus Photodetector for Multispectral, High-Resolution Imaging. *Nano Lett.* **2014,** *14* (11), 6414-6417.

49. Penillard, A.; Tripon-Canseliet, C.; Rosticher, M.; Maksimovic, I.; Liu, Z.; Géron, E. Effective Photoconductivity of Exfoliated Black Phosphorus for Optoelectronic Switching under 1.55 μm Optical Excitation. *J. Appl. Phys.* **2016,** *119*, 024506.

50. Kroto, H. W.; Heath, J. R.; O'Brien, S. C.; Curl, R. F.; Smalley, R. E. C_{60}: Buckminsterfullerene. *Nature* **1985,** *318* (6042), 162-163.

51. Hassel, O.; Mark, H. Über die Kristallstruktur des Graphits. *Z. Phys.* **1924,** *25* (1), 317-337.

52. Bernal, J. D. The Structure of Graphite. *Proc. R. Soc. London, Ser. A* **1924,** *106* (740), 749-773.

53. Wallace, P. R. The Band Theory of Graphite. *Phys. Rev.* **1947,** *71* (9), 622-634.

54. Novoselov, K. S.; Geim, A. K.; Morozov, S. V.; Jiang, D.; Zhang, Y.; Dubonos, S. V.; Grigorieva, I. V.; Firsov, A. A. Electric Field Effect in Atomically Thin Carbon Films. *Science* **2004,** *306* (5696), 666-669.

55. Castellanos-Gomez, A.; Buscema, M.; Molenaar, R.; Singh, V.; Janssen, L.; Zant, H. S. J. v. d.; Steele, G. A. Deterministic Transfer of Two-Dimensional Materials by All-Dry Viscoelastic Stamping. *2D Mater.* **2014,** *1* (1), 011002.

56. Dean, C. R.; Young, A. F.; Meric, I.; Lee, C.; Wang, L.; Sorgenfrei, S.; Watanabe, K.; Taniguchi, T.; Kim, P.; Shepard, K. L.; Hone, J. Boron Nitride Substrates for High-Quality Graphene Electronics. *Nat. Nanotechnol.* **2010,** *5*, 722-726.

57. Moriya, R.; Yamaguchi, T.; Inoue, Y.; Morikawa, S.; Sata, Y.; Masubuchi, S.; Machida, T. Large Current Modulation in Exfoliated-Graphene/MoS_2/Metal Vertical Heterostructures. *Appl. Phys. Lett.* **2014,** *105* (8), 083119.

58. Bischoff, D.; Eich, M.; Varlet, A.; Simonet, P.; Overweg, H. C.; Ensslin, K.; Ihn, T. Graphene Nano-Heterostructures for Quantum Devices. *Mater. Today (Oxford, U. K.)* **2016,** *19* (7), 375-381.

59. Joensen, P.; Frindt, R. F.; Morrison, S. R. Single-layer MoS_2. *Mater. Res. Bull.* **1986,** *21* (4), 457-461.

60. Nicolosi, V.; Chhowalla, M.; Kanatzidis, M. G.; Strano, M. S.; Coleman, J. N. Liquid Exfoliation of Layered Materials. *Science* **2013,** *340* (6139), 1226419.

61. Hernandez, Y.; Nicolosi, V.; Lotya, M.; Blighe, F. M.; Sun, Z.; De, S.; McGovern, I. T.; Holland, B.; Byrne, M.; Gun'Ko, Y. K.; Boland, J. J.; Niraj, P.; Duesberg, G.; Krishnamurthy, S.; Goodhue, R.; Hutchison, J.; Scardaci, V.; Ferrari, A. C.; Coleman, J. N. High-Yield Production of Graphene by Liquid-Phase Exfoliation of Graphite. *Nat. Nanotechnol.* **2008,** *3* (9), 563-568.

62. Coleman, J. N. Liquid Exfoliation of Defect-Free Graphene. *Acc. Chem. Res.* **2013,** *46* (1), 14-22.

63. Brent, J. R.; Savjani, N.; Lewis, E. A.; Haigh, S. J.; Lewis, D. J.; O'Brien, P. Production of Few-Layer Phosphorene by Liquid Exfoliation of Black Phosphorus. *Chem. Commun. (Cambridge, U. K.)* **2014,** *50* (87), 13338-13341.

64. Golub, A. S.; Zubavichus, Y. V.; Slovokhotov, Y. L.; Novikov, Y. N. Single-Layer Dispersions of Transition Metal Dichalcogenides in the Synthesis of Intercalation Compounds. *Russ. Chem. Rev.* **2003,** *72* (2), 123-141.

65. Ma, R.; Sasaki, T. Nanosheets of Oxides and Hydroxides: Ultimate 2D Charge-Bearing Functional Crystallites. *Adv. Mater.* **2010,** *22* (45), 5082-5104.

66. Kang, J.; Wells, S. A.; Wood, J. D.; Lee, J.-H.; Liu, X.; Ryder, C. R.; Zhu, J.; Guest, J. R.; Husko, C. A.; Hersam, M. C. Stable Aqueous Dispersions of Optically and Electronically Active Phosphorene. *Proc. Natl. Acad. Sci. U.S.A.* **2016,** *113* (42), 11688-11693.

67. Guo, Z.; Zhang, H.; Lu, S.; Wang, Z.; Tang, S.; Shao, J.; Sun, Z.; Xie, H.; Wang, H.; Yu, X.-F.; Chu, P. K. From Black Phosphorus to Phosphorene: Basic Solvent Exfoliation, Evolution of Raman Scattering, and Applications to Ultrafast Photonics. *Adv. Funct. Mater.* **2015,** *25*, 6996-7002.

68. Xu, J.; Dang, D. K.; Tran, V. T.; Liu, X.; Chung, J. S.; Hur, S. H.; Choi, W. M.; Kim, E. J.; Kohl, P. A. Liquid-Phase Exfoliation of Graphene in Organic Solvents with Addition of Naphthalene. *J. Colloid Interface Sci.* **2014,** *418*, 37-42.

69. Woomer, A. H.; Farnsworth, T. W.; Hu, J.; Wells, R. A.; Donley, C. L.; Warren, S. C. Phosphorene: Synthesis, Scale-Up, and Quantitative Optical Spectroscopy. *ACS Nano* **2015,** *9* (9), 8869-8884.

70. Dhanabalan, S. C.; Ponraj, J. S.; Guo, Z.; Li, S.; Bao, Q.; Zhang, H. Emerging Trends in Phosphorene Fabrication towards Next Generation Devices. *Adv. Sci. (Weinheim, Ger.)* **2017,** *4*, 160035.

71. Suslick, K. S.; Hammerton, D. A.; Cline, R. E. Sonochemical Hot Spot. *J. Am. Chem. Soc.* **1986,** *108* (18), 5641-5642.

72. Tao, H.; Zhang, Y.; Gao, Y.; Sun, Z.; Yan, C.; Texter, J. Scalable Exfoliation and Dispersion of Two-Dimensional Materials - An Update. *Phys. Chem. Chem. Phys.* **2017,** *19* (2), 921-960.

73. Muscuso, L.; Cravanzola, S.; Cesano, F.; Scarano, D.; Zecchina, A. Optical, Vibrational, and Structural Properties of MoS_2 Nanoparticles Obtained by Exfoliation and Fragmentation via Ultrasound Cavitation in Isopropyl Alcohol. *J. Phys. Chem. C* **2015,** *119* (7), 3791-3801.

74. Ploss, R. S., Jr. Material Trivial Transfer Graphene. US 20130248097 A1, September 26, 2013.

75. Storhoff, J. J.; Elghanian, R.; Mucic, R. C.; Mirkin, C. A.; Letsinger, R. L. One-Pot Colorimetric Differentiation of Polynucleotides with Single Base Imperfections Using Gold Nanoparticle Probes. *J. Am. Chem. Soc.* **1998,** *120* (9), 1959-1964.

76. Abbott, A. P.; Barron, J. C.; Ryder, K. S.; Wilson, D. Eutectic-Based Ionic Liquids with Metal-Containing Anions and Cations. *Chem. - Eur. J.* **2007,** *13* (22), 6495-6501.

77. Abbott, A. P.; Capper, G.; Davies, D. L.; Rasheed, R. Ionic Liquids Based upon Metal Halide/Substituted Quaternary Ammonium Salt Mixtures. *Inorg. Chem.* **2004,** *43* (11), 3447-3452.

78. Abbott, A. P.; Al-Barzinjy, A. A.; Abbott, P. D.; Frisch, G.; Harris, R. C.; Hartley, J.; Ryder, K. S. Speciation, Physical and Electrolytic Properties of Eutectic Mixtures Based on $CrCl_3 \cdot 6H_2O$ and Urea. *Phys. Chem. Chem. Phys.* **2014,** *16* (19), 9047-9055.

79. Abbott, A. P.; Capper, G.; Davies, D. L.; Rasheed, R. K.; Tambyrajah, V. Novel Solvent Properties of Choline Chloride/Urea Mixtures. *Chem. Commun. (Cambridge, U. K.)* **2003,** *0* (1), 70-71.

80. Mukesh, C.; Mondal, D.; Sharma, M.; Prasad, K. Choline Chloride–Thiourea, a Deep Eutectic Solvent for the Production of Chitin Nanofibers. *Carbohydr. Polym.* **2014,** *103*, 466-471.

81. Hammond, O. S.; Bowron, D. T.; Edler, K. J. Liquid Structure of the Choline Chloride-Urea Deep Eutectic Solvent (Reline) from Neutron Diffraction and Atomistic Modelling. *Green Chem.* **2016,** *18* (9), 2736-2744.

82. Ng, A.; Sutto, T. E.; Matis, B. R.; Deng, Y.; Ye, P. D.; Stroud, R. M.; Brintlinger, T. H.; Bassim, N. D. Chemically Exfoliating Large Sheets of Phosphorene via Choline Chloride Urea Viscosity-Tuning. *Nanotechnology* **2017,** *28* (15), 155601.

83. Nilges, T.; Kersting, M.; Pfeifer, T. A Fast Low-Pressure Transport Route to Large Black Phosphorus Single Crystals. *J. Solid State Chem.* **2008,** *181* (8), 1707-1711.

84. Köpf, M.; Eckstein, N.; Pfister, D.; Grotz, C.; Krüger, I.; Greiwe, M.; Hansen, T.; Kohlmann, H.; Nilges, T. Access and In Situ Growth of Phosphorene-Precursor Black Phosphorus. *J. Cryst. Growth* **2014,** *405*, 6-10.

85. Ziletti, A.; Carvalho, A.; Campbell, D. K.; Coker, D. F.; Castro Neto, A. H. Oxygen Defects in Phosphorene. *Phys. Rev. Lett.* **2015,** *114* (4), 046801.

86. Edmonds, M. T.; Tadich, A.; Carvalho, A.; Ziletti, A.; O'Donnell, K. M.; Koenig, S. P.; Coker, D. F.; Özyilmaz, B.; Neto, A. H. C.; Fuhrer, M. S. Creating a Stable Oxide at the Surface of Black Phosphorus. *ACS Appl. Mater. Interfaces* **2015,** *7* (27), 14557-14562.

87. Makadia, V. S.; Manocha, L. M.; Manocha, S.; Gajera, H. L. The Freeze-Thaw Technique for Exfoliation of Graphite: A Novel Approach for Bulk Production of Scroll-Free Graphene Oxide Sheets. *Adv. Mater. Lett.* **2017,** *8* (3), 262-264.

88. Swatloski, R. P.; Visser, A. E.; Reichert, W. M.; Broker, G. A.; Farina, L. M.; Holbrey, J. D.; Rogers, R. D. Solvation of 1-Butyl-3-Methylimidazolium Hexafluorophosphate in Aqueous Ethanol-A Green Solution for Dissolving 'Hydrophobic' Ionic Liquids. *Chem. Commun. (Cambridge, U. K.)* **2001,** *0* (20), 2070-2071.

89. Silva, R. L. G. N. P.; Oliveira, A. F. d.; Neves, E. A. Spectrophotometric Determination of Iodate in Table Salt. *J. Braz. Chem. Soc.* **1998,** *9*, 171-174.

90. Li, N.; Shi, L.; Wang, X.; Guo, F.; Yan, C. Experimental Study of Closed System in the Chlorine Dioxide-Iodide-Sulfuric Acid Reaction by UV-Vis Spectrophotometric Method. *Int. J. Anal. Chem.* **2011,** *2011*, 1-7.

91. Bhagwat, A. D.; Sawant, S. S.; Ankamwar, B. G.; Mahajan, C. M. Synthesis of Nanostructured Tin Oxide (SnO_2) Powders and Thin Films by Sol-Gel Method. *J. Nano-Electron. Phys.* **2015,** *7* (4), 04037.

92. Hickling, G. G. Gravimetric Analysis: The Synthesis of Tin Iodide. *J. Chem. Educ.* **1990,** *67* (8), 702-703.

93. Goodman, J. F.; Gregg, S. J. 237. The Production of Active Solids by Thermal Decomposition. Part XI. The Heat Treatment of Precipitated Stannic Oxide. *J. Chem. Soc.* **1960,** *82* (0), 1162-1167.

94. Lee, M.; Roy, A. K.; Jo, S.; Choi, Y.; Chae, A.; Kim, B.; Park, S. Y.; In, I. Exfoliation of Black Phosphorus in Ionic Liquids. *Nanotechnology* **2017,** *28* (12), 125603.

95. Zhao, W.; Xue, Z.; Wang, J.; Jiang, J.; Zhao, X.; Mu, T. Large-Scale, Highly Efficient, and Green Liquid-Exfoliation of Black Phosphorus in Ionic Liquids. *ACS Appl. Mater. Interfaces* **2015,** *7*, 27608-27612.

96. Chaban, V. V.; Fileti, E. E.; Prezhdo, O. V. Imidazolium Ionic Liquid Mediates Black Phosphorus Exfoliation while Preventing Phosphorene Decomposition. *ACS Nano* **2017,** *11* (6), 6459-6466.

97. Ogino, I.; Yokoyama, Y.; Iwamura, S.; Mukai, S. R. Exfoliation of Graphite Oxide in Water without Sonication: Bridging Length Scales from Nanosheets to Macroscopic Materials. *Chem. Mater.* **2014,** *26*, 3334-3339.

98. Buchsteiner, A.; Lerf, A.; Pieper, J. Water Dynamics in Graphite Oxide Investigated with Neutron Scattering. *J. Phys. Chem. B* **2006,** *110* (45), 22328-22338.

99. Butler, I. B.; Schoonen, M. A. A.; Rickard, D. T. Removal of Dissolved Oxygen from Water: A Comparison of Four Common Techniques. *Talanta* **1994,** *41* (2), 211-215.

100. Sa, B.; Li, Y.-L.; Qi, J.; Ahuja, R.; Sun, Z. Strain Engineering for Phosphorene: The Potential Application as a Photocatalyst. *J. Phys. Chem. C* **2014,** *118* (46), 26560-26568.

101. Ma, H.; Shen, Z.; Yi, M.; Ben, S.; Liang, S.; Liu, L.; Zhang, Y.; Zhang, X.; Ma, S. Direct Exfoliation of Graphite in Water with Addition of Ammonia Solution. *J. Colloid Interface Sci.* **2017,** *503*, 68-75.

102. Summary of Properties of the Elements. In *CRC Handbook of Chemistry and Physics*, 98th ed.; Rumble, J. R., Ed.; CRC Press: Boca Raton, FL, 2018.

103. Properties of Ice and Supercooled Water. In *CRC Handbook of Chemistry and Physics*, 98th ed.; Rumble, J. R., Ed.; CRC Press: Boca Raton, FL, 2018.

104. Standard Density of Water. In *CRC Handbook of Chemistry and Physics*, 98th ed.; Rumble, J. R., Ed.; CRC Press: Boca Raton, FL, 2018.

105. Jensen, W. B. The Origin of the Name "Onion's Fusible Alloy". *J. Chem. Educ.* **2010,** *87* (10), 1050-1051.

106. Wood, B. New Fusible Alloys: Remarks on Determining the Melting Point of Metals. *J. Franklin Inst.* **1862,** *73* (1), 61-63.

107. Zeng, M.; Tan, L.; Wang, J.; Chen, L.; Rümmeli, M. H.; Fu, L. Liquid Metal: An Innovative Solution to Uniform Graphene Films. *Chem. Mater.* **2014,** *26* (12), 3637-3643.

108. Dupont, J.; Consorti, C. S.; Suarez, P. A. Z.; de Souza, R. F. Preparation of 1-Butyl-3-Methylimidazolium-Based Room Temperature Ionic Liquids. *Org. Synth.* **2002,** *79*, 236.

109. Housecroft, C. E.; Sharpe, A. G., *Inorganic Chemistry*. 2nd ed.; Pearson Education Limited: Harlow, 2005; pp 307.

110. Wamser, C. A. Hydrolysis of Fluoboric Acid in Aqueous Solution. *J. Am. Chem. Soc.* **1948,** *70* (3), 1209-1215.

111. Mikheeva, V. I.; Fedneva, E. M. Reaction Between the Ether Complex of Boron Trifluoride and Lithium Hydride Communication 1. Preparation of Pure Diborane. *Bull. Acad. Sci. USSR, Div. Chem. Sci. (Engl. Transl.)* **1956,** *5* (8), 925-934.

112. Gillespie, R. J.; Hartman, J. S. Nuclear Magnetic Resonance Studies of Ketone.BF_3 Complexes. II. The Boron Trifluoride Catalyzed Condensation of Acetone. *Can. J. Chem.* **1968,** *46*, 3799-3811.

113. Huang, Y.; Qiao, J.; He, K.; Bliznakov, S.; Sutter, E.; Chen, X.; Luo, D.; Meng, F.; Su, D.; Decker, J.; Ji, W.; Ruoff, R. S.; Sutter, P. Interaction of Black Phosphorus with Oxygen and Water. *Chem. Mater.* **2016,** *28* (22), 8330-8339.

114. Hanlon, D.; Backes, C.; Doherty, E.; Cucinotta, C. S.; Berner, N. C.; Boland, C.; Lee, K.; Harvey, A.; Lynch, P.; Gholamvand, Z.; Zhang, S.; Wang, K.; Moynihan, G.; Pokle, A.; Ramasse, Q. M.; McEvoy, N.; Blau, W. J.; Wang, J.; Abellan, G.; Hauke, F.; Hirsch, A.; Sanvito, S.; O'Regan, D. D.; Duesberg, G. S.; Nicolosi, V.; Coleman, J. N. Liquid Exfoliation of Solvent-Stabilized Few-Layer Black Phosphorus for Applications Beyond Electronics. *Nat. Commun.* **2015,** *6*, 8563.

115. Wang, G.; Slough, W. J.; Pandey, R.; Karna, S. P. Degradation of Phosphorene in Air: Understanding at Atomic Level. *2D Mater.* **2016,** *3* (2), 025011.

116. NRC. Red Phosphorus Smoke. In *Toxicity of Military Smokes and Obscurants: Volume 1* [Online]; National Academies Press: Washington, DC, 1997; Chapter 4, pp 98-126. http://www.nap.edu/catalog.php?record_id=5582.

117. Dogan, M.; Murat Unlu, S. Flame Retardant Effect of Boron Compounds on Red Phosphorus Containing Epoxy Resins. *Polym. Degrad. Stab.* **2014,** *99*, 12-17.

118. Moffat, J. B.; Goltz, H. L. Surface Chemistry and Catalytic Properties of Boron Phosphate: 1. Surface Area and Acidity. *Can. J. Chem.* **1965,** *43* (6), 1680-1688.

119. Kmecl, P.; Bukovec, P. Boron Phosphate: Its Synthesis, Gradual Crystallisation and Characterisation of Bulk Properties. *Acta. Chim. Slov.* **1999,** *46* (2), 161-171.

120. Baykal, A.; Kizilyalli, M.; Toprak, M.; Kniep, R. Hydrothermal and Microwave Synthesis of Boron Phosphate, BPO_4. *Turk. J. Chem.* **2001,** *25*, 425-432.

121. Mylius, F.; Meusser, A. Ueber die Bestimmung der Borsäure als Phosphat. *Ber. Dtsch. Chem. Ges.* **1904,** *37* (1), 397-401.

122. Mackenzie, J. D.; Roth, W. L.; Wentorf, R. H. New High Pressure Modifications of BPO_4 and $BAsO_4$. *Acta Crystallogr.* **1959,** *12* (1), 79.

123. Moffat, J. B.; Chao, E. E.; Nott, B. Temperature Programmed Desorption Studies on Boron Phosphate. *J. Colloid Interface Sci.* **1978,** *67* (2), 240-246.

124. Jimenez, M.; Duquesne, S.; Bourbigot, S. Intumescent Fire Protective Coating: Toward a Better Understanding of Their Mechanism of Action. *Thermochim. Acta* **2006,** *449* (1), 16-26.

125. Karrasch, A.; Wawrzyn, E.; Schartel, B.; Jäger, C. Solid-State NMR on Thermal and Fire Residues of Bisphenol A Polycarbonate/Silicone Acrylate Rubber/Bisphenol A bis(diphenyl-phosphate)/(PC/SiR/BDP) and PC/SiR/BDP/Zinc Borate (PC/SiR/BDP/ZnB) – Part I: PC Charring and the Impact of BDP and ZnB. *Polym. Degrad. Stab.* **2010,** *95* (12), 2525-2533.

126. Pawlowski, K. H.; Schartel, B.; Fichera, M. A.; Jäger, C. Flame Retardancy Mechanisms of Bisphenol A bis(diphenyl phosphate) in Combination with Zinc Borate in Bisphenol A Polycarbonate/Acrylonitrile–Butadiene–Styrene Blends. *Thermochim. Acta* **2010,** *498* (1), 92-99.

127. Wawrzyn, E.; Schartel, B.; Karrasch, A.; Jäger, C. Flame-Retarded Bisphenol A Polycarbonate/Silicon Rubber/Bisphenol A bis(diphenyl phosphate): Adding Inorganic Additives. *Polym. Degrad. Stab.* **2014,** *106*, 74-87.

128. Brei, V. V.; Kaspersky, V. A.; Gulyanitskaya, N. U. Synthesis and Study of Boron Phosphate and Titanium Silicate Compounds on Silica Surface. *React. Kinet. Catal. Lett.* **1993,** *50* (1-2), 415-421.

129. Liang, Y. F.; Zhu, X. L.; Jian, X. G. Synthesis and Properties of Sulfonated Poly(Phthalazinone Ether Nitrile Ketone)/Boron Phosphate Composite Membranes for PEMFC. *Solid State Ionics* **2008,** *179* (33), 1940-1945.

130. Magda, A.; Pode, R.; Muntean, C.; Medeleanu, M.; Popa, A. Synthesis and Characterization of Ammonium Phosphate Fertilizers with Boron. *J. Serb. Chem. Soc.* **2010,** *75* (7), 951-963.

131. Abat, M.; Degryse, F.; Baird, R.; McLaughlin, M. J. Formulation, Synthesis and Characterization of Boron Phosphate (BPO_4) Compounds as Raw Materials to Develop Slow-Release Boron Fertilizers. *J. Plant Nutr. Soil Sci.* **2014,** *177* (6), 860-868.

132. Şahin, A.; Ar, İ. Synthesis, Characterization and Fuel Cell Performance Tests of Boric Acid and Boron Phosphate Doped, Sulphonated and Phosphonated Poly(Vinyl Alcohol) Based Composite Membranes. *J. Power Sources* **2015,** *288*, 426-433.

133. Kilinc, M.; Cakal, G. O.; Bayram, G.; Eroglu, I.; Özkar, S. Flame Retardancy and Mechanical Properties of PET-Based Composites Containing Phosphorus and Boron-Based Additives. *J. Appl. Polym. Sci.* **2015,** *132* (22), 42016.

134. Physical Constants of Inorganic Compounds. In *CRC Handbook of Chemistry and Physics*, 98th ed.; Rumble, J. R., Ed.; CRC Press: Boca Raton, FL, 2018.

135. Pestunovich, A. E.; Doronina, E. P.; Albanov, A. I.; Voronkov, M. G. Reaction of Diphenyl[2-(triethoxysilyl)ethyl]phosphine Oxide with Boron Trifluoride Etherate. *Russ. J. Gen. Chem.* **2010,** *80* (10), 1913-1917.

136. Yuan, H.; Zheng, Y.; Zhang, J. Understanding the Mechanism of the Lewis Acid Promoted [3 + 2] Cycloaddition of Propargylic Alcohol and α-Oxo Ketene Dithioacetals. *J. Org. Chem.* **2016,** *81* (5), 1989-1997.

137. Weir, C. E.; Schroeder, R. A. Infrared Spectra of the Crystalline Inorganic Borates. *J. Res. Natl. Bur. Stand., Sect. A* **1964,** *68A* (5), 465-487.

138. Datka, J.; Piwowarska, Z. The Properties of Boralites Studied by Infrared Spectroscopy. *J. Chem. Soc., Faraday Trans. 1* **1989,** *85* (1), 47-53.

139. Peak, D.; Luther, G. W., III; Sparks, D. L. ATR-FTIR Spectroscopic Studies of Boric Acid Adsorption on Hydrous Ferric Oxide. *Geochim. Cosmochim. Acta* **2003,** *67* (14), 2551-2560.

140. El Mhammedi, M. A.; Bakasse, M.; Chtaini, A. Voltammetric Detection of Diquat at the Carbon Paste Electrode Containing a $Ca_{10}(PO_4)_6(OH)_2$. *Leonardo Electron. J. Pract. Technol.* **2007,** *10*, 1-12.

141. Gaafar, M. S.; Afifi, H. A.; Mekawy, M. M. Structural Studies of Some Phospho-Borate Glasses using Ultrasonic Pulse–Echo Technique, DSC and IR Spectroscopy. *Phys. B (Amsterdam, Neth.)* **2009,** *404* (12), 1668-1673.

142. Depci, T.; Ozbayoglu, G.; Yilmaz, A. Comparison of Different Synthesis Methods to Produce Lithium Triborate and Their Effects on Its Thermoluminescent Property. *Metall. Mater. Trans. A* **2010,** *41A*, 2584-2594.

143. Granados–Correa, F.; Bonifacio–Martínez, J.; Serrano–Gómez, J. Synthesis and Characterization of Calcium Phosphate and its Relation to Cr(VI) Adsorption. *Rev. Int. Contam. Ambiental* **2010,** *26* (2), 129-134.

144. Devamani, R. H. P.; Alagar, M. Synthesis and Characterization of Aluminium Phosphate Nanoparticles. *Int. J. Appl. Sci. Eng. Res.* **2012,** *1* (6), 769-775.

145. Erfani, M.; Saion, E.; Soltani, N.; Hashim, M.; Wan Abdullah, W. S. B.; Navasery, M. Facile Synthesis of Calcium Borate Nanoparticles and the Annealing Effect on Their Structure and Size. *Int. J. Mol. Sci.* **2012,** *13*, 14434-14445.

146. Chen, K.; Fang, L.; Zhang, T.; Jiang, S. P. New Zinc and Bismuth Doped Glass Sealants with Substantially Suppressed Boron Deposition and Poisoning for Solid Oxide Fuel Cells. *J. Mater. Chem. A* **2014,** *2* (Suppl. 1), 18655-18665.

147. Ouis, M. A.; El-Batal, H. A.; Azooz, M. A.; Abdelghany, A. M. Characterization of WO_3-doped Borophosphate Glasses by Optical, IR and ESR Spectroscopic Techniques Before and After Subjecting to Gamma Irradiation. *Indian J. Pure Appl. Phys.* **2013,** *51*, 11-17.

148. Hermansen, C.; Youngman, R. E.; Wang, J.; Yue, Y. Structural and Topological Aspects of Borophosphate Glasses and Their Relation to Physical Properties. *J. Chem. Phys.* **2015,** *142* (18), 184503.

149. Ge, S.; Zhang, L.; Wang, P.; Fang, Y. Intense, Stable and Excitation Wavelength-Independent Photoluminescence Emission in the Blue-Violet Region from Phosphorene Quantum Dots. *Sci. Rep.* **2016,** *6*, 27307.

150. Berzina-Cimdina, L.; Borodajenko, N. Research of Calcium Phosphates Using Fourier Transform Infrared Spectroscopy. In *Infrared Spectroscopy - Materials Science, Engineering and Technology* [Online]; Theophanides, T., Ed.; InTech: 2012; Chapter 2, pp 123-148. http://www.intechopen.com/books/infrared-spectroscopy-materials-science-engineering-andtechnology/research-of-calcium-phosphates-using-fourier-transformation-infrared-spectroscopy (accessed Nov 16, 2017).

151. Gage, D. M.; Barker, E. F. The Infra-Red Absorption Spectrum of Boron Trifluoride. *J. Chem. Phys.* **1939,** *7*, 455-459.

152. Bethell, D. E.; Sheppard, N. The Infra-Red Spectrum and Structure of Boric Acid. *Trans. Faraday Soc.* **1955,** *51,* 9-15.

153. Shen, Z.; Sun, S.; Wang, W.; Liu, J.; Liu, Z.; Yu, J. C. A Black-Red Phosphorus Heterostructure for Efficient Visible-Light-Driven Photocatalysis. *J. Mater. Chem. A* **2015,** *3* (Suppl. S4), 3285-3288.

154. Sanati, M.; Andersson, A. DRIFT Study of the Oxidation and the Ammoxidation of Toluene over a TiO_2 (B)-supported Vanadia Catalyst. *J. Mol. Catal.* **1993,** *81*, 51-62.

155. Mielke, Z.; Andrews, L. Infrared Spectra of P_4O_6, P_4O_7, P_4O_8, P_4O_9, and P_4O_{10} in Solid Argon. *J. Phys. Chem.* **1989,** *93*, 2971-2976.

156. Rudolph, W. W. Raman- and Infrared-Spectroscopic Investigations of Dilute Aqueous Phosphoric Acid Solutions. *Dalton Trans.* **2010,** *39* (40), 9642-9653.

157. Kniep, R.; Engelhardt, H.; Hauf, C. A First Approach to Borophosphate Structural Chemistry. *Chem. Mater.* **1998,** *10* (10), 2930-2934.

158. Ahsan, M. R.; Uddin, M. A.; Mortuza, M. G. Infrared Study of the Effect of P_2O_5 in the Structure of Lead Silicate Glasses. *Indian J. Pure Appl. Phys.* **2005,** *43,* 89-99.

159. Rada, S.; Culea, E.; Rada, M.; Maties, V.; Bosca, M.; Pop, L.; Fechete, R.; Chelcea, R.; Moldovan, D. Immobilization of Gadolinium in Borate-Tellurate Glasses. *J. Phys.: Conf. Ser.* **2009,** *182*, 012075.

160. Katsyuba, S. A.; Dyson, P. J.; Vandyukova, E. E.; Chernova, A. V.; Vidiš, A. Molecular Structure, Vibrational Spectra, and Hydrogen Bonding of the Ionic Liquid 1-Ethyl-3-methyl-1H-imidazolium Tetrafluoroborate. *Helv. Chim. Acta* **2004,** *87* (10), 2556-2565.

161. Heimer, N. E.; Del Sesto, R. E.; Meng, Z.; Wilkes, J. S.; Carper, W. R. Vibrational Spectra of Imidazolium Tetrafluoroborate Ionic Liquids. *J. Mol. Liq.* **2006,** *124*, 84-95.

162. Boron Trifluoride Diethyl Etherate. http://www.hanhonggroup.com/ir/ir_en/RB01030069.html (accessed Nov 18, 2017), Hanhong Group IR Spectrum.

163. Lopatin, S. I.; Semenov, G. A. A Mass Spectrometric Study of the Vaporization of Boron Phosphate (BPO_4). *Rapid Commun. Mass Spectrom.* **1999,** *13*, 1398-1400.

164. Koudelka, L.; Mošner, P.; Šubčík, J. Study of Structure and Properties of Modified Borophosphate Glasses. *IOP Conf. Ser.: Mater. Sci. Eng.* **2009,** *2* (1), 012015.

Appendix A: Abbreviations

AFM Atomic Force Microscopy

ATR Attenuated Total Reflectance

$[BMIM]PF_6$ 1-Butyl-3-methylimidazolium Hexafluorophosphate

BP Black Phosphorus

CCTU Choline Chloride Thiourea

CCU Choline Chloride Urea

CI Chemical Ionization

CVD Chemical Vapor Deposition

DES Deep Eutectic Solvent

Er:ZBLAN Erbium-doped ZrF_4-BaF_2-LaF_3-AlF_3-NaF

FET Field-Effect Transistor

GO Graphene Oxide

HWP Half-Wave Plate

IPA Isopropyl Alcohol

KEMS Knudsen Effusion Mass Spectrometry

MS Mass Spectrometry

NMP N-Methyl-2-Pyrrolidone

PMMA Poly(Methyl Methacrylate)

PNT Phosphorus Nanotube

QWP Quarter-Wave Plate

RP Red Phosphorus

SDS Sodium Dodecyl Sulfate

SEM Scanning Electron Microscopy

TMD Transition Metal Dichalcogenide

UV-Vis Ultraviolet-Visible

Appendix B: Additional Images of BPO_4

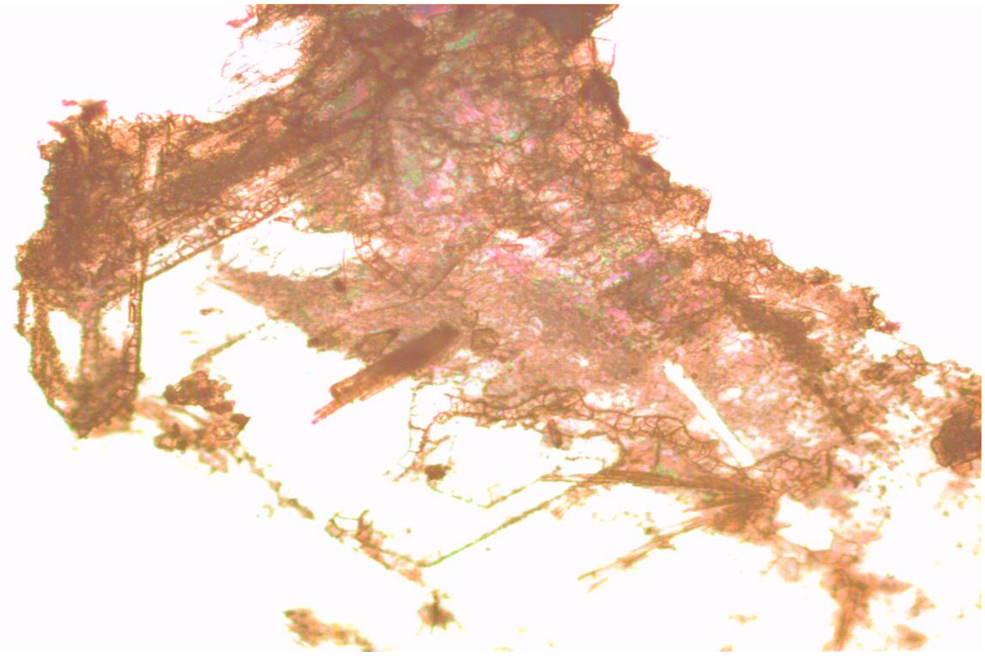

Figure B.1 – Optical image of BPO_4 product at 10x magnification with backlight.

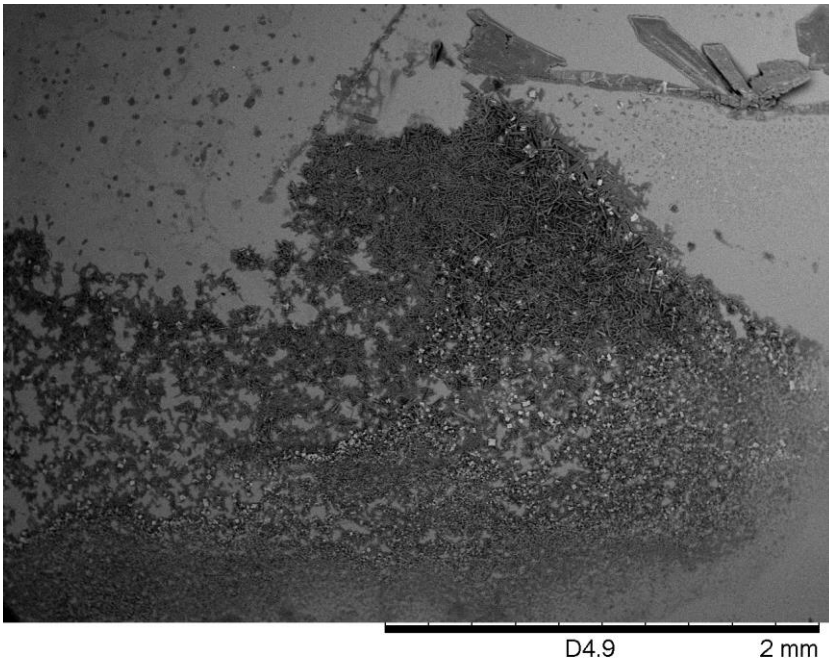

Figure B.2 – SEM image of BPO_4 product.

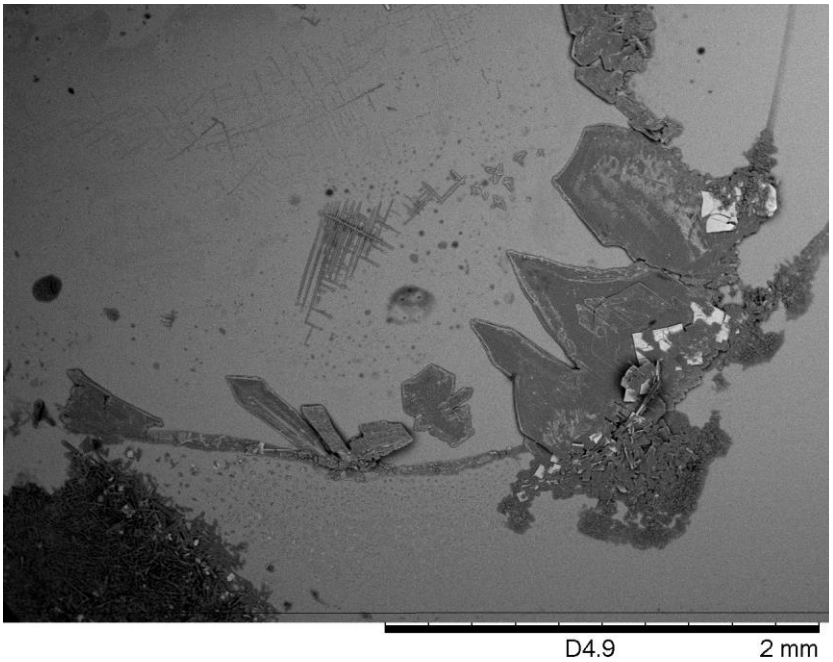

Figure B.3 – SEM image of BPO_4 product.

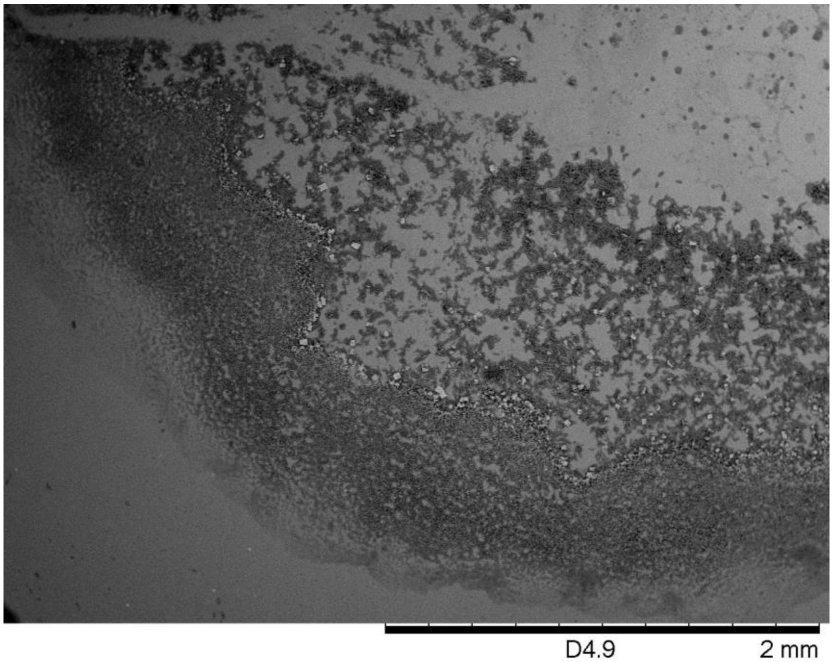

Figure B.4 – SEM image of BPO_4 product.

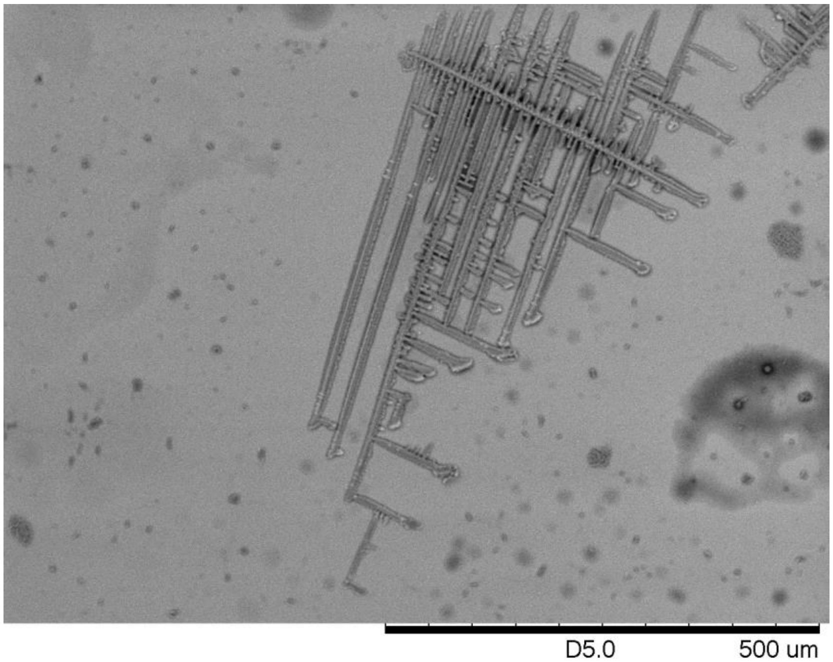

Figure B.5 – SEM image of BPO_4 product.

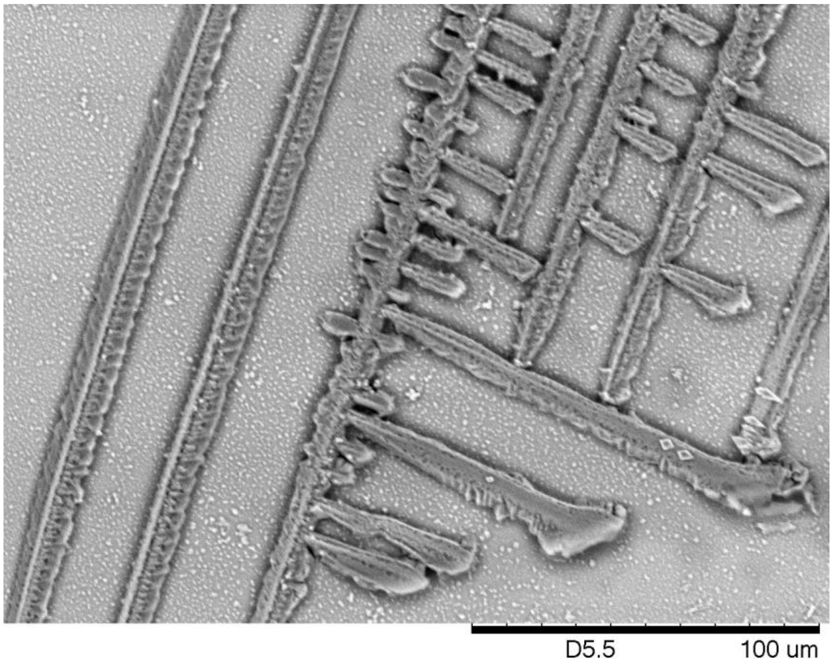

Figure B.6 – SEM image of BPO_4 product.

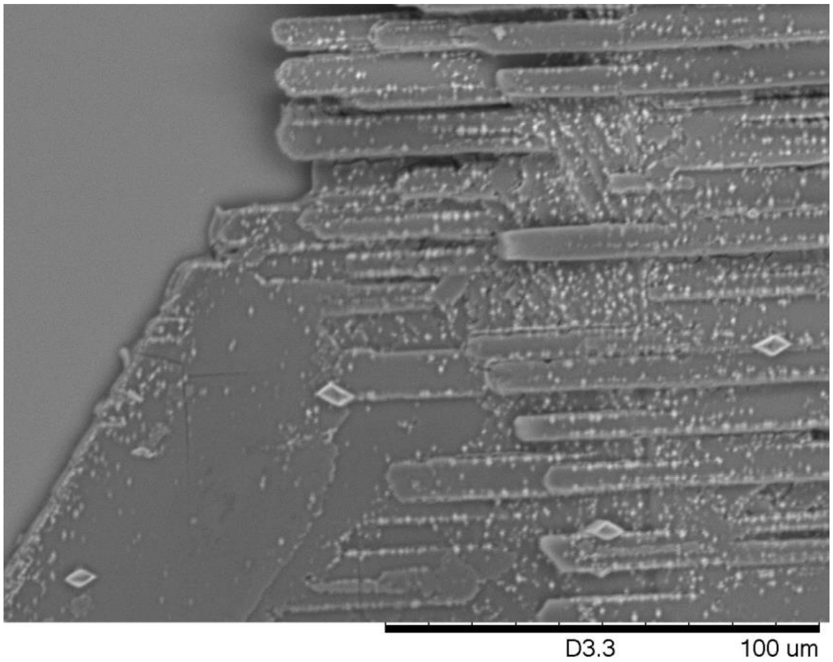

Figure B.7 – SEM image of BPO_4 product.

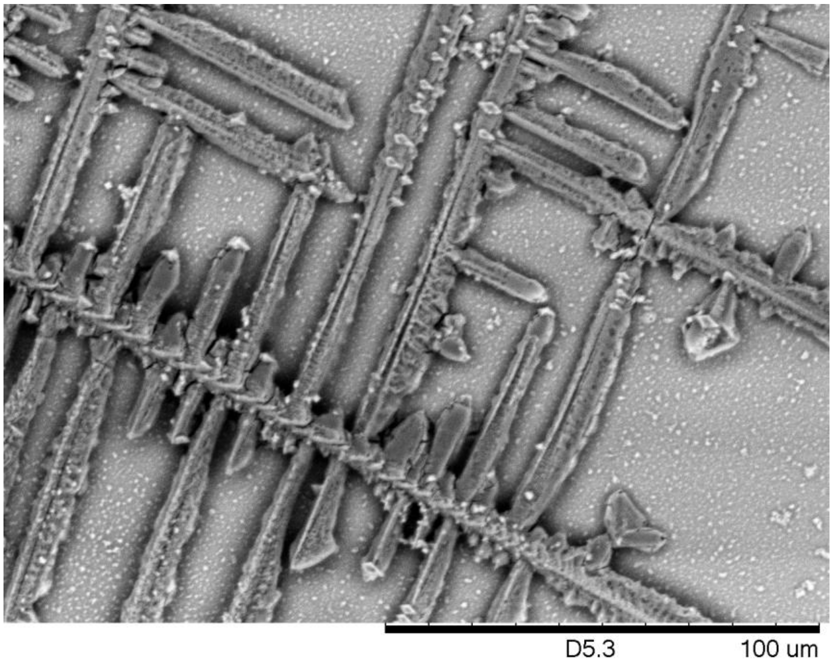

Figure B.8 – SEM image of BPO_4 product.

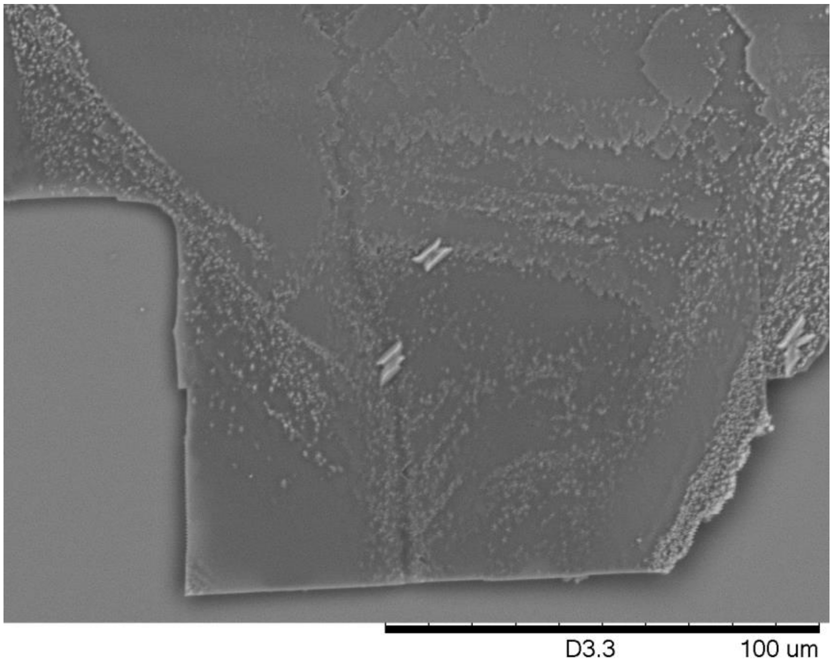

Figure B.9 – SEM image of BPO_4 product.

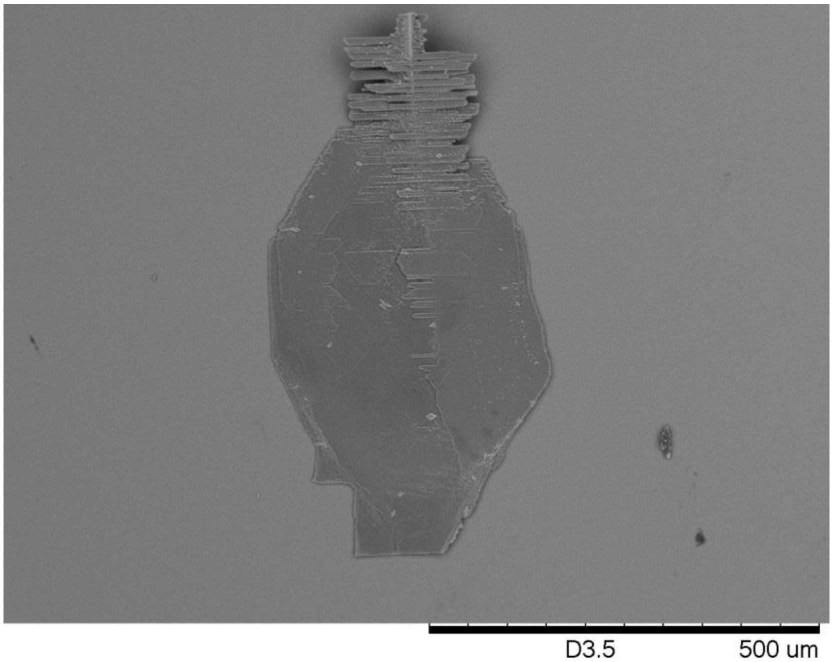

Figure B.10 – SEM image of BPO_4 product.

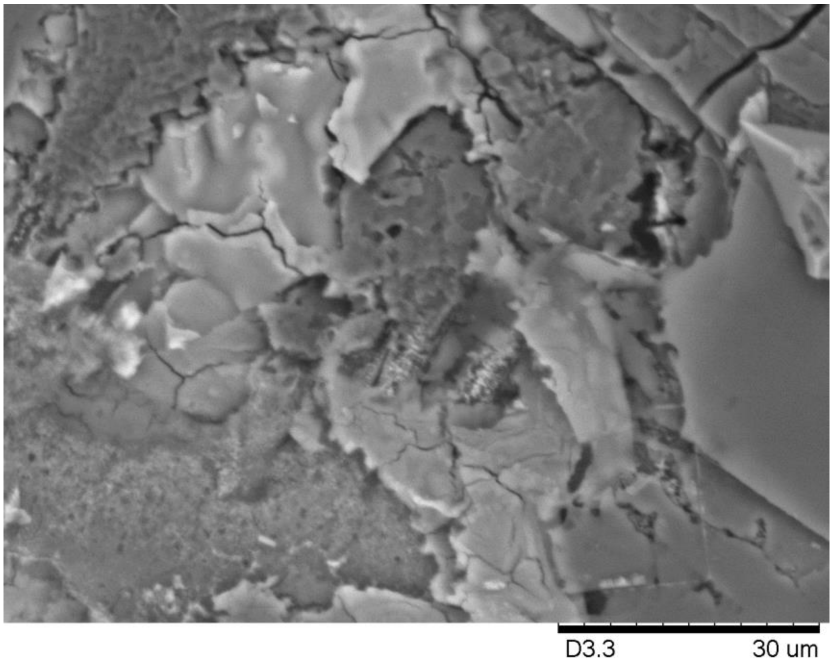

Figure B.11 – SEM image of BPO_4 product.

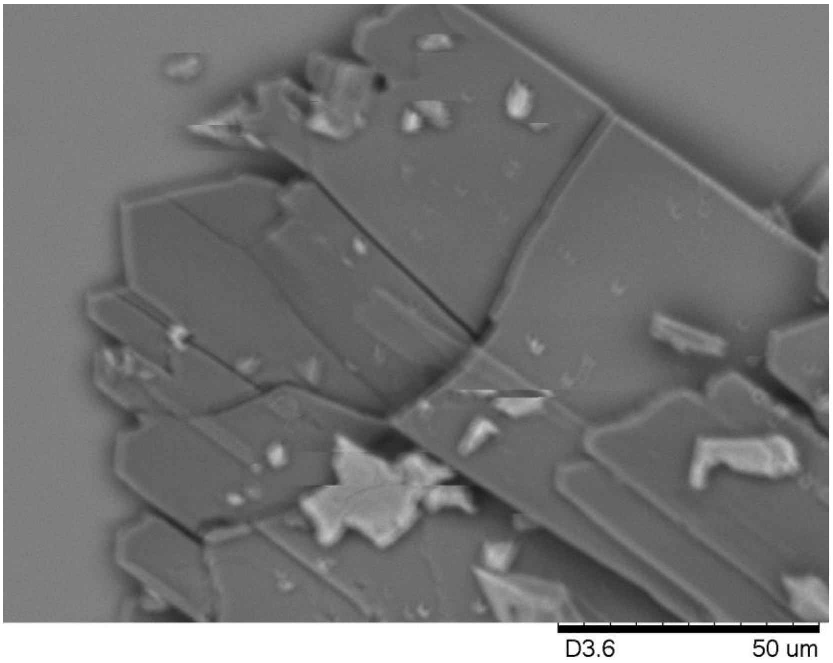

Figure B.12 – SEM image of BPO_4 product.

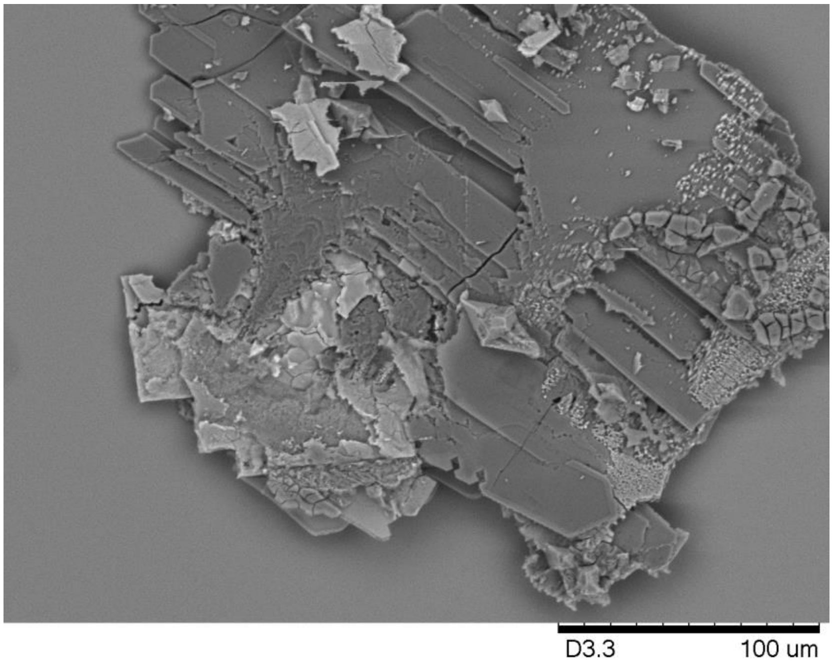

Figure B.13 – SEM image of BPO_4 product.

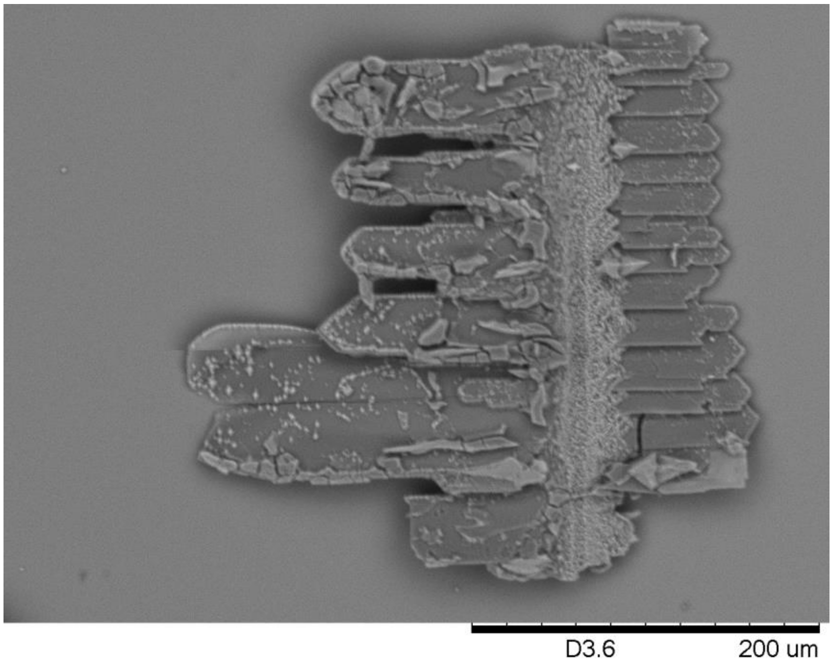

Figure B.14 – SEM image of BPO_4 product.

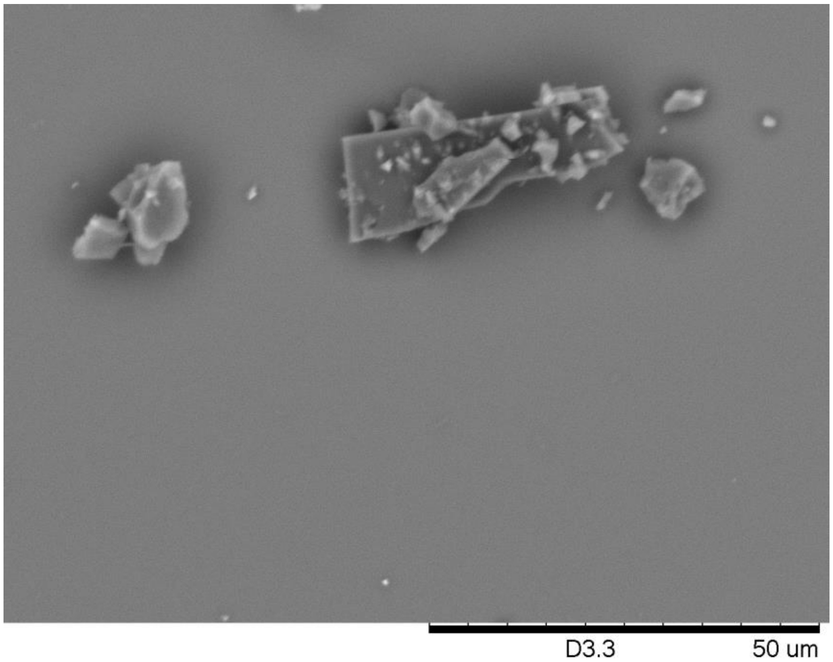

Figure B.15 – SEM image of BPO_4 product.

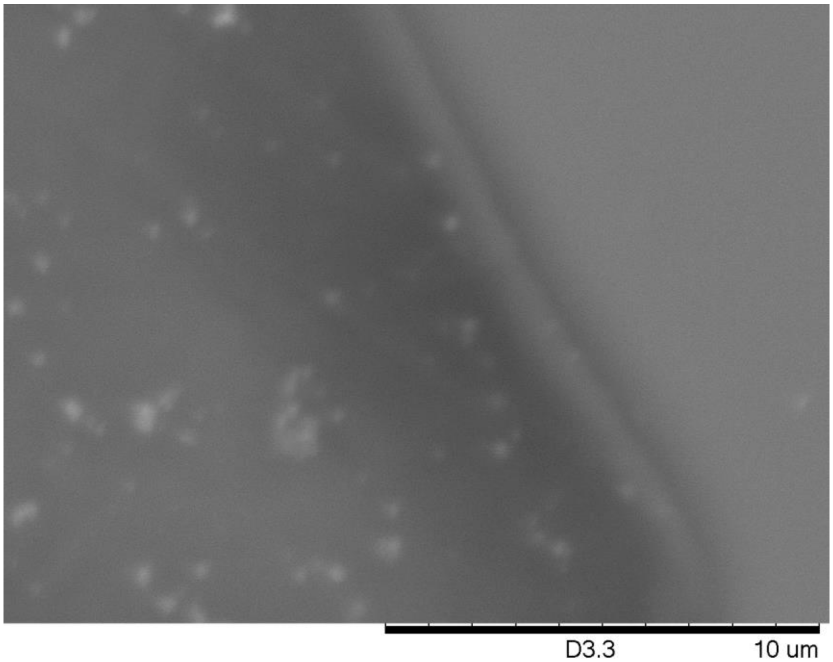

Figure B.16 – SEM image of BPO_4 product with thin edge.

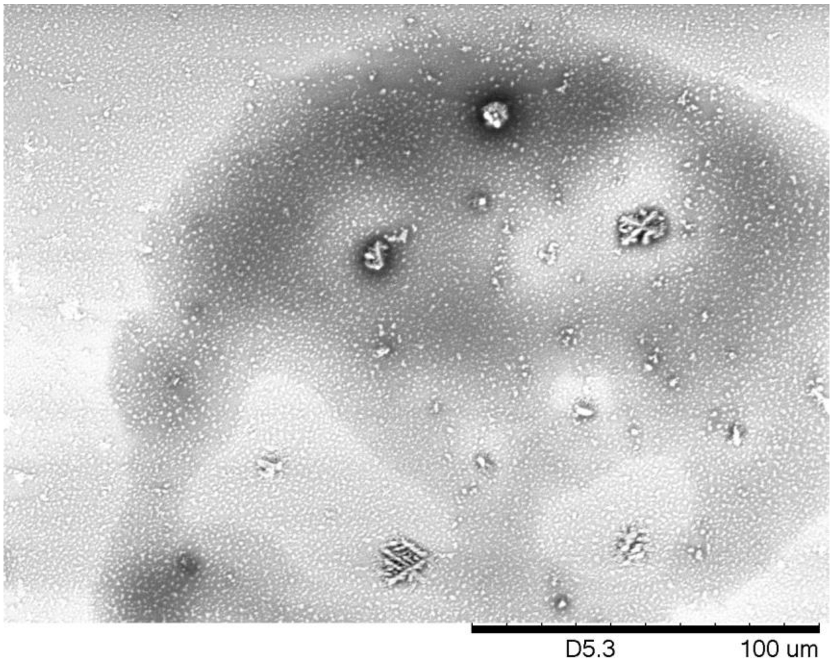

Figure B.17 – SEM image of small BPO_4 fragments with thin background.

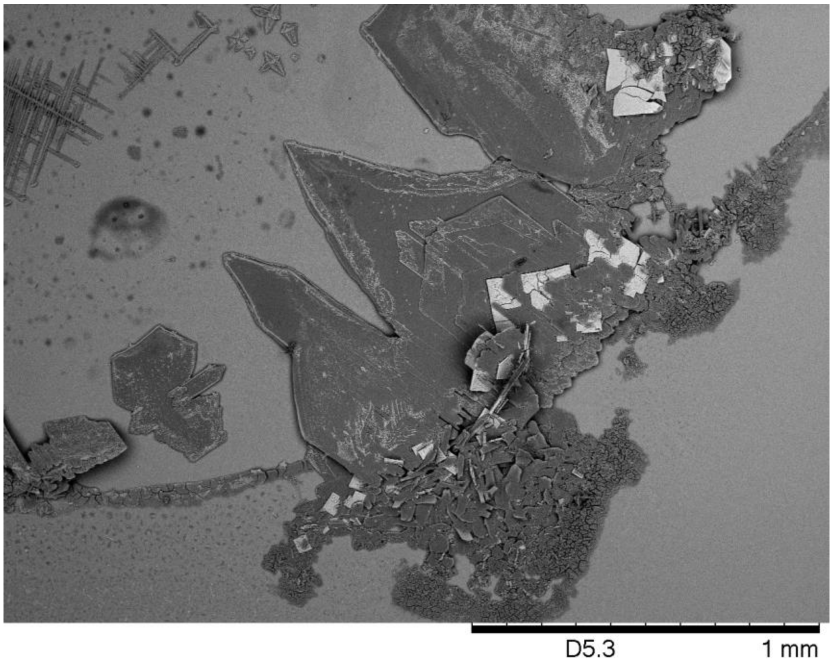

Figure B.18 – SEM image of BPO_4 product.

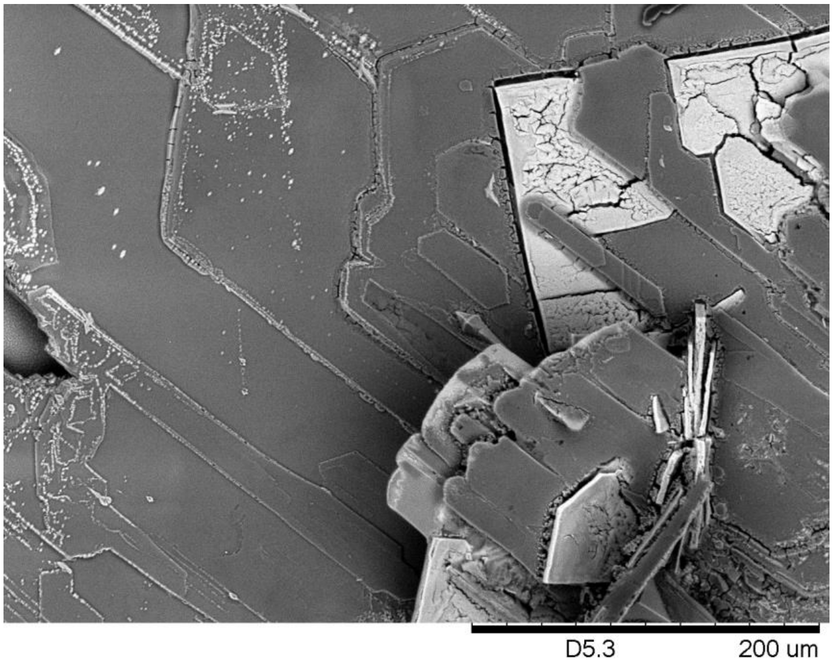

Figure B.19 – SEM image of BPO_4 product.

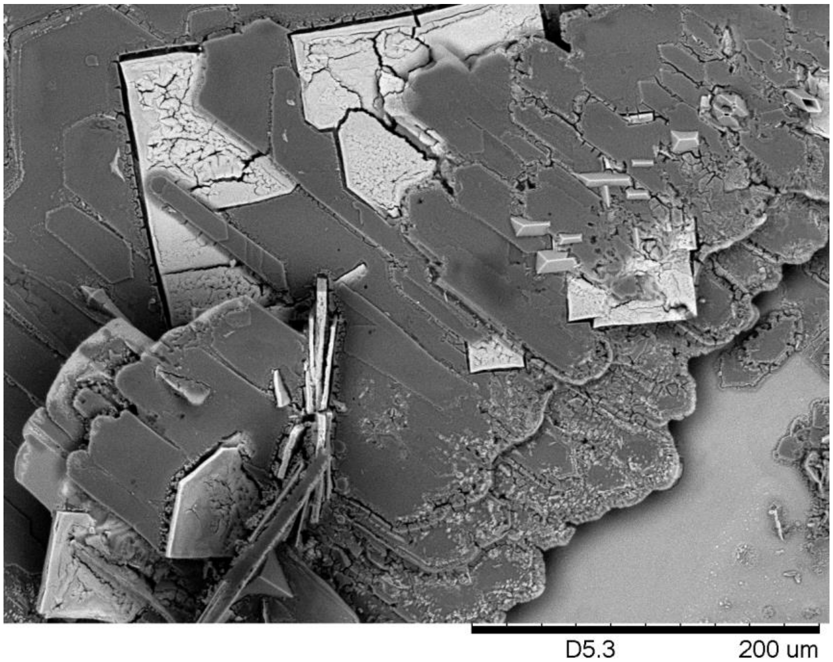

Figure B.20 – SEM image of BPO_4 product.

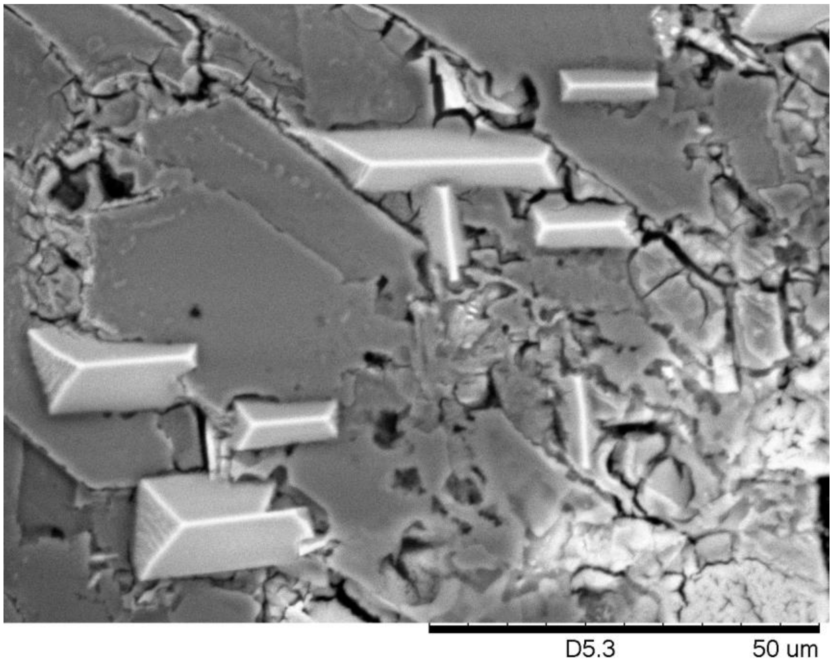

Figure B.21 – SEM image of BPO_4 product.

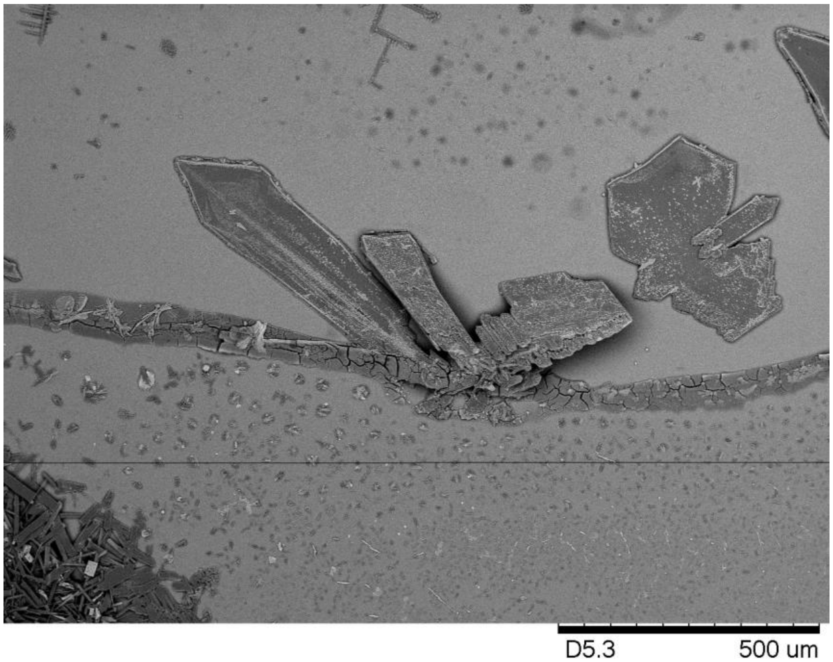

Figure B.22 – SEM image of BPO_4 product.

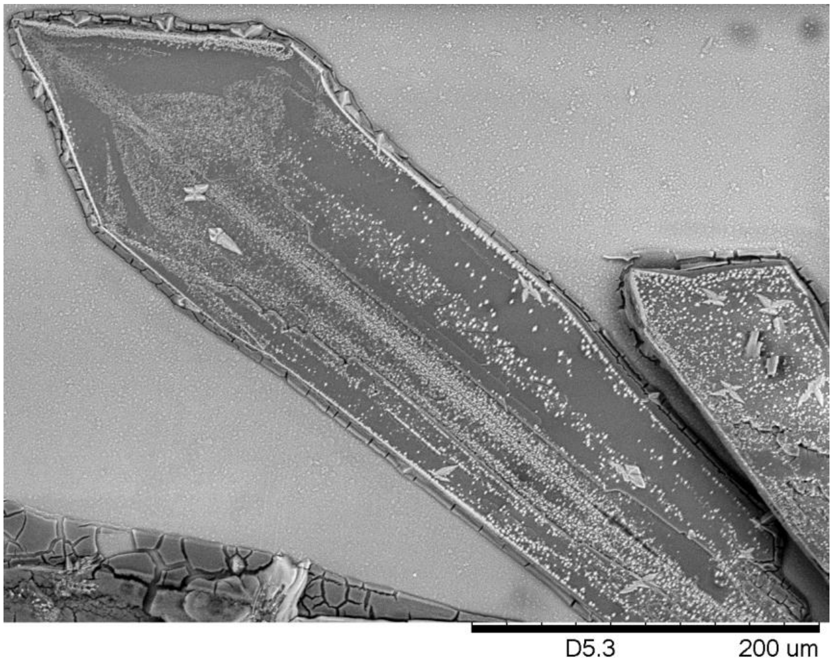

Figure B.23 – SEM image of BPO_4 product.

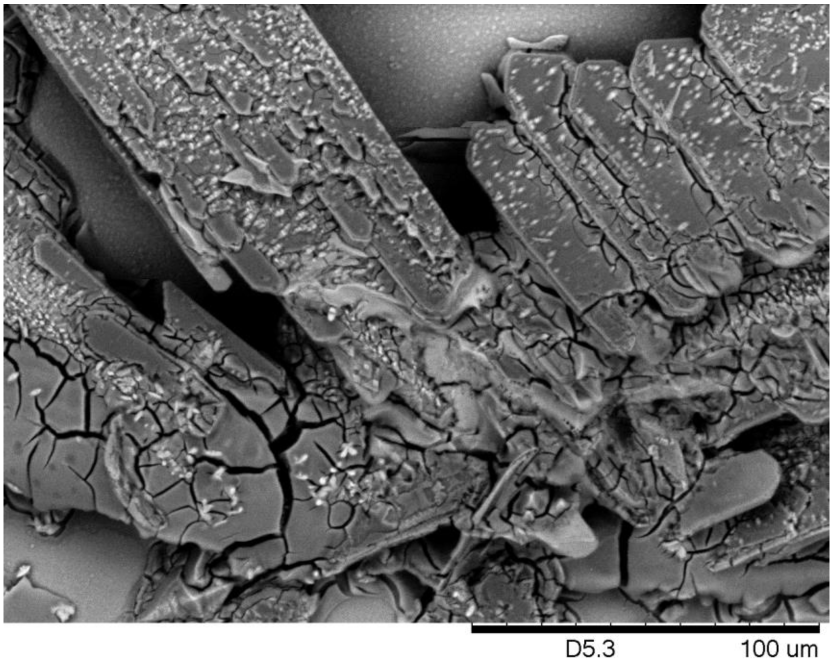

Figure B.24 – SEM image of BPO_4 product.

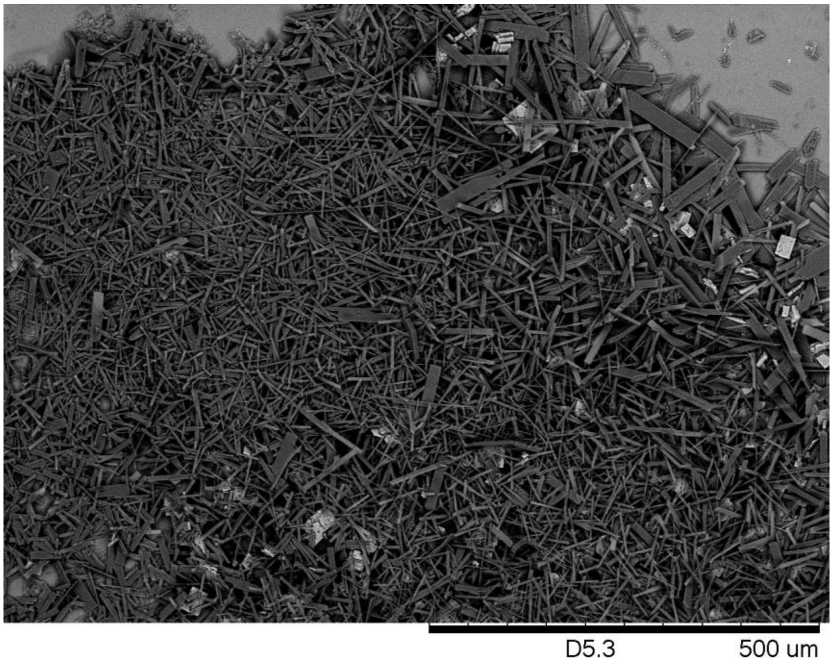

Figure B.25 – SEM image of BPO_4 product.

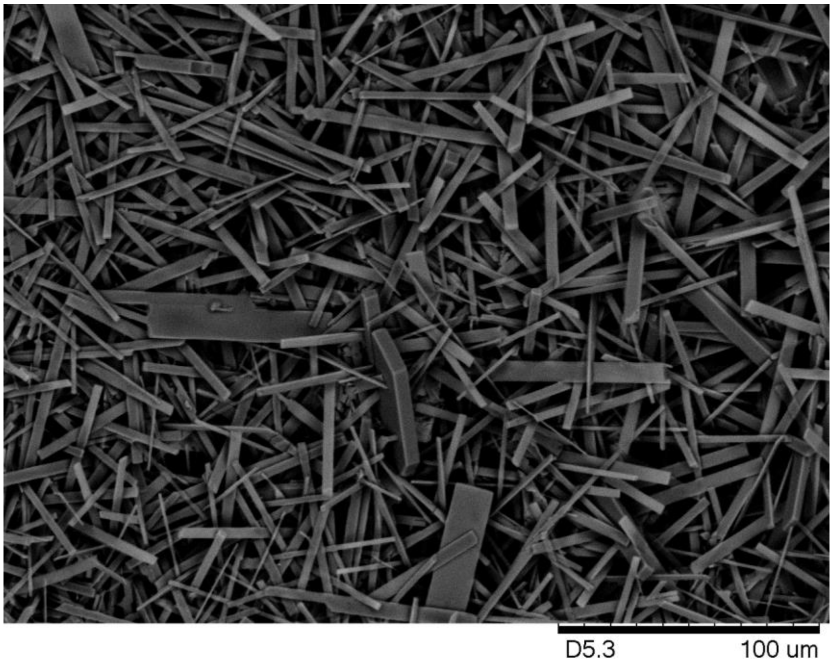

Figure B.26 – SEM image of BPO_4 product.

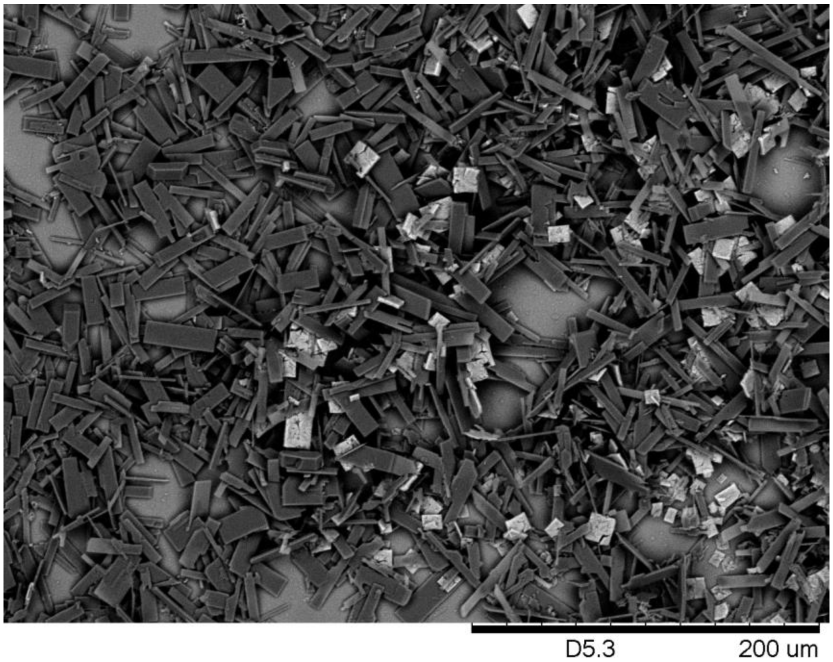

Figure B.27 – SEM image of BPO_4 product.

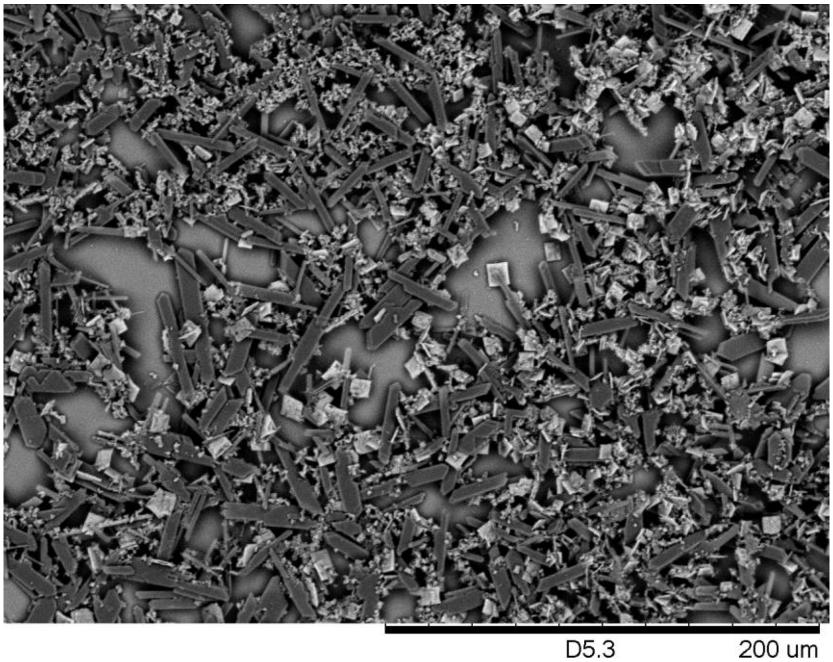

Figure B.28 – SEM image of BPO_4 product.

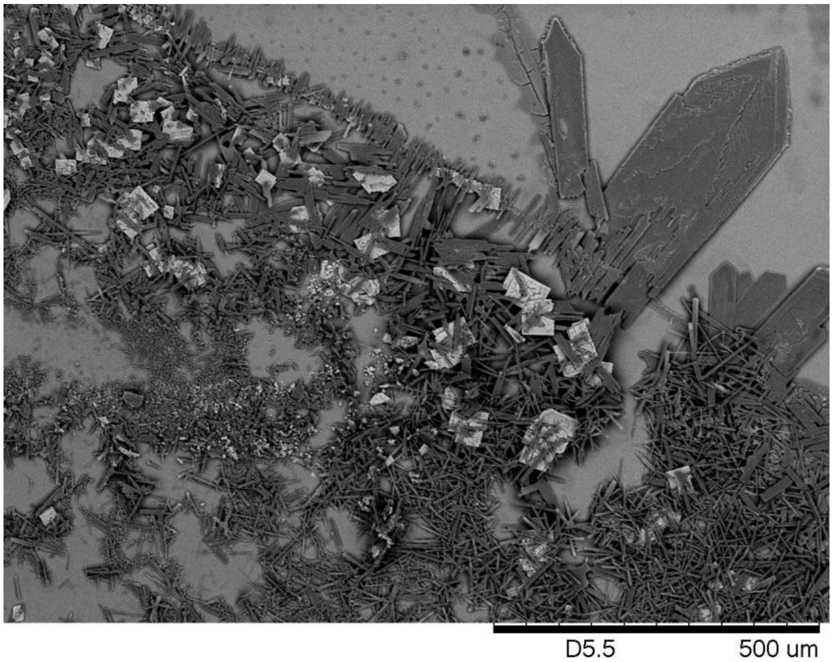

Figure B.29 – SEM image of BPO_4 product.

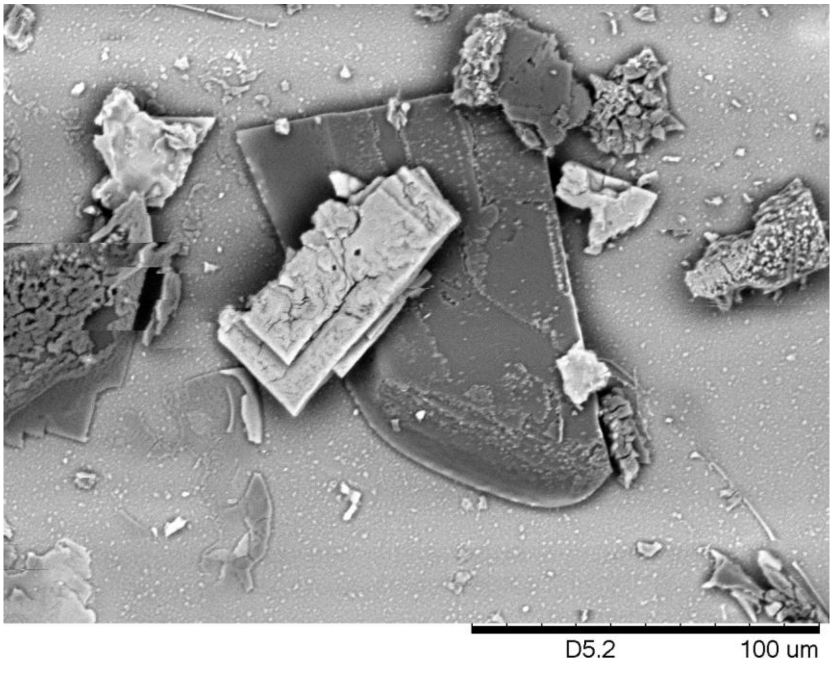

Figure B.30 – SEM image of BPO_4 product.

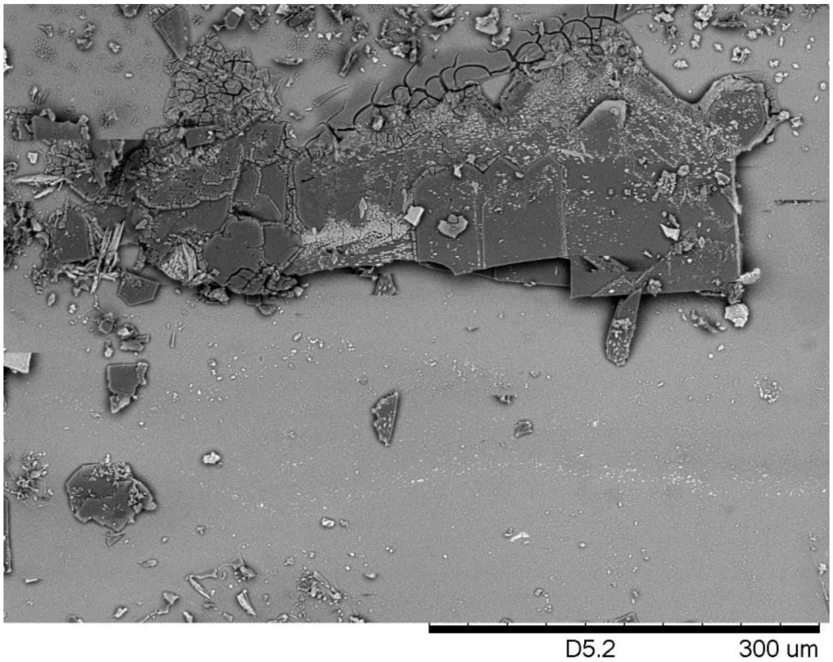

Figure B.31 – SEM image of BPO_4 product.

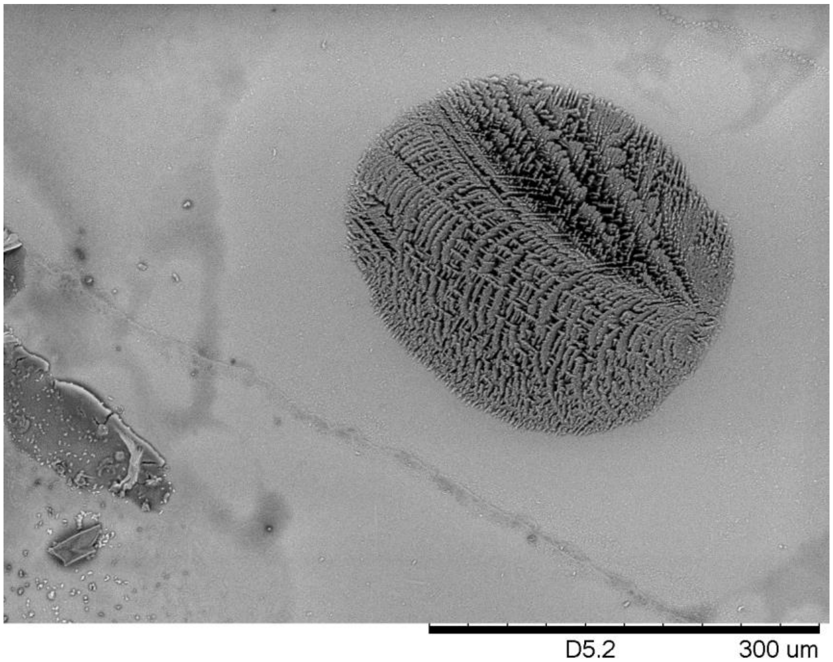

Figure B.32 – SEM image of BPO_4 product.

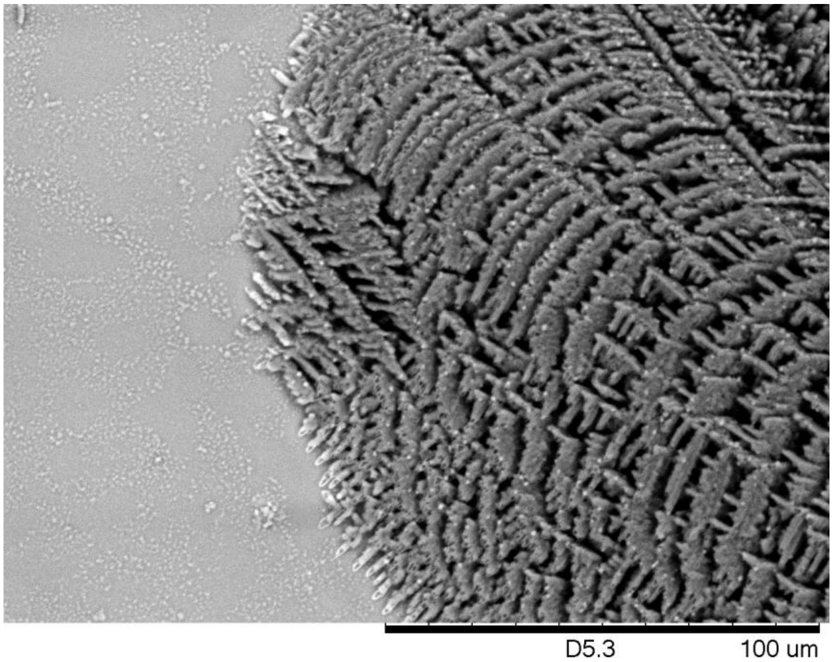

Figure B.33 – SEM image of BPO_4 product.

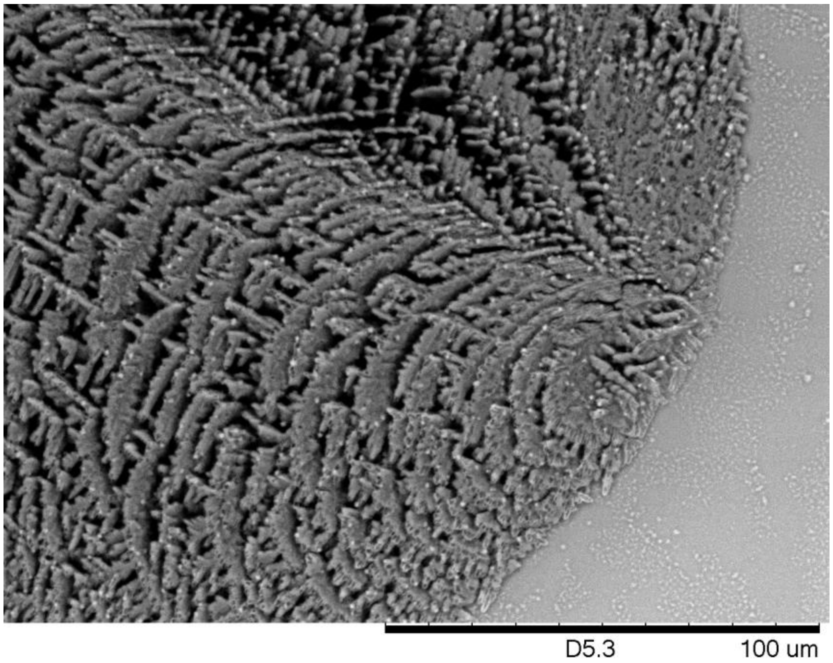

Figure B.34 – SEM image of BPO_4 product.

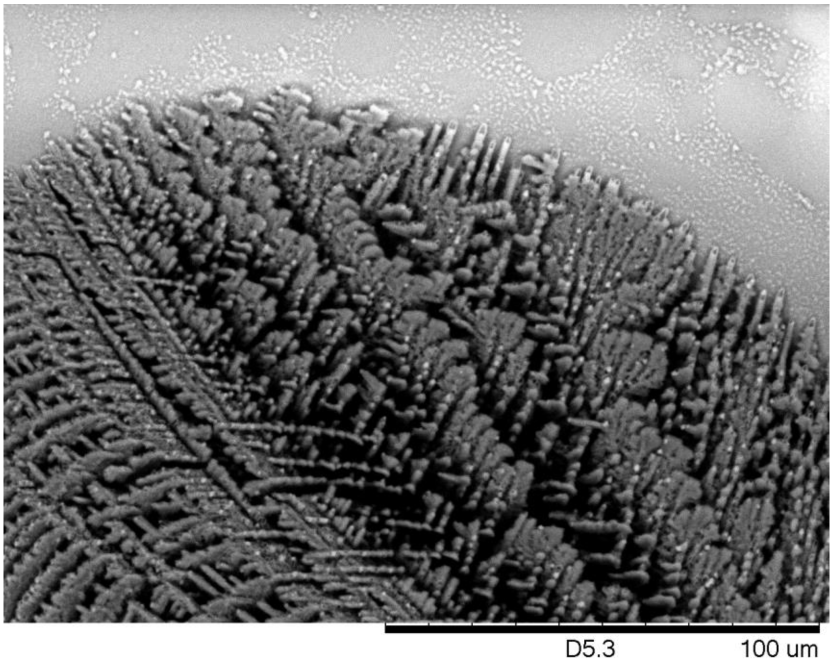

Figure B.35 – SEM image of BPO_4 product.

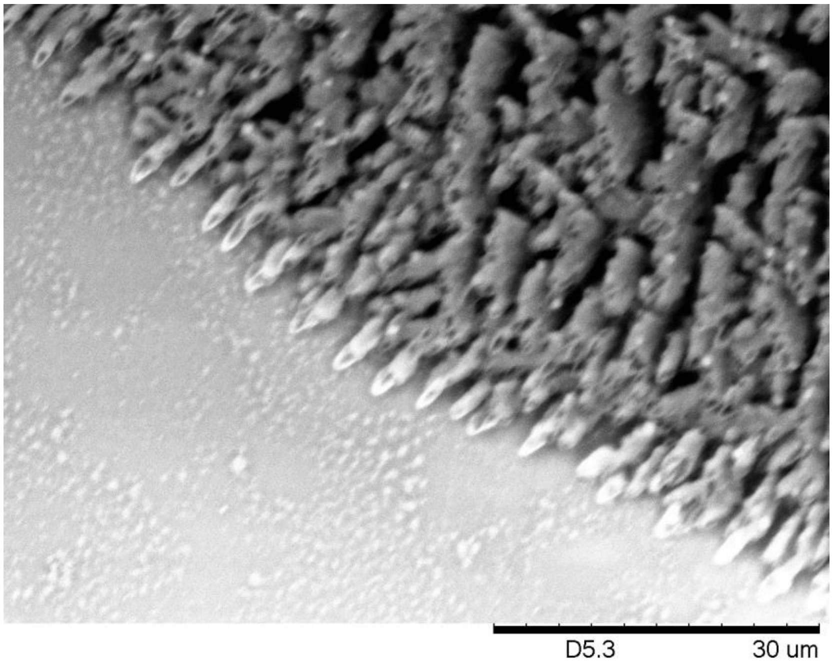

Figure B.36 – SEM image of BPO_4 product.

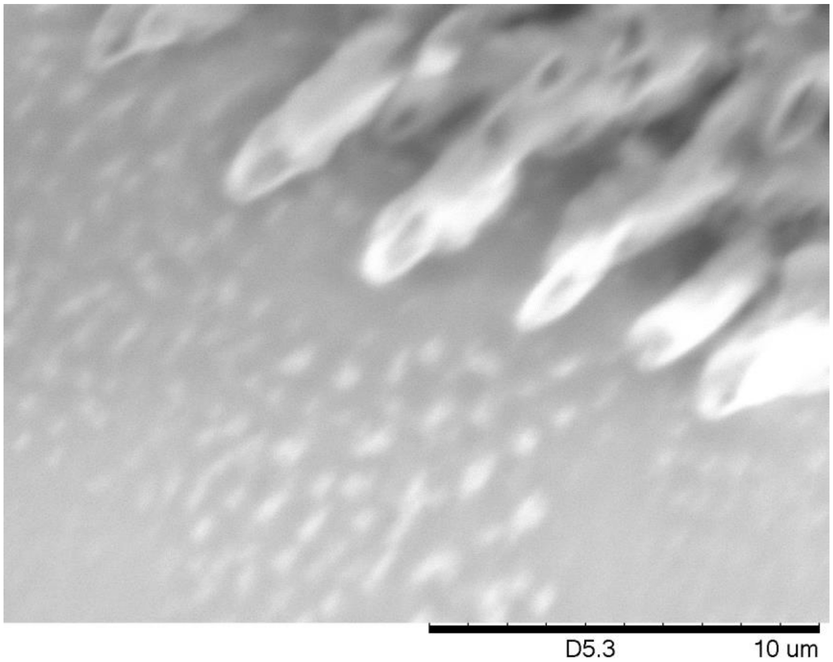

Figure B.37 – SEM image of BPO_4 product.

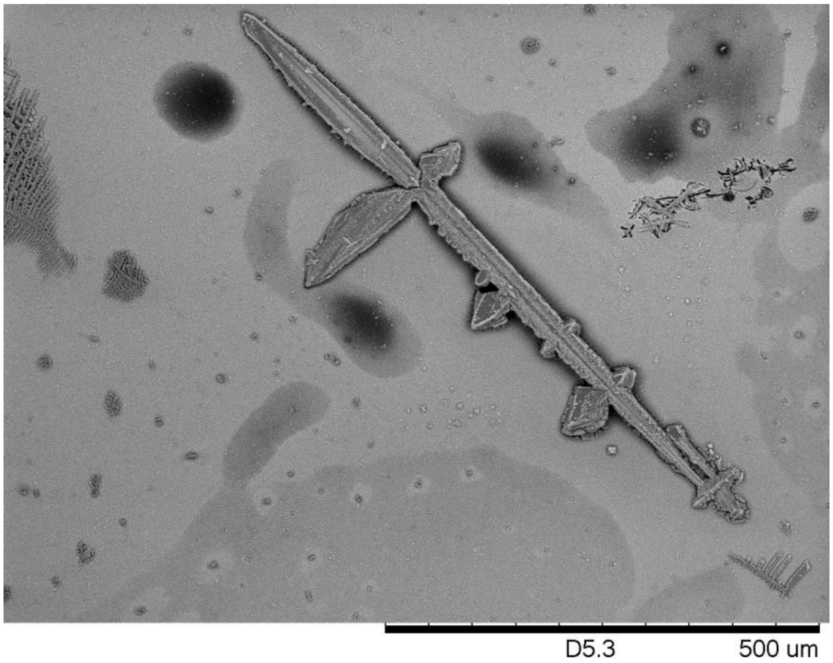

Figure B.38 – SEM image of BPO_4 product.

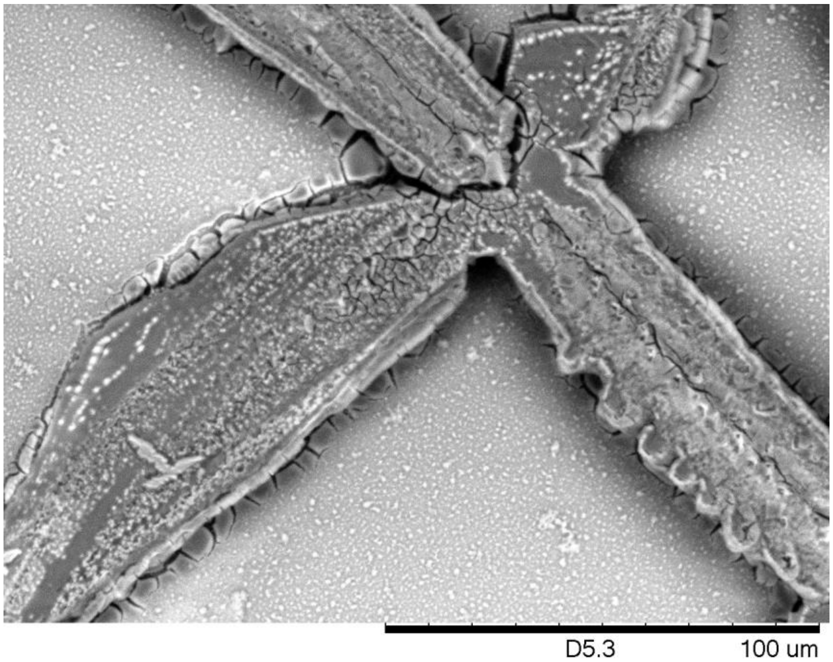

Figure B.39 – SEM image of BPO_4 product.

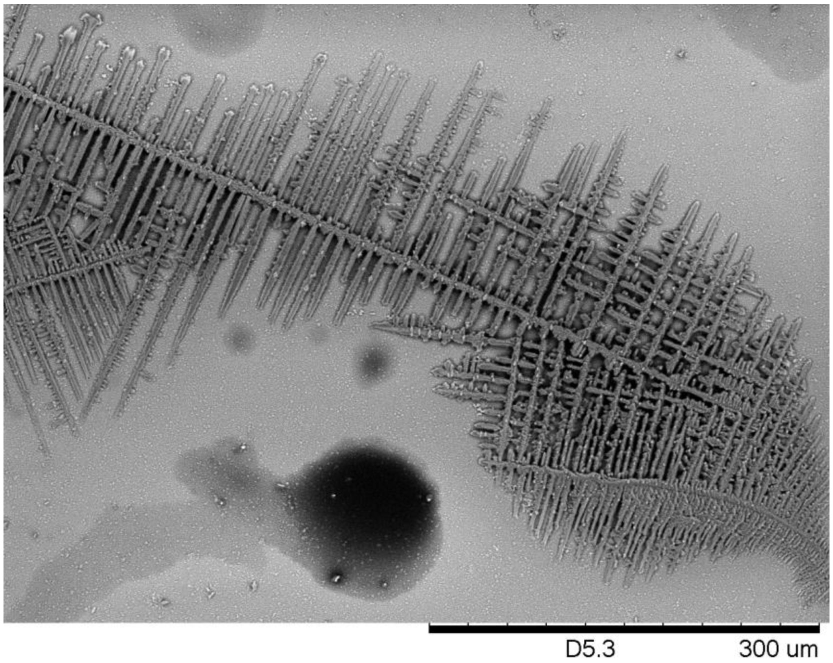

Figure B.40 – SEM image of BPO_4 product.

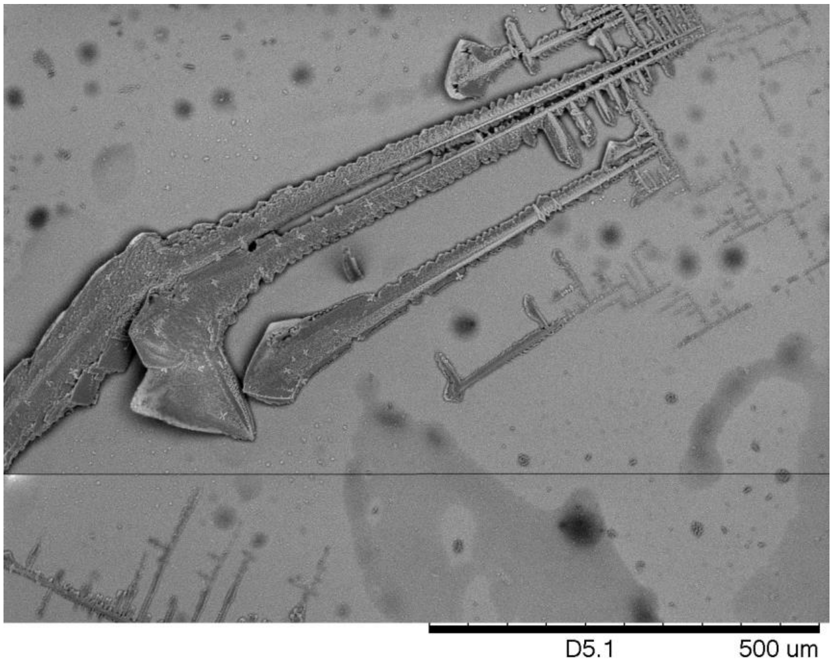

Figure B.41 – SEM image of BPO_4 product.

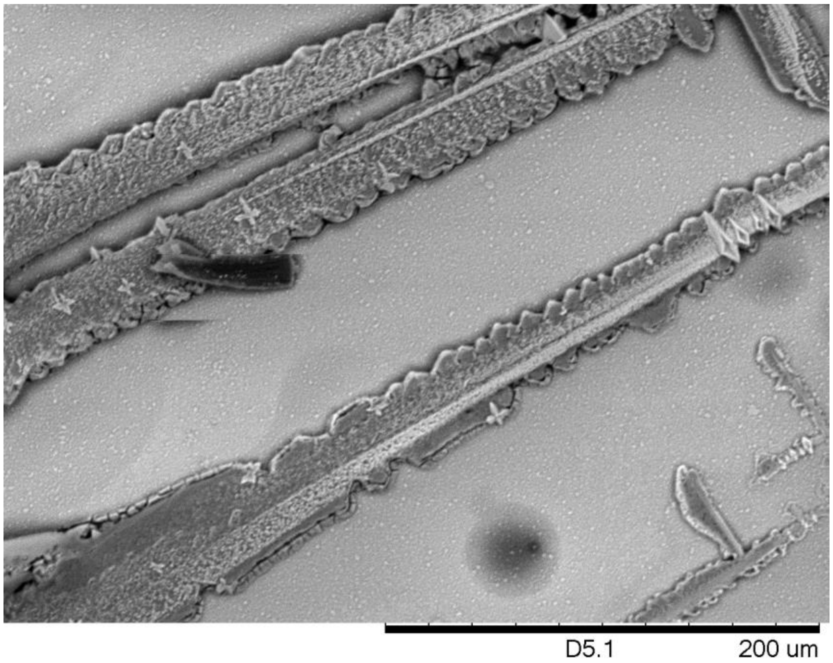

Figure B.42 – SEM image of BPO_4 product.

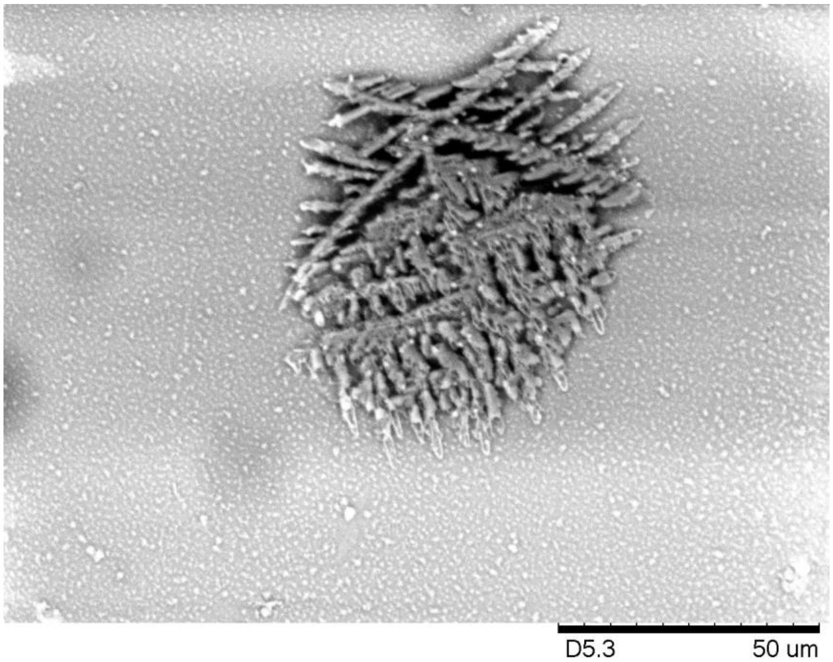

Figure B.43 – SEM image of BPO_4 product.